ABSTRACT

Inclusive Charged Hadron Transverse Momentum Spectra at Center of Mass Energy of 200 GeV for p+p and d+Au Collisions at the Relativistic Heavy Ion Collider

Jonathan Edward Gans
Yale University
December 2004

The Relativistic Heavy Ion Collider (RHIC) produces collisions that have large energy densities. One of the most pressing challenges in the field is determining if the initial energy density is sufficient to produce the Quark-Gluon Plasma (QGP). As high $p_\perp$ particles tend to be produced early in the collision, they probe the primordial era of the collision where the density is highest. These high densities are expected to cause energy loss in the particles traversing the medium which softens the fragmentation of jets and leads to the suppression of high $p_\perp$ hadrons in the final state. By measuring the extent of this suppression, we probe the density of the initial state which could help determine whether the initial state is a hadron gas or a far more dense QGP. This analysis will provide the first measured absolutely normalized p+p and d+Au charged hadron yields at $\sqrt{s_{\mathrm{NN}}} = 200$ GeV. By comparing these measurements to the inclusive charged hadron yield in Au+Au collisions at the same energy, one can measure the suppression in Au+Au and relate it to an initial density. Furthermore, the comparison helps to rule out, or support, various physical processes that lead to this suppression. This analysis will also present global observables, such as multiplicity and mean $p_\perp$, from p+p and d+Au collisions.

Inclusive Charged Hadron Transverse Momentum Spectra at Center of Mass Energy of 200 GeV for p+p and d+Au Collisions at the Relativistic Heavy Ion Collider

A Dissertation
Presented to the Faculty of the Graduate School
of
Yale University
in Candidacy for the Degree of
Doctor of Philosophy

By
Jonathan Edward Gans

Dissertation Director: John Harris

December 2004

© Copyright 2004
by
Jonathan Edward Gans
All Rights Reserved

Acknowledgements

To my soul-mate, Emily, for her unwavering support of me over many years and many miles. To my mother who first exposed me to science, tutored me in the basics, and gave up so much for my happiness. To my father for allowing my sometimes devious creativity to flourish and providing me with the means for my education. To the rest of my family and friends who each touched my life in their own way. To my advisor, John Harris, and my other mentors James Dunlop, Carl Gagliardi, Peter Jacobs, and Thomas Ullrich who always lead me in the right direction. I would like to thank the entire Yale Relativistic Heavy Ion Group group of past and present: Betty, Boris, Brian, Christina, Evan, Fei, Gerd, Haibin, Helen, Jack, Jana, Jaro, Leslie, Manuel, Matt, Mike, Nikolai, Oana, Sevil, and Zhangbu who were always eager to help. To the STAR Collaboration and the high-$p_\perp$ working group who allowed me to build upon their mountain of knowledge. Finally, to my first physics teacher Mr. Palmer and to all my teachers in all of life's subjects.

Contents

List of Figures

Chapter 1

Introduction

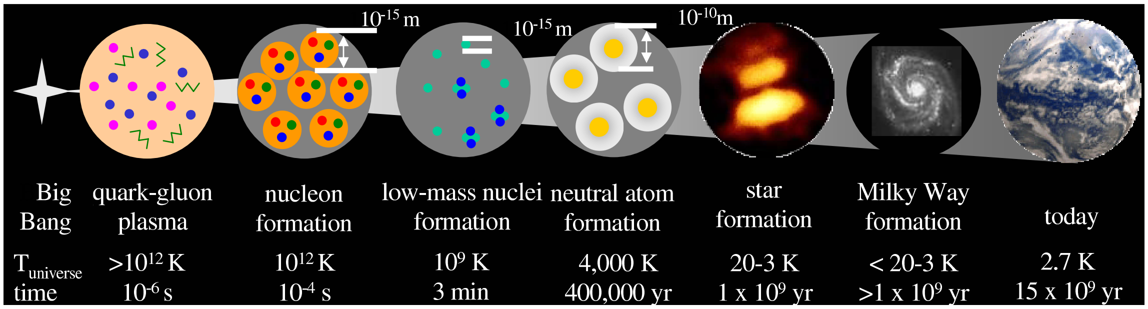

Figure 1.1: Illustration of the time evolution of the universe from the Big Bang to today. Figure adapted from [1].

Nuclear collisions serve as a time machine to study the primordial universe. One can probe earlier eras of the universe by imparting more energy, and thus a higher temperature, into the collisions as illustrated in Figure 1.1. The first and lowest energy nuclear collisions performed by Rutherford were able to resolve the charged nucleus inside the neutral atom. Higher energy collisions were able to resolve the existence of nucleons and eventually quarks bound within these nucleons [2]. The current goal of relativistic heavy ion collisions is to produce matter where the quarks effectively decouple from nucleons and behave as quasi-free particles. This is the quark-gluon plasma (QGP) which has not occurred in nature since microseconds after the "Big Bang". The evolution of the QGP may allow us to better understand the evolution of the universe itself.

Before studying the QGP, one must first confirm its very existence. Numerical lattice calculations show that nuclear matter experiences a phase change into a QGP at high density and temperature [3]. This behavior is shown in Figure 1.2(a) for 3 different quark configurations. The sign change of the second derivative at $T/T_c =$

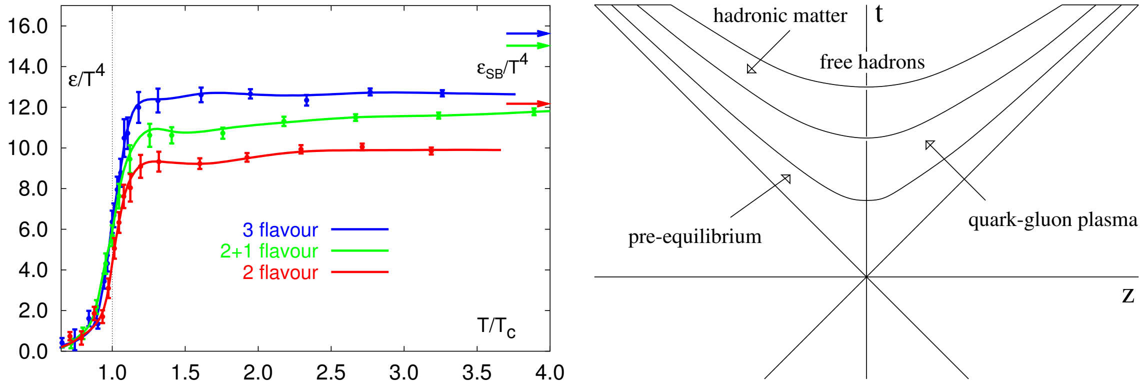

(a) **(b)**

Figure 1.2: (a) Lattice calculations of the dependence of the density versus temperature. The sharp knee indicates the crossover from bound to free quarks and gluons. The different curves are for 2 or 3 light quarks, or 2 lights quarks plus 1 heavy quark. Figure taken from [3]. (b) The expected evolution of a nuclear collision. The quark-gluon plasma stage lasts approximately 10 fm/c.

1 indicates a phase transition. Depending on the assumptions used in these calculations, the critical temperature $T_c \approx$ 150-170 MeV, which is more than 100,000 times the temperature of the sun's core. The critical density $\epsilon_c \approx 1$ GeV/fm^3, which is 6 times denser than normal nuclear matter or 10 million times denser than water. Unfortunately, it is difficult to measure the temperature, and thus prove thermodynamic equilibrium, of matter that exists for approximately 10 fm/c (3.3×10^{-23} seconds). However, as will be discussed in the following sections, by using well calibrated probes of high transverse momentum (high-$p_\perp$) particles in elementary p+p and complex d+Au and Au+Au collisions, one can extract the initial energy density of heavy ion collisions.

1.1 Quantum Chromodynamics

The original parton model claimed that baryons, such as protons, neutrons, and Δ baryons, consist of 3 fractionally charged quarks while mesons, such as π's, and ρ's, consist of a quark anti-quark pair. This naive model required modification with the observation of the doubly charged Δ^{++}, as its decay properties suggest that it is made up of three identical spin 1/2 quarks, thus violating the Pauli exclusion principal. A new quantum number called color was introduced to fully anti-symmetrize the Δ^{++} wavefunction. This three component color charge is treated similarly to the electric charge in Quantum Electrodynamics (QED) except the propagators of the field are color charged gluons while the photon of QED has no electric charge. Quantum Chromodynamics (QCD) is the theory of colored interactions. It attempts to incorporate all the experimental properties of quarks and gluons even though these particles never have been observed as free particles.

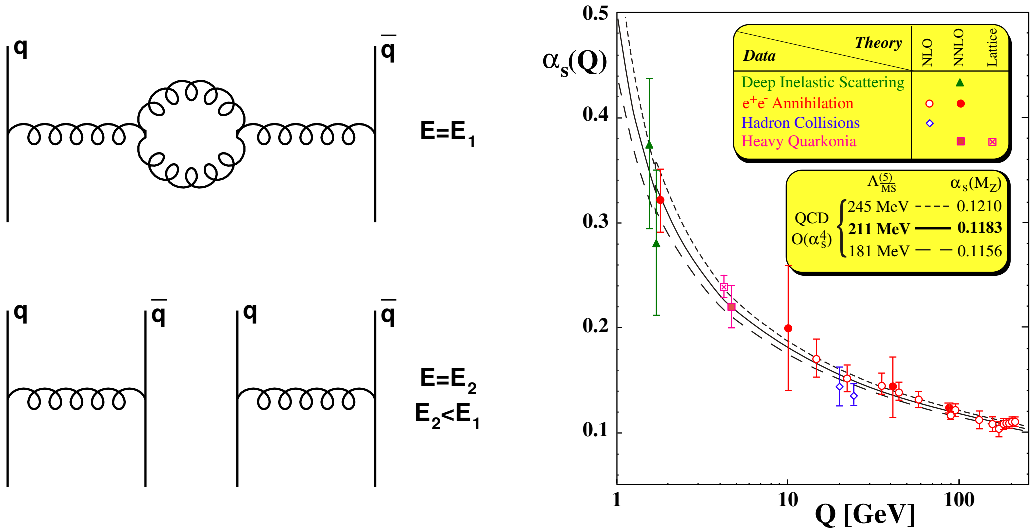

(a) (b)

Figure 1.3: (a) Feynman diagram of the quark-quark coupling. At large distances it is energetically advantageous to convert a gluon-gluon loop, with energy E_1 into a quark anti-quark pair with energy $E_2 < E_1$. (b) The QCD running coupling constant $\alpha_S(Q)$ determined from a variety of processes. Figure taken from [4].

The existence of the color field is able to explain some of the experimental subtleties of QCD. As already mentioned, free quarks and gluons have not been observed in nature, which suggests an increasing attractive force with the distance between two quarks. Since a gluon has a color charge, it can couple to other gluons as shown by the loop in the top of Figure 1.3(a). At larger distances, more energy will be stored in the gluon-gluon vertices, which increases the coupling between the two original quarks and leads to a color charge anti-screening. At some distance, however, the coupling must stop because there is no attraction between quarks in different nuclei. This suggests that a colorless gluon cannot exist as it would mediate a long range force. The combination of these two properties makes it impossible to isolate a single quark. If somehow two quarks could be pulled apart, the energy stored in the gluon-gluon vertices, E_1, would convert into a quark anti-quark pair resulting in two separate mesons with energy $E_2 < E_1$ as shown in the bottom of Figure 1.3(a). The state of two separated mesons is energetically favored to a single meson with large interquark separation. This property of QCD is known as confinement.

In contrast to confinement, the results from large-momentum transfer experiments can be described by a model where the quarks have no interaction. From the uncertainty principal, one determines that large momentum transfer probes small distances. One then can deduce that the coupling decreases at small distances. This property of QCD is known as asymptotic freedom.

The dependence on the QCD coupling, α_s, on momentum transfer, Q, is shown in Figure 1.3(b) from various experiments. At sufficiently high energies, $\alpha_s \to 0$ the quarks and gluons behave as free particles. At low energies, $\alpha_s \to \infty$ binding the quarks and gluons within the nucleon. A lowest order QCD calculation parameterizes the above data as

$$\alpha_s(Q^2) = \frac{1}{\beta_0 \ln(Q^2/\Lambda^2)} \tag{1.1}$$

where β_0 is a constant that depends on the number of active quark flavors and Λ is the energy scale where $\alpha_s(Q^2)$ diverges to infinity [5]. The Λ parameter in the lowest order calculation is approximately 0.1 GeV and effectively sets the lower bound for the predictive power of QCD. Figure 1.3(b) shows fits to the data from higher order calculations which illustrate the model dependent variance of Λ.

1.2 Predictions of QCD

In order to discover the QGP, one requires a sensitive and well calibrated probe. This analysis uses high transverse momentum particles as their production is well modelled by QCD. The predictive power of QCD owes itself to two properties, evolution and factorization. Evolution states that as long as the QCD coupling is small,

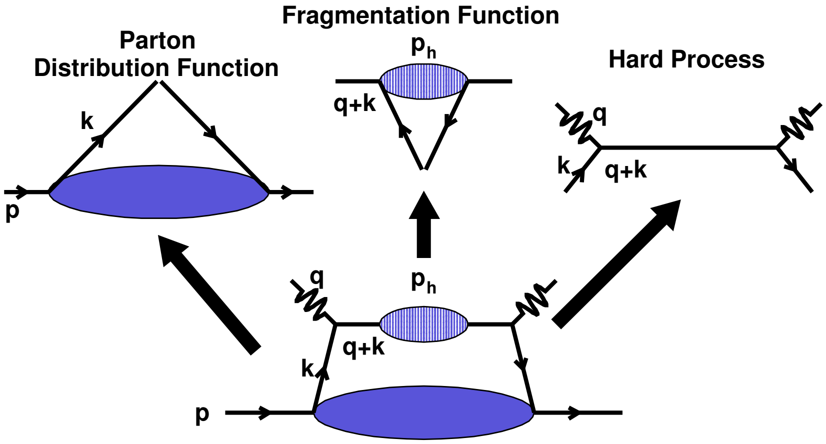

Figure 1.4: Illustration of a deep inelastic parton-hadron scattering which can be factorized into three separate contributions.

measurements of certain quantities at one energy can be used to determine the same quantity at other energies. Factorization states that particle production from parton-hadron collisions at high Q^2 can be separated into three independent contributions: parton distributions, hard processes, and fragmentation. The Feynman diagrams for a parton-hadron scattering are shown in Figure 1.4 along with the breakdown into the factorized contributions.

The inclusive invariant cross section for a $p+p \rightarrow$ hadron + X is given in the first order by

$$\frac{d\sigma}{dy} = \sum_{a,b} \int_0^1 dx_A \; dx_B \; dz_c \; f_{a/A}(x_A, Q_a) \; f_{b/B}(x_B, Q_b) \; \frac{D_{C/c}(z_c, Q_c)}{z_c} \frac{d\hat{\sigma}_{ab\rightarrow cd}}{dy}. \qquad (1.2)$$

The probability to find a parton of type i in the proton I with momentum fraction x_i of the proton is $f_{i/I}(x_i, Q_i)dx_I$. Examples of parton distribution functions are shown in Figure 1.5(a) where $\int x f_{i/I}(x)dx$ is the total number of partons of type i in the hadron. These functions are extracted by global fits to experimental data [6]. The cross section for these partons to produce the outgoing partons is given by $d\hat{\sigma}_{ab\rightarrow cd}/dy$, which are calculated using the Feynman rules of QCD and the experimental determination of the QCD constant α_s. Finally, $D_{C/c}(z_c, Q_c)dz_c$ is the mean number of hadrons produced of type c with momentum fraction between z_c and $z_c + dz_c$ of the parent parton C. This fragmentation function essentially is the final state analogue to the initial state parton distribution function. Figure 1.5(b) shows examples of fragmentation functions. An in-depth review of fragmentation functions and their extraction from experimental data can be found in Reference [7].

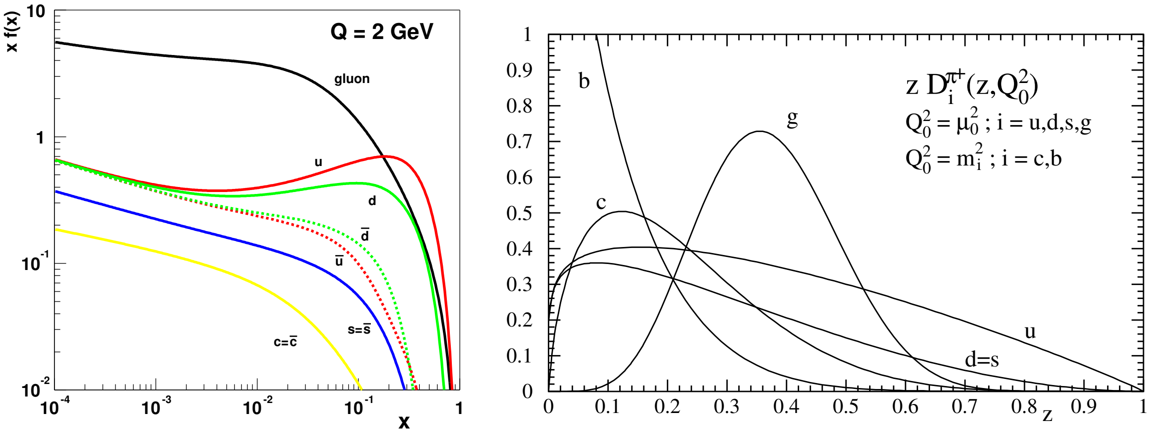

(a) **(b)**

Figure 1.5: (a) A parametrization of parton distribution functions at $Q = 2$ GeV. Calculations from [6]. (b) A parametrization of π^+ fragmentation functions at $Q_0^2 = 0.4$ GeV^2. Figure taken from [7].

The above framework applies to proton-proton collisions in a vacuum. To compare to nucleus-nucleus collisions, one must scale the particle production in some way. A popular model of this scaling is to assume that nucleus-nucleus collisions are a superposition of many proton+proton collisions as discussed in Appendix E. By comparing hadron production to the framework of Equation 1.2, one can determine if the presence of a nucleus leads to a modification of the theory. As will be shown, the data suggest such a modification. Some models focus on initial-state effects and advocate that the presence of the nucleus alters the parton distribution functions. Other models focus on final-state effects and argue that the fragmentation functions are modified by the hot and dense medium created from the collision. If the latter is the case, one can use the inclusive hadron spectra to determine if the density of this medium is sufficient for the creation of the Quark Gluon Plasma.

1.3 Outline

Chapter 2 of the thesis will discuss the experimental facilities used to conduct this research. Chapter 3 will document the data analysis and corrections of the raw data, while Chapter 4 will present the absolutely normalized proton+proton $\rightarrow h^{\pm}$ + X cross section and other event-wise variables. Chapter 5 will compare this data to dueteron+gold (d+Au) collisions, gold+gold (Au+Au) collisions, and various theoretical frameworks that incorporate elements of QCD. Appendix F describes the d+Au analysis and the other appendices expand upon technical and theoretical concepts mentioned in the text.

Chapter 2

Detector Setup

2.1 The Relativistic Heavy Ion Collider Complex

The experiments were conducted at the Relativistic Heavy Ion Collider (RHIC) located on Long Island, New York. RHIC is one element of the heavy ion physics program housed at Brookhaven National Laboratory (BNL). A schematic diagram of the RHIC accelerator complex is displayed in Figure 2.1. RHIC is the first and

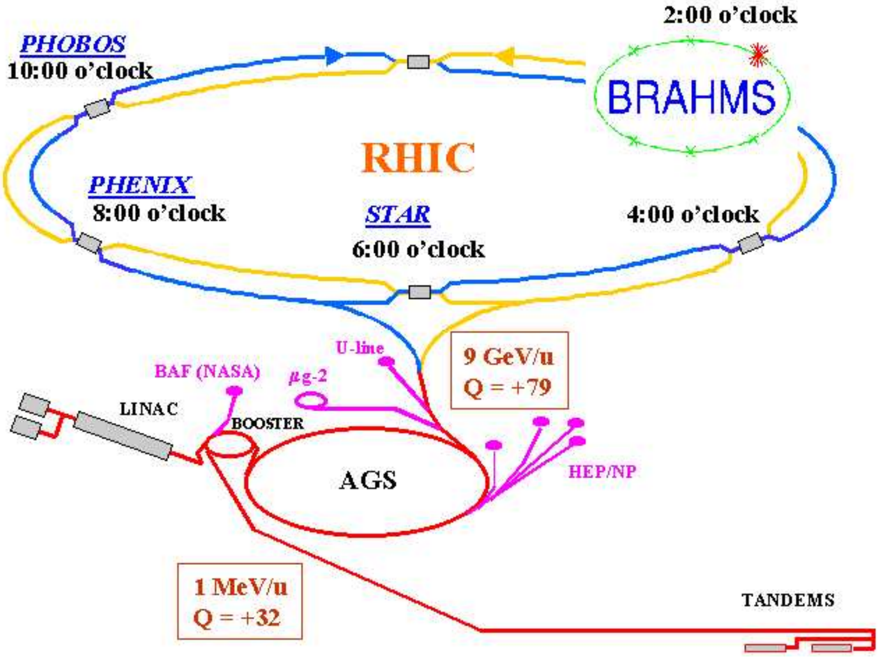

Figure 2.1: The Relativistic Heavy Ion Collider (RHIC) accelerator complex at Brookhaven National Laboratory.

Collision Type	Lab Energy A	Lab Energy B
Colliding Beams	100 GeV	100 GeV
Fixed Target	0 GeV	21469 GeV

Table 2.1: Energy of nuclei needed to produce center of mass energy per nucleon $\sqrt{s_{\mathrm{NN}}} = 200$ GeV.

currently the only operating nucleus-nucleus collider accelerator. All other nucleus-nucleus collisions to date were performed with an accelerated beam on a fixed target. A colliding beam has many advantages. By having two beams colliding at the center of mass, more energy is provided to the collision rather than the translation of the entire system. An example of the energy advantages are given in Table 2.1. Due to RHIC's two quasi-independent rings, it can collide protons on protons (p+p). All previous colliding beam experiments at the same or greater energy [8] can only collide protons on anti-protons (p+$\bar{\mathrm{p}}$). RHIC can also handle asymmetric collisions, such as protons on gold.

2.1.1 The Pre-Accelerators

Accelerating ions in RHIC is a multi-stage process, each adding more energy to the ions [9, 10]. The gold ions are initially accelerated in the Tandem Van de Graaff Facility labelled as Tandems in Figure 2.1. It consists of two 15 MeV Pelletron® [11] electrostatic accelerators in series shown in Figure 2.2. The two Tandem Van de Graaff electrostatic accelerators (a primary and a backup) accelerate gold ions from a cesium sputter ion source [12]. Starting out with an electric charge of -1 (Au^{-1}), the ions are accelerated from ground through a 14 mega-Volt (MV) potential. The ions pass through a carbon foil which removes 13 electrons (Au^{+12}) and the ions are accelerated back to ground. The ions leave the tandem with ~1.0 MeV/u (million electron volts per nucleon). After the initial acceleration, another 20 electrons are removed (Au^{+32}) and the ions travel along a ~850 meter-long tunnel called the Tandem to Booster (TtB), which injects the ions into the Booster synchrotron. The Booster removes all but two of the electrons (Au^{+77}), accelerates the ions to 95 MeV/u, and injects them into the main AGS ring.

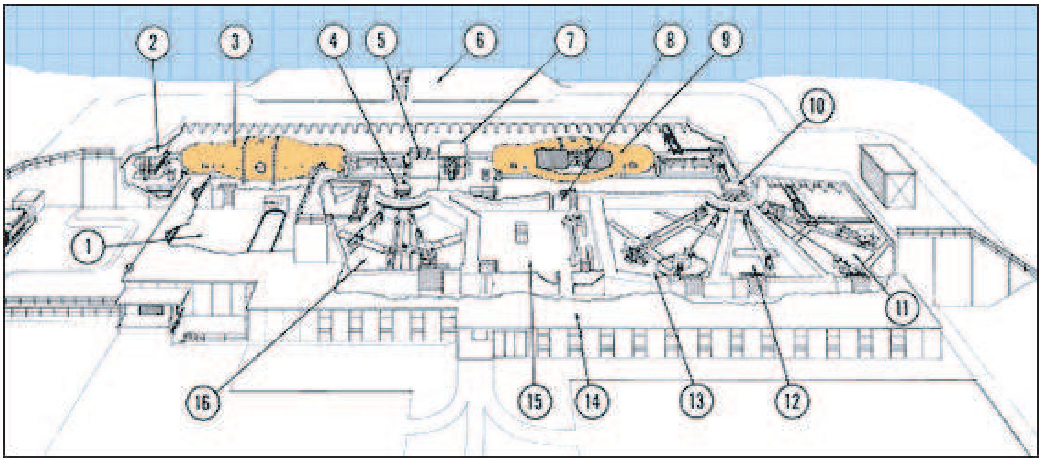

Figure 2.2: The Tandem Van de Graaff Facility.

The Alternating Gradient Synchrotron(AGS) once served as Brookhaven National Laboratory's premier accelerator where the research for three Nobel Prizes was conducted in the mid-20th Century. The AGS implemented a breakthrough in accelerator technology called alternating gradient focusing, in which the field gradients of the accelerator's 240 magnets are successively alternated inward and outward, permitting particles to be propelled and focused in both the horizontal and vertical plane at the same time. The AGS is capable of accelerating 25 trillion protons with every pulse, and heavy ions such as gold and iron [13]. The AGS accepts the beam from the Booster, accelerates it to an energy 8.86 GeV/u and then removes the remaining 2 electrons (Au^{+79}). The ions are finally injected into the RHIC rings. Because of this multi-stage acceleration, after the AGS fills the RHIC rings it decouples from RHIC and can run other ions and conduct its own fixed target experiments until RHIC needs to be filled again (almost every four hours presently).

The path taken for the deuteron ions is similar to the path taken by the gold ions. The deuteron's are produced at the source from titanium deuteride (TiD_2) with a single negative charge (D^{-1}) and are accelerated through the Tandem Van de Graaff to an energy of 12 MeV/u and a positive electric charge (D^{+1}). Next, the deuterons are injected into the Booster and brought to 153 MeV/u and injected into the main AGS ring which brings them to an energy of 12 GeV/u. The deuterons are then brought to the top energy of 100 GeV/u in one of the main RHIC rings [14].

When accelerating protons, a separate injection system is used labelled LINAC in Figure 2.1. The protons start out as hydrogen gas in the BNL Linear Accelerator (LinAc). The protons are accelerated by nine radio frequency cavities with a total length of 140 meters. A picture of these cavities is shown in Figure 2.3. The LinAc accelerates the protons to 200 MeV. After the LinAc, the protons follow a similar path as that of the heavy ions. They are injected into the AGS booster which brings them to 1.5 GeV and then the AGS accelerates them to 25 GeV. From here they are injected into the two RHIC rings.

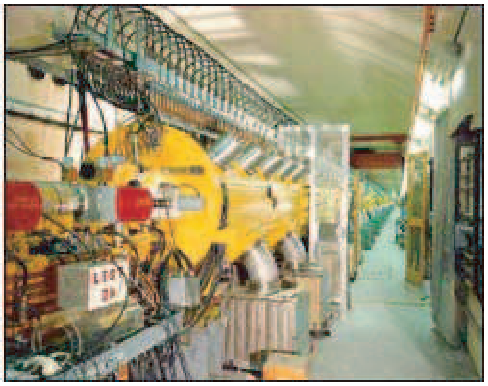

Figure 2.3: The Linear Accelerator Tunnel.

2.1.2 The Relativistic Heavy Ion Collider

The two RHIC rings are each 3.8 km in circumference. They consist of 396 9.7 m long super-conducting dipole magnet elements that provide a magnetic field of up to 3.458 Tesla. There are additional smaller magnets bringing the total number of superconducting magnets to 1740. The magnets must be run at 4.6 Kelvin, so they are cooled actively by liquid nitrogen and liquid helium. The RHIC cooling system is closed and the nitrogen and helium must be recycled and refrigerated. This is the main cost associated with operating RHIC because it consumes 21 mega-Watts (MW) of electricity. A cross section of the tubes is shown in Figure 2.4(a) and a picture of the assembled rings is shown in Figure 2.4(b). The RHIC rings accelerate

Collision Nuclei	Num. Buckets	Mean Num. ions per bucket	Maximum Event Rate
proton+proton	60	100×10^9	1 per 213 ns
deuteron+gold	60	80×10^9 (d) and 1×10^9 (Au)	1 per 213 ns
deuteron+gold	120	80×10^9 (d) and 1×10^9 (Au)	1 per 107 ns

Table 2.2: RHIC Beams Fill Parameters

the protons, deuterons or gold to their final energy of 100 GeV/u. [9]

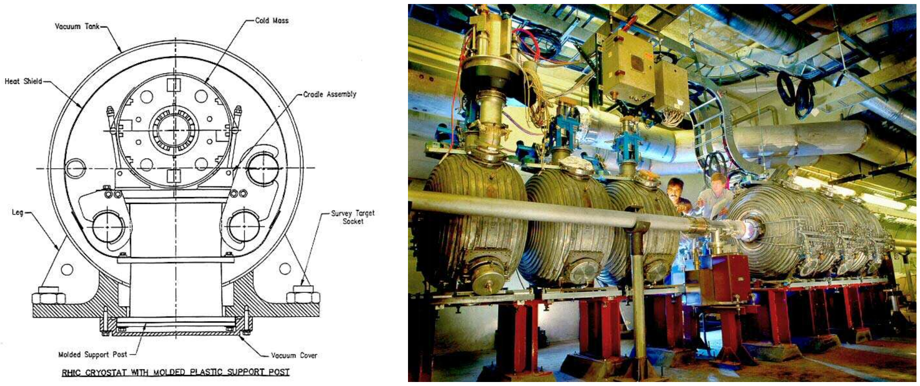

(a) **(b)**

Figure 2.4: RHIC acceleration cavities: (a) a cross-sectional diagram and (b) a picture of the RF cavities.

The RHIC beams do not have a continuous intensity. The ions are stored in many distinct buckets, with a vacuum of approximately 10^{-11} Torr [15] in between each bucket. The nominal number of ions per bunch are 1×10^9, 80×10^9, and 100×10^9 for gold, deuterons, and protons respectively [16, 17]. The number of filled buckets can be varied. For example, the fewer buckets that are filled, the easier it is to accelerate and keep the beam stable as there are less intra-beam effects. RHIC can handle a maximum of 360 buckets in each ring, although it usually runs a factor 3 or 6 fewer buckets. Table 2.2 summarizes the bucket configuration used by RHIC for this analysis.

There are many reasons RHIC gathers the beam into bunches. The RF Cavities used to accelerate the beam are more efficient at accelerating discrete buckets of ions. Also, since the location of the buckets can be tracked, the experiments can be told when a bucket is entering their detectors, which makes the trigger more efficient (more on triggering in Sections 2.2.1 and 3.6.2). By leaving a few empty buckets in a row (abortgaps), the beam can be controlled more easily. For example, this allows the accelerator magnets to switch modes over a longer period of time when filling or dumping the beam. Examples of beam fill patterns, the number of events per bunch crossing number, are shown in Figure 2.5. The bunch crossing numbers range from 0 to 120 for the p+p and d+Au runs. Notice in the p+p run (Figure 2.5(a)), every other bunch crossing is empty because only 60 bunches are used in each ring. The abortgaps can be seen at bunches 36-46 and 76-86. In the later half of the d+Au run (Figure 2.5(b)), RHIC switched to 120 buckets and one can see that every bunch is filled except for the abortgaps located at 28-37 and 68-77. The location of the abortgaps change every run and have to be found dynamically.

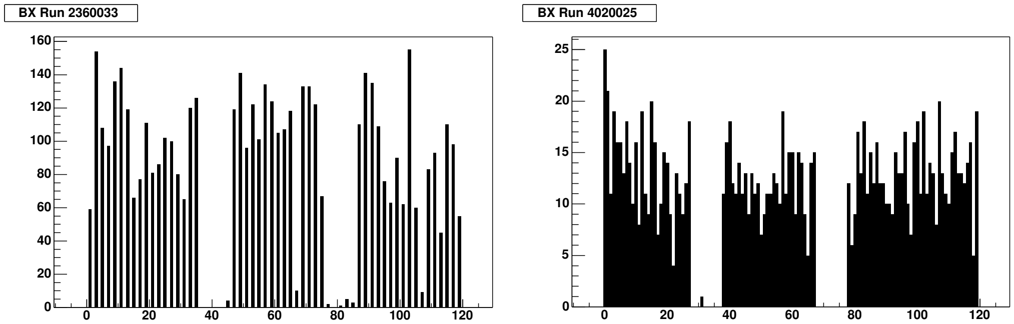

(a) **(b)**

Figure 2.5: RHIC Fill Pattern for (a) p+p and (b) d+Au collisions.

The RHIC beams are not truly independent because they must travel through a common beam pipe in order to collide in the experimental halls. The beams are diverted out of the two main rings by the DX or kicker magnets which provide a 4.3 Tesla field. The kicker magnets are located on either side of each collision area as shown in Figure 2.6 [18]. One set diverts one beam into the common Beryllium beam pipe and the other diverts the beam back into the main RHIC ring. However, since the DX Magnets are shared by the counter-rotating beams, the magnets need to perform both operations at the same time. Because of this, RHIC ran deuteron (the bound state of a proton and a neutron) on gold collisions instead of proton on gold collisions. The charge to mass ratio $\frac{q}{m}$ is closer for deuterons and gold than for protons and gold. As magnetic deflection depends on this ratio, the deuteron(d)+Au configuration is easier to achieve technically. In the interest of time, the decision was made to run d+Au first because this physics is very similar to proton(p)+Au. RHIC will eventually run p+Au by moving the location of one of the DX Magnets in each of the collision areas.

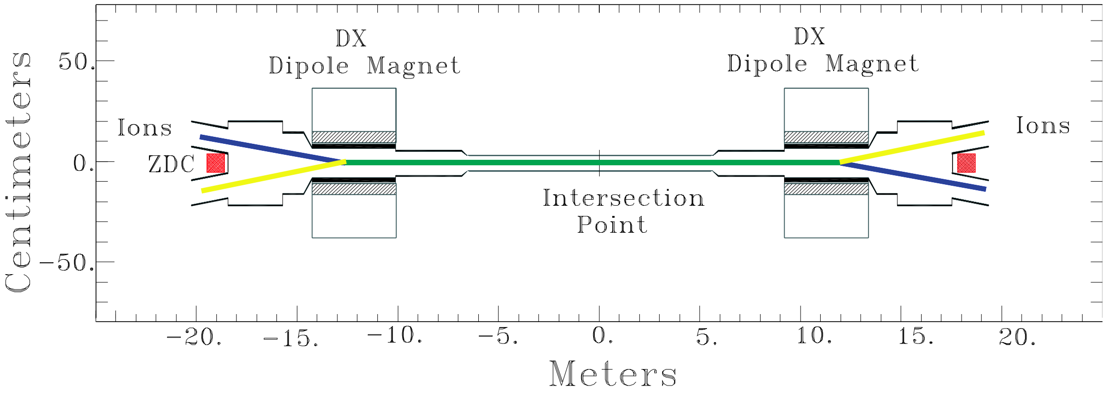

Figure 2.6: DX Magnet Location. The DX Magnets divert the two separate RHIC beams (Blue and Yellow) into the common beam pipe (Green). Notice the beams cross.

2.2 The STAR Experiment

All data presented were recorded at the Solenoidal Tracker at RHIC (STAR) experiment which is one of the four experiments at RHIC as shown in Figure 2.1. The main detector that gives STAR its name is a multi-purpose, large acceptance drift chamber designed to measure many observables. A schematic design overview of STAR is shown in Figure 2.7. Despite its name, there are many other detector components in STAR.

2.2.1 Trigger Detectors

Before a detector acquires data, it must be triggered. STAR has a robust capability to trigger with many different methods, but only the methods and detectors used in

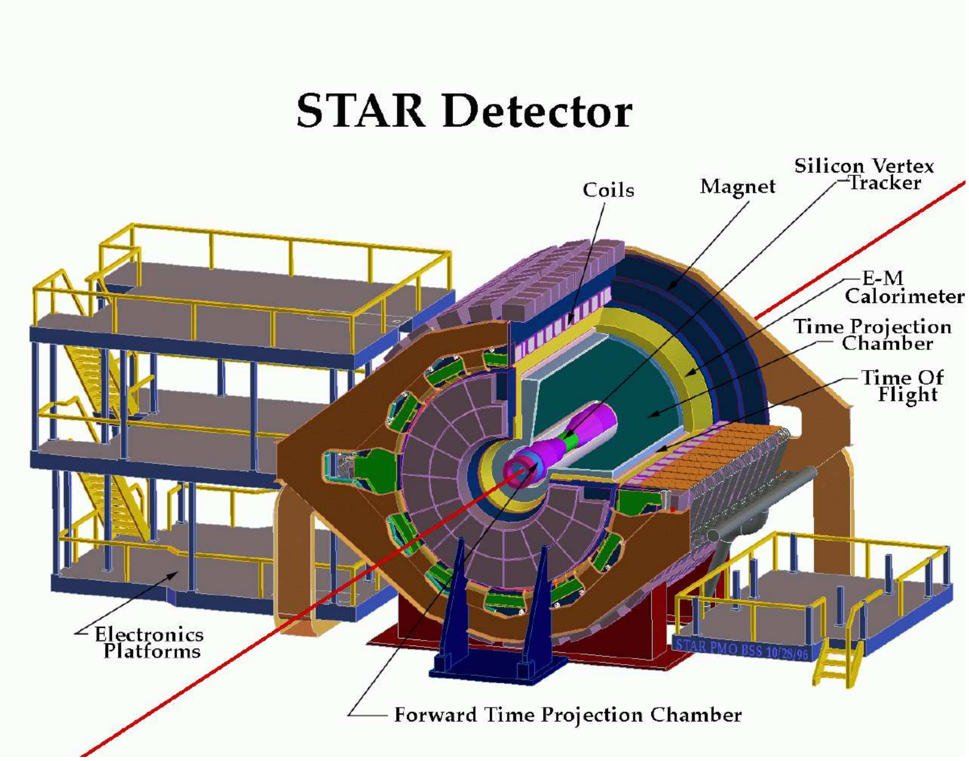

Figure 2.7: Illustration of the STAR detector.

this analysis will be discussed.

Beam-Beam Counters

The first p+p collisions, in 2001, presented novel challenges to STAR which had previously recorded only heavy ion collisions. In terms of triggering, the main difference between p+p running and Au+Au running is the multiplicity, or the number of tracks per event. In Au+Au collisions, one has roughly 5000 tracks per event, and a minimally biased trigger can be implemented based on the many mid-rapidity tracks and spectator neutrons [19]. Therefore, STAR previously only had trigger detectors that relied on large amounts of mid-rapidity tracks, or high rapidity neutral spectators, both of which p+p collisions lack. To solve this acceptance gap, the STAR Beam-Beam Counters (BBCs) were implemented shortly before the start of the p+p data run.

The BBCs are annular scintillator detectors which are sensitive to charged tracks. They are situated ±3.5 m from the interaction region. Figure 2.8 shows a schematic diagram of the BBCs and a picture of one BBC frame mounted in STAR. For the p+p data set, only the small inner tiles shown in blue in Figure 2.8(b) were active covering pseudorapidity $3.3 < |\eta| < 5.0$. These inner tiles can all be inscribed within a circle of 9.64 cm. The RHIC beam line passes through the center of the BBC (labelled B in Figure 2.8(a)) with a 1 cm annular clearance.

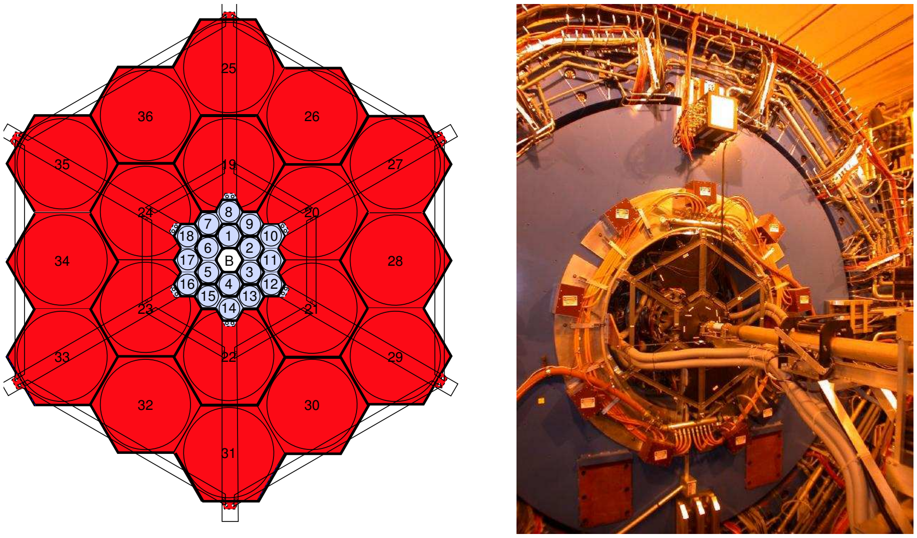

(a) **(b)**

Figure 2.8: (a) Diagram of the Beam-Beam Counter (BBC) layout. (b) Picture of the BBC frame mounted on the STAR endcap with the RHIC beamline protruding. The detector is approximately 0.5 meters in diameter.

Eight photomultiplier tubes (PMTs) were used for the 18 small hexagonal scintillator tiles comprising one annulus on both the east and west sides of the STAR magnet. Each tile has four wavelength shifting (WLS) optical fibers inserted into circular grooves inscribed within the hexagonal scintillator to collect scintillation light. The tiles are grouped to allow for radial and azimuthal segmentation of the readout. The grouping is: 1, 2-3, 4, 5-6, 7-9, 10-12, 13-15, 16-18. Each group has an optical connector to mate the WLS fibers to clear optical fibers for light transport to the PMT's. The voltage on the PMT is run through an Analog to Digital Converter (ADC), which maps the amount of light collected to a number in a monotonically increasing fashion. The fine segmentation of the BBC's was not used in the p+p minimum bias trigger. Rather the trigger sums the output of all the tiles on a BBC. If both BBC's have a value above a predetermined noise threshold, within a time window $\Delta t = 17$ ns, the event is written to disk. There are no higher-level triggers used in this data set. Because both BBC's are required to fire, this is a dual arm trigger that is primarily sensitive to non-singly diffractive (NSD) events. The efficiency of this trigger will be discussed in Section 3.6.2.

In an ideal detector, one could also use the BBC's as tracking or vertex detectors. By comparing the arrival time between the two detectors located on opposite sides of the collision, one could determine the longitudinal location of the collision (otherwise known as the vertex). Due to budget constraints, each BBC has a limited timing resolution of ~1 ns which gives a minimal spacial resolution of 60cm from the coincidence requirement. Therefore, one cannot get a precise handle on the position of the vertex and other methods must be used to determine the vertex, as will be discussed in Section 3.4.

Zero Degree Calorimeters

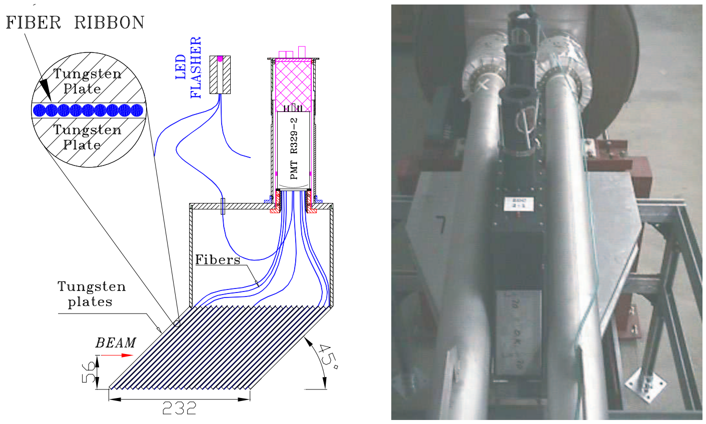

(a) **(b)**

Figure 2.9: (a) Diagram of Zero Degree Calorimeter (ZDC) layout. (b) Picture of mounted ZDC between the RHIC beam lines.

In the deuteron+gold run, a very different trigger was used. It used one of the Zero

Degree Calorimeters (ZDCs) [18]. The ZDCs are hadronic calorimeters that lie ±18 meters from the nominal interaction point along the beamline, as shown in Figure 2.6. They have an angular acceptance of ∼2.5 mrads and they lie along the beamline just after the DX Magnets. Since the DX Magnets sweep away charged particles, including the beams, only neutrons enter the ZDCs' acceptance. Each ZDC consists of 3 sets of 27 Tungsten plates with fibers embedded that carry the scintillation light to a PMT as shown in Figure 2.9(a). In the Au+Au run, a coincidence of the two ZDCs was used as a trigger, but in the d+Au run only the ZDC in the fragmentation direction of the gold beam was required to fire. The trigger efficiency in d+Au collisions will be discussed in detail in Appendix F. Other uses of the ZDC, such as centrality selection in the d+Au run will also be discussed.

2.2.2 Tracking Detectors

The Time Projection Chamber

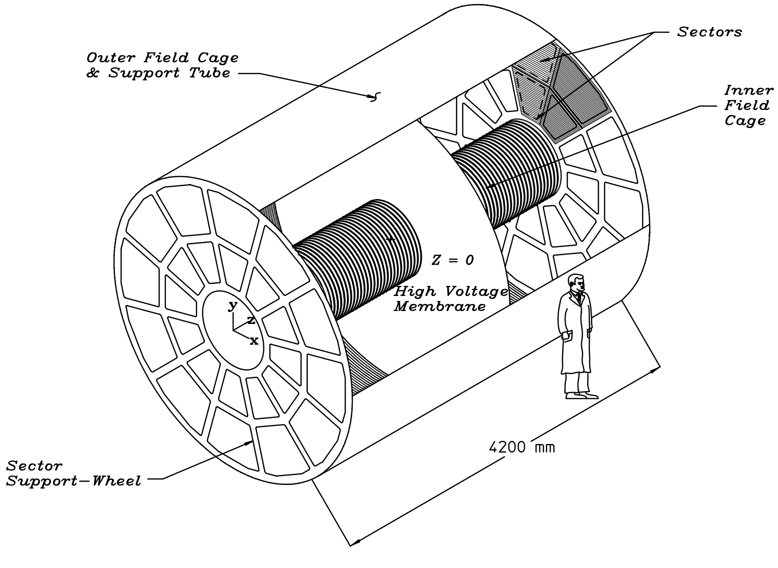

Figure 2.10: The Time Projection Chamber (TPC) layout.

The main detector in STAR is the Time Projection Chamber (TPC) as shown in Figure 2.10 [20]. The chamber is 4.2 m long and 4 m in diameter. The active dimensions radially are from 50 cm to 200 cm. It provides tracking for charged particles with $|\eta| < 1.8$ and has full azimuthal coverage and symmetry. It can measure the three-dimensional position of up to 45 points on a track as the particle traverses the active radius of the TPC. It has very high tracking efficiencies and accurately reconstructs the momentum of the track as will be discussed in Section 3.5.

Electrons are produced when charged particles ionize the P10 gas (10% Methane / 90% Argon) which is held at atmospheric temperature and atmospheric pressure + 2 millibars. The slight overpressure prevents impurities in the laboratory air from leaking into the detector. The gas is cleaned constantly to remove electro-negative impurities such as water and oxygen that capture electrons, thus reducing the efficiency of the detector. A central membrane cathode constructed from kapton is held at 28 kV and the shield grids at the end-caps are held at ground. This causes the ionized electrons to drift from the central membrane to the end-caps, therefore one can think of the TPC as two independent chambers that are placed together. Along the inner and outer field cage, located at 50 cm and 200 cm respectively, there are 183 precision 2 MΩ resistors which provide a uniform electric field of 135 V/m between the central membrane and the end-caps. This uniform electric field is needed to ensure a constant electron drift velocity throughout the chamber. The combination of the 135 V/m field and the P10 gas results in an electron drift velocity of 5.45 $\frac{cm}{\mu\text{s}}$. It takes approximately 40 μs to drift the electrons through the entire 2.1 m drift distance. The drift velocity is checked periodically throughout the run with a laser calibration system.

Once the electrons drift to the end-caps, they are detected by a Multi Wire Proportional Chamber (MWPC) with pad readout. A diagram of the wire configuration is shown in Figure 2.11. The first element the drift electrons encounter is the gating grid. The wires are made from gold plated copper and beryllium with a diameter of 75 μm and are parallel with 1 mm separating each wire [22]. The gating grid prevents un-triggered events from reaching the rest of the readout detectors and electronics. When a trigger is received, the grid is opened by holding the wires at equipotential relative to the surrounding material (110 V) which allows the drift electrons to pass.

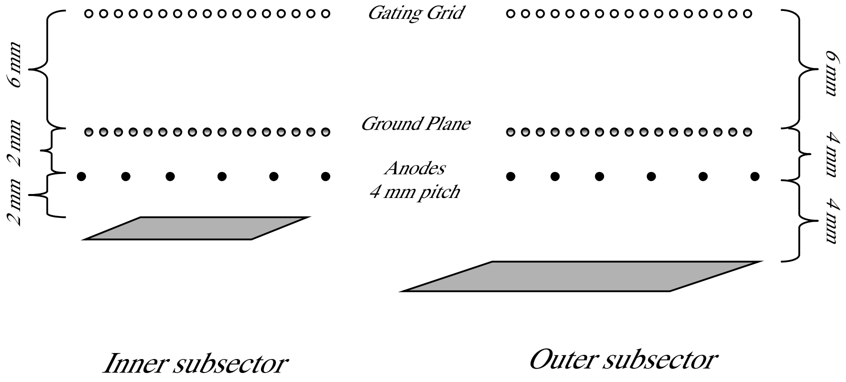

Figure 2.11: The Time Projection Chamber (TPC) wire configuration. Notice different dimensions for inner and outer sectors. From [21] corrected by the author.

When the grid is in the closed state, the wires are alternately held at +75 V and -75 V from the equipotential value. This collects the drift electrons and any remaining positive ions ($P10^{+1}$) from the previous readout. A diagram of the electric fields of a gating grid is shown in Figure 2.12.

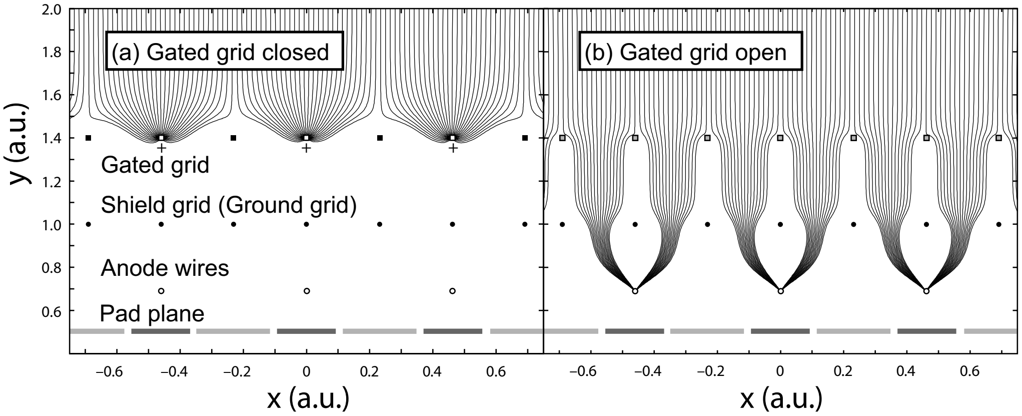

Figure 2.12: Operation of a gating grid. Figure taken from [23].

Next the electrons come across the shield grid, which is held at ground relative to the central membrane and defines the end of the drift. It is constructed from the same material and has the same spacing as the gating grid. The electrons do not terminate on the shield grid because of the high potential anode wires behind the shield grid. The shield grid serves two other purposes: it reduces the induction of charge on the pad plane from the gating grid and it collects the positive ions created near the anode wires.

Once the drift electrons pass the shield grid they approach the anode wires. The anode wires are 20 μm diameter gold plated tungsten wires that are parallel to each other with 4 mm between each wire. They are 2 mm from the inner pad plane or 4 mm from the outer pad plane. They are held at a high positive potential (1170 Volts for the inner sector or 1390 Volts for the outer sector). This creates large electric field gradients near the wires, which causes the electrons to accelerate quickly towards the anode wires. Because the P10 gas is also in this region, as the electrons accelerate towards the wires they ionize the gas. These ionized electrons are accelerated towards the wires and the cycle repeats. Approximately 1000-3000 electrons are created near an anode wire for every 1 drift electron. This in turn leaves a cloud of positive ions around the anode wire which induces a image charge on the segmented pad plane.

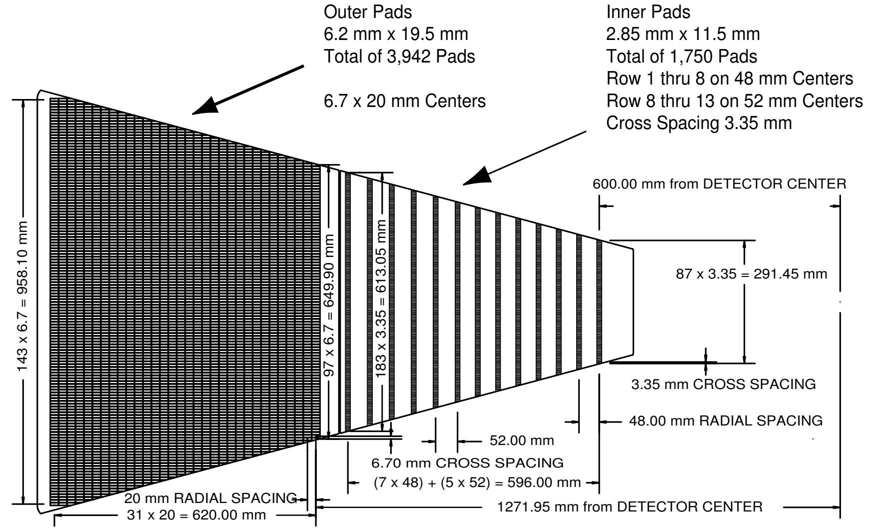

Figure 2.13: The TPC sector and readout pad layout.

One sector of the pad plane is shown in Figure 2.13. In each end-cap of the TPC there are 12 of these sectors arranged in a pie shape, with 3 mm of dead space between each sector. The pads are etched onto large multi-layer NEMA G-10 circuit boards. In order to be gas tight, there are no perforations on the circuit boards. Each sector is divided into an outer and an inner subsector. In the inner sector, which measures the highest track density, there are 1,750 pads and each pad is 2.85 mm × 11.5 mm. The first 8 rows of pads are 48 mm apart and rows 8 - 13 are 52 mm apart. The outer sector has 3,942 6.2 mm × 20 mm pads. They are arranged in 32 rows with 20 mm between each row. The pads are smaller on the inner sector to maximize the two-hit resolution. They are at different distances from the anode wires to confine the induced charge to 3 adjacent pads to facilitate cluster finding.

Since the pad planes are on the end-caps, the hit pad location determines the radius (r) and azimuth (ϕ) of the original ionized electron from the track. The third dimension (z) is determined from the time the pad is read out after the initial start time (TO) of the event. The electrons drift from the central membrane to the end-caps at 5.45 $\frac{cm}{\mu s}$ and this can be used to convert the arrival time to the original position in z. Each TPC pad can digitize 512 time bins with Δt = 100 ns. In actuality, a single drift electron leaves a signal in many adjacent r,ϕ, and z bins (typically 27) and a cluster finding operation is used to convert the pad topology into a single three-dimensional position.

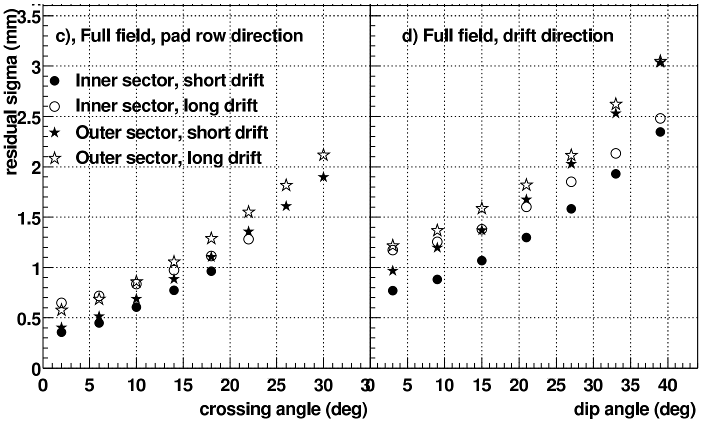

Figure 2.14: The TPC hit resolution in the (left) transverse and (right) longitudinal direction. Figure taken from [20].

The hit resolution is shown in Figure 2.14. The left half of the figure shows the resolution in the transverse plane versus crossing angle, which is is the angle between the particle's momentum that generated the hit and the pad row. The right half of the figure is the hit resolution for the longitudinal direction versus dip angle, which is the angle between the particles momentum and the longitudinal axis. The resolution worsens at higher angle because the electron clouds become more elongated in the drift direction. The resolution is larger in the longitudinal direction because of the 100 ns time bins (or .54 cm in space). The inner sector has a better resolution because of the smaller pad dimensions. Also notice the hits that drift the least, e.g. occur closer to the ends of the TPC, have a better hit resolution as the electron cloud has less time to diffuse.

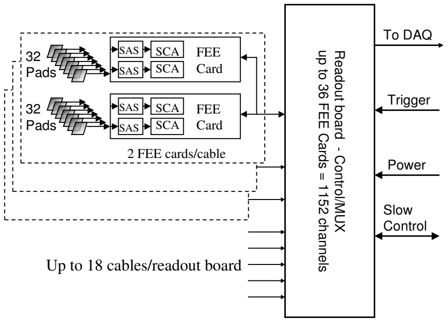

Figure 2.15: The TPC Front End Electronics (FEE) layout.

Sophisticated custom electronics were produced to read out and digitize signals from the TPC. A diagram of the read-out Front End Electronics (FEEs) is shown in Figure 2.15. Each FEE card accepts the analog voltages from 32 pads. The signals first go through the STAR preamplifier/shaper (SAS) chip. The SAS contains low noise integrating preamplifiers, 2-pole shapers and buffers. The SAS chip has 16 channels, thus each FEE card contains two SAS chips. After the SAS chip the signals are fed into a switched capacitor array/ADC chip (SCA/ADC), each with 16 channels. This chip samples the signals every 100 ns creating the 512 time bins mentioned earlier. It also contains a Wilkinson analog to digital converter (ADC) which maps the analog voltages to a 12 bit digital number by using a Grey Code counter. Next the signals from 36 FEE cards go to a readout board (RDO) which gathers the signals and sends them over a 1.2 Gbit/s fiber optical link to the computers in the Data Acquisition (DAQ) System. The DAQ System builds the event from all the RDO boards and writes the event to disk. A zero-suppressed empty event with just the background detector noise is approximately 1 MB in size while zero-suppressed central Au+Au event is upwards of 12 MB in size.

The Solenoidal Magnet

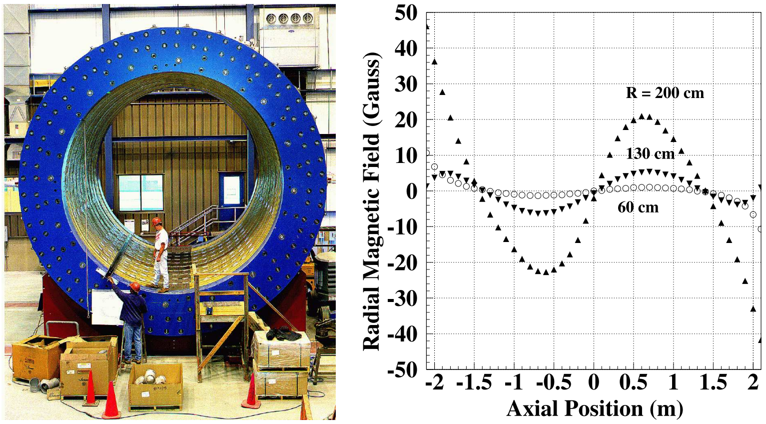

(a) (b)

Figure 2.16: (a) Picture of the STAR magnet without the TPC. (b) Plot of magnetic field distortions across the TPC. Figure taken from [24].

In order for the TPC to reconstruct the momentum of a track, a magnetic field must be applied. This magnetic field will bend the trajectory of the tracks and by analyzing the curvature the momentum can be extracted as discussed in Appendix B. The STAR magnet is a large cylindrical conventional coil with an outer diameter of 7.32 m and an axial length of 4 m as shown in Figure 2.16(a). It is constructed from 1100 tons of aluminium insulated with fiberglass cloth. The magnet consists of the main coils, field correcting trim coils and two pole-tips. When running at the maximum setting of 0.5 Tesla, the electric current through the magnet is approximately 5000 A with a total power consumption of 3.5 MW. In order to dissipate this heat, a closed water cooling system flows 1200 GPM of 24° C water at 200 PSI across the coils to cool the magnet to 29° C.

The magnetic field applied in this analysis is 0.5 Tesla, however the magnet is capable of delivering 0.25-0.5 Tesla. The polarity of the magnet can be switched and was switched once during both the p+p and the d+Au run to understand systematic errors. The magnetic field variation across the chamber is less than 50 Gauss as seen in the right panel of Figure 2.16. The magnetic field was mapped with Hall probes, and the field map is accurate to ±0.2 Gauss and is used during tracking [24, 25].

The Forward Time Projection Chamber

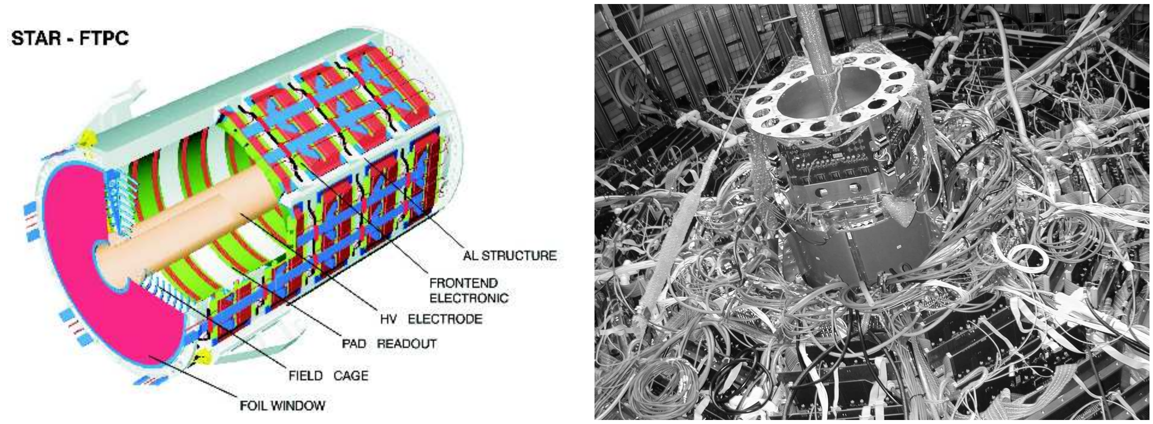

(a) (b)

Figure 2.17: (a) The Forward Time Projection Chamber (FTPC) layout. (b) Picture of one FTPC installed in STAR. The beamline is protruding from the FTPC and directly behind one can see the electronics for the main TPC.

The two Forward Time Projection Chambers (FTPCs) are radial drift chambers constructed to extend the phase space coverage of the STAR experiment to $2.5 < |\eta| < 4.0$. Each chamber is located along the beamline 210 cm from the center of the TPC. The FTPC is a cylindrical structure 120 cm long and 75 cm in diameter. It has an active volume from 7.73 cm to 30.05 cm radially and 93.7 in length as shown in Figure 2.17(a). Placed at the outer radius are 19200 1.9mm × 20mm pads which sample 256 time bins of 213.5 ns each. As opposed to the main TPC, the FTPCs drift electrons radially, from the inside wall which is held at ground, to the outer wall which is held at 10-15 kV. This non-uniform electric field leads to a drift velocity of 0.3-2.0 cm/μs. The maximum drift time is 50 μs for the maximum drift length of 23 cm. The gas mixture is 50% Ar and 50% $C0_2$ which provides a electron gain of 1-2$\times 10^3$ [26]. The FTPC uses a pad chamber and electronics system which is similar to that of the main TPC.

The mathematics of tracking are a little more difficult in the FTPCs because the magnetic field and the FTPCs' electric field are perpendicular, so $\vec{E} \times \vec{B}$ effects can be quite large. Also, because tracks in the FTPCs are almost parallel to the 0.5 T magnetic field, they undergo very little magnetic deflection. Due to these constraints, the FTPCs deliver a position resolution of 100 μm and two track separation of 1 mm. The momentum resolution is between 12 and 15% and the overall reconstruction efficiency is between 70 and 80%. During the p+p run, the detectors were still being commissioned, but in the d+Au run they were used to measure the track multiplicity in the high rapidity region as will be discussed in Section F.4.

Central Trigger Barrel (CTB)

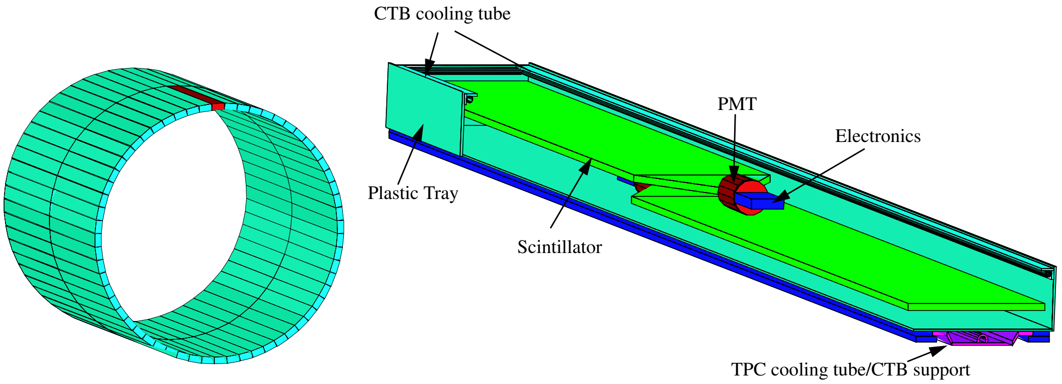

Figure 2.18: The Central Trigger Barrel (CTB) layout.

The Central Trigger Barrel (CTB) is an array of 240 scintillating slats that surround the TPC as shown in Figure 2.18. The slats are located 213.6 cm radially from the nominal beamline. Each slat is 1 meter long and covers 6 degrees in azimuth. There is a magnetic field shielded PMT that is optically coupled directly to the slat. There are two slats on each side of the central membrane and one of these groups is shown in the right of Figure 2.18. Sixty of these groups are required to cover the entire azimuth as shown in the left of Figure 2.18. With respect to the center of the TPC, the CTB has a pseudorapidity coverage of $|\eta| < 1$. Although the CTB has a large pixel size, it can be read out quickly because the PMTs and electronics are located on the scintillator slats. The CTB, therefore, is read out every bunch crossing.

Most previous analyses at STAR have used the CTB as a multiplicity counter, but this analysis pioneered its use as a tracking detector. A track found in the TPC can be associated with a hit in the CTB, giving the track a fixed point in space and time. If the event multiplicity is low enough, the large pixel size does not hinder the association. The usefulness of the TPC to CTB track matching will be explained in Section 3.2.1.

Silicon Vertex Tracker

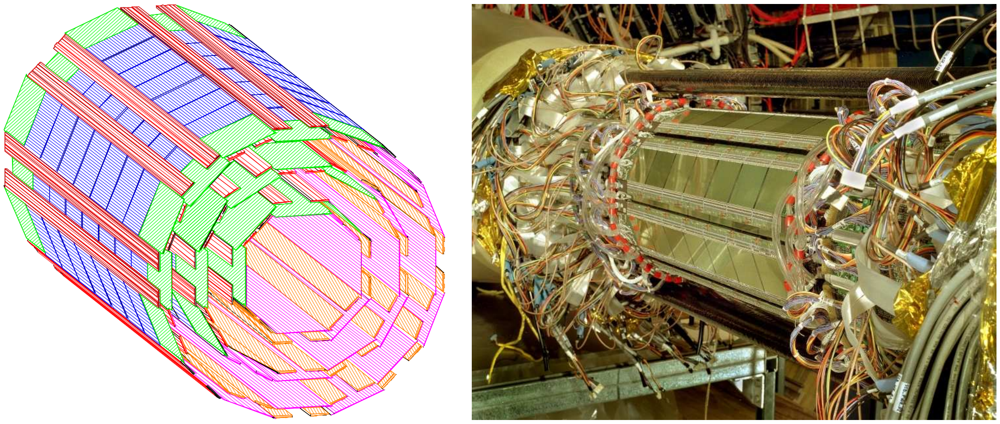

(a) **(b)**

Figure 2.19: (a) The Silicon Vertex Tracker (SVT) layout. (b) Picture of the SVT.

The Silicon Vertex Tracker (SVT), is a solid state drift detector located just outside the beam pipe [27] designed to improve the measurement of the vertex and track parameters to a higher precision than the TPC alone. The total active length of the SVT is 44.1 cm and it covers the full azimuth and $|\eta| < 1$. The detector is made up of 216 independent wafers that measure 6.3 cm × 6.3 cm. There are 3 layers of wafers at 5.97 cm, 10.16 cm and 14.91 cm as shown in in Figure 2.19. The inner layer has 32 wafers: a group of 4 wafers across on a ladder and 8 of these ladders around the radius (4×8). The middle has 12×6 wafers and the outer has 16×7 wafers. The wafers are effectively split in two and are read out at both ends. 1500 Volts is applied across each half wafer, leading to maximum drift time of 4.5 μs. There are a total of 480 anodes read out per wafer. The signal from each anode is sampled and stored in a Switched Capacitor Array (SCA) with a depth of 128 capacitors. This effectively creates a detector with 256 × 240 pixels per wafer and a pixel size of 250 μm × 250 μm.

The SVT has a position resolution better than 25 μm. In a high-multiplicity Au+Au event, this can be used to improve the vertex finding resolution [22]. The overall tracking efficiency for the SVT is approximately 80%. The momentum resolution is also greatly improved with the SVT. Since the SVT only covers 44.1 cm longitudinally, events must also lie in this range for the SVT to be effective. Unfortunately, the accelerator provided many events outside this range, contrary to the design plans. This effectively caused the SVT to have a limited event acceptance. Because of the limited acceptance and the fact the SVT was still being commissioned for this analysis, the SVT was not used for physics in this analysis. However, this analysis did use the SVT to calibrate the CTB and it will be discussed in Section 3.5.2.

Chapter 3

Data Analysis

Although similar analyses of inclusive charged hadron $p_\perp$ spectra have been done for STAR Au+Au data [19, 28], this analysis is the first from the proton+proton (p+p) run. The high luminosity, but low particle multiplicity p+p environment poses many analysis challenges not present in the high particle multiplicity, but low luminosity, environment of Au+Au collisions. The main challenge of the analysis is separating the signal from the many sources of background. Alternate novel analysis methods were developed to address these unique challenges.

3.1 The Standard Method of Vertex Finding

The standard method of separating signal tracks from background tracks in this type of analysis is vertex finding. The vertex of the collision is the point where the two nuclei collide. Figure 3.1(a) shows the side view of the STAR Time Projection Chamber (TPC) in a high multiplicity proton+proton event. In the figure, the beams enter from the left and the right through the beam pipe which is represented by the two center-most horizontal lines. The beam pipe can be seen more easily as the innermost circle in the end view shown in Figure 3.1(b). The color scale of the tracks is based on the $p_\perp$ of the track, with low $p_\perp$ tracks shown in blue and high $p_\perp$ tracks shown in red. Most of the tracks originate from a point near the center of the TPC; this point is called the vertex and is symbolized on the event display as a red star. Tracks that come from the vertex are primary tracks and they are the signal. Tracks that do not project to the vertex are background tracks. These background tracks have many sources: pileup, cosmic rays, and decays of primary tracks which all will be discussed.

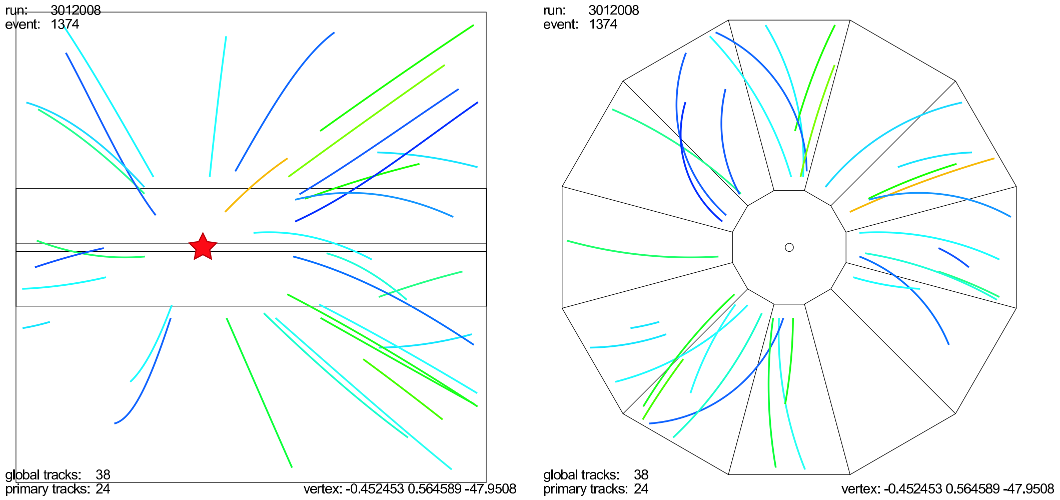

(a) **(b)**

Figure 3.1: (a) Side view and (b) end view of a proton+proton event. The software assigned vertex position is symbolized with a red star.

Whereas in a fixed target experiment, the vertex must be within the target, RHIC, which has colliding beams, has primary vertices located anywhere along the beamline. If the bunches are not steered or collimated well, the vertex can wander longitudinally. When the vertex is close to the edge of the TPC, many of the tracks will not be reconstructed because they do not fall within the acceptance of the TPC. Therefore, the vertex position must be constrained to near the center of the TPC in order to maintain a uniform acceptance. Figure 3.2(a) shows the longitudinal vertex position distribution for the entire p+p run. The distribution is very wide, therefore many outlier events need to be rejected. The actual cut applied will be discussed in Section 3.6.4. The transverse position of the vertex is more constrained because it must occur within the 3 cm beam pipe and does not depend strongly on the bunch timing. Figure 3.2(b) shows the transverse position of the vertex for the p+p run which is grouped very tightly, but offset from the radial center of the TPC. The color scale is logarithmic and indicates the number of events occurring at that radial position.

In the standard method of vertex finding, a minimization is performed to find the vertex. Schematically, what is done is to minimize the distance of closest approach of all the tracks in the event. If a track comes from the vertex, one would expect the

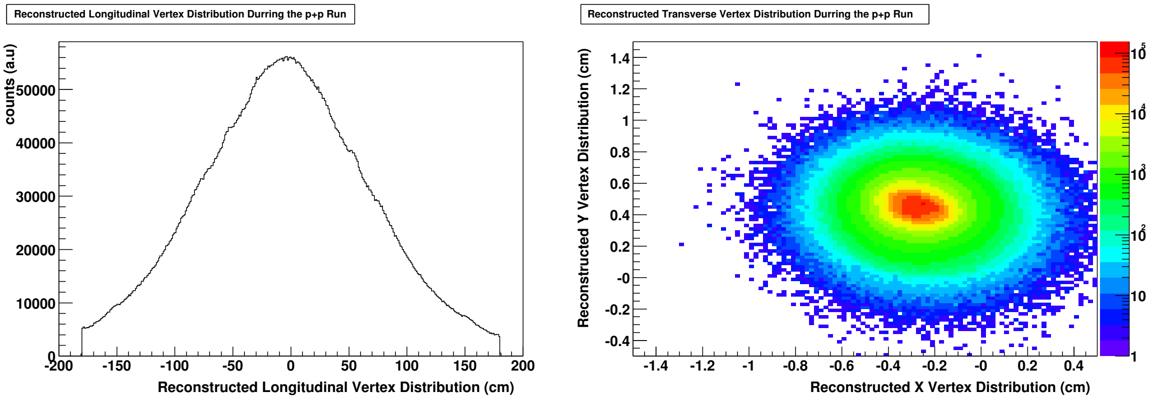

(a) **(b)**

Figure 3.2: Proton+proton reconstructed vertex distributions in the (a) longitudinal and (b) transverse directions.

distance of closest approach (DCA) of a track to the vertex to be zero. An iterative approach is used to remove the outliers in order to find a more precise vertex location. The software package that performs this function is referred to as the proton+proton Low Multiplicity Vertex (ppLMV) finder [29].

The quantity that is minimized is:

$$\chi^2 = \frac{1}{N}\sum_{i=1}^{N}\frac{\Delta x_i^2}{\sigma_i^2} \tag{3.1}$$

Where Δx_i is the distance of closest approach between the requested vertex and the current track; σ_i is the error on Δx_i and is a function of momentum and other track parameters [30]. The error can also be used as a weighting function to give a larger influence on the vertex for certain "high quality" tracks. For example, a high $p_\perp$ track has a small curvature and undergoes less scattering with respect to a low $p_\perp$ track. Therefore, high $p_\perp$ tracks should have a smaller error when projecting back to the vertex. Remember, the TPC does not measure tracks until at least 50 cm from the vertex point as shown in Figure 3.1(b), so extrapolations must be made.

In the Au+Au data sets, this fit function was calculated in all three dimensions. In a Au+Au event there are approximately 5000 tracks per event, so there are sufficient constraints to produce a reliable and accurate fit. However, in a p+p event, there are far fewer tracks as will be discussed in Section 4.2.2, so extra constraints

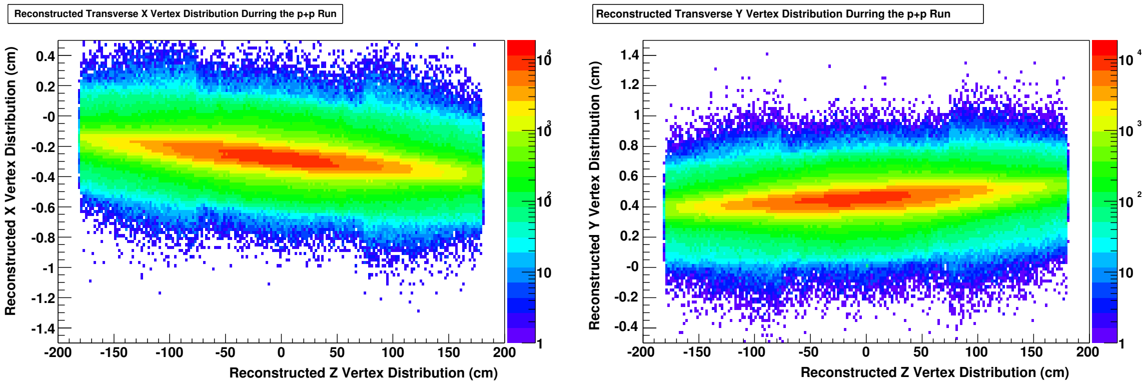

(a) **(b)**

Figure 3.3: Proton+proton transverse versus longitudinal reconstructed vertex location in the (a) X and (b) Y transverse directions.

must be added to produce a reliable fit. Since the transverse position of the beam is very well confined, as shown in Figure 3.2(b), this can be used as a constraint on the vertex position. The ellipsoidal feature of the figure is due to the changing transverse positions of the beam with respect to the longitudinal position which is shown in Figure 3.3. In order to use this as a constraint, the standard vertex finder is run without restrictions on the transverse position. The transverse position versus the longitudinal position is then parameterized by a fit, which is referred to as the beamline. The vertex finder is then rerun with the beamline added in as a highly weighted track. This effectively constrains the vertex to lie along the beamline. Since the beam steering changes every time RHIC is filled, a beamline parametrization is calculated for every run.

3.2 Event Pileup

There are other challenges that make vertex finding and separating signal from background tracks difficult. One of the main challenges to overcome in the p+p data set is the high event rate coupled with the relatively slow TPC drift time. As described in Sections 2.1.2 and 2.2.2, the TPC integrates its readout over 40 μs and but an event can occur every 213 ns. Therefore it is possible to have 188 events occur during the readout of a single triggered event. Fortunately, the probability of a bunch crossing producing an event is much lower than this ratio. The probability of a bunch crossing producing an event depends on the luminosity of the beam, but has a maximum value of 0.5% during the p+p run as discussed in Appendix D. However, there is still some probability of two or more bunch crossings producing events in the same readout window. This phenomena is called pileup and is a common concern when working with drift chambers. It is also possible for pileup to occur from two collisions in a single bunch crossing, but the probability for this is much lower as it is the square of the above probability.

Pileup manifests itself in a unique way in the Time Projection Chamber (TPC). Since the electric drift field does not turn off between triggers, the electrons are always drifting from the central membrane to the end-caps. Moreover, the longitudinal position of the TPC points is determined by the difference between the start time of the event (T0) and the readout time. If two events occur at different times, but use a common T0, then the longitudinal position of the tracks from at least one of the events will be wrong. Figure 3.4 shows three real events that are typical examples of pileup in the TPC. A non-pileup event is shown in Figure 3.1.

Figure 3.4(a) shows a pileup event. The triggered event occurred first and can be seen at the center of the TPC. The second event can be seen at the far right of the TPC. Because the tracks that come from this event are split across the central membrane, one can discern that this event happened after the first event. It appears to be split in two because the electrons drifted towards the closest end-cap. This order of events causes the software to assign the wrong position to the tracks. The true position of the pileup event can be found by moving both halves of the split event towards each other until they line up.

At first sight, Figure 3.4(b) appears to show a normal event. However, if one looks closely, the tracks going to the right point to a different place than the tracks going to the left. Because both events happen close to the central membrane and close in time, one does not see the track splitting that helped identify the previous event as pileup. From topology alone, it is difficult to identify which, if any, of these events is the true event.

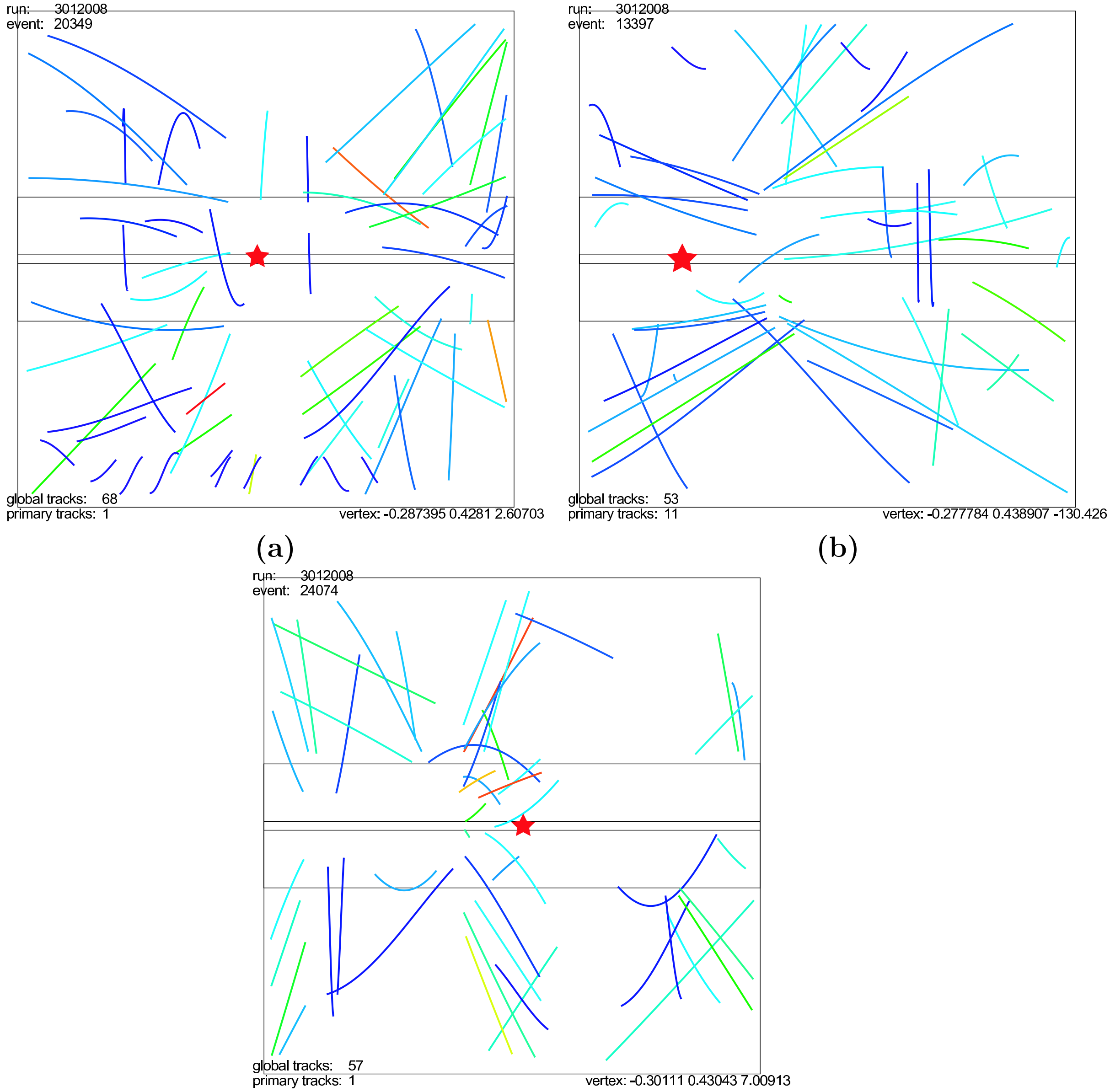

(a) (b)

(c)

Figure 3.4: Pileup events in the TPC. The software assigned vertex position is symbolized with a red star.

Figure 3.4(c) shows another example of pileup. First notice the two clusters of tracks near the end-caps of the TPC. They are from an event that occurred before the triggered event. By the time the trigger occurs, the electrons are located near the end-caps. A second event can be seen just left of center. However, one only sees the particles going to the right from this event. This leads one to believe that this is also a pileup event that actually occurred at the left end-cap at the very end of the drift period.

Because of very different topology of pileup events, it is difficult to identify them, and even more difficult to decouple the individual events from topology in the TPC alone. If these events were not identified, much of the analysis would be tainted. For instance, if the pileup events were treated as normal events, they would have roughly twice the number of particles per event. Any analysis that compares the relative location of particles would be biased as well due to tracks being reconstructed in the wrong position.

3.2.1 Methods To Remove Pileup

Fortunately, one can exploit other detector elements of STAR in order to eliminate pileup. The Central Trigger Barrel (CTB) as discussed in Section 2.2.2 can be used to untangle the pileup event from the triggered event. The CTB is read out at every possible bunch crossing, therefore one can match TPC tracks to the CTB. If the TPC track matches a CTB hit that is in time with the trigger, one determines that the track most likely came from the triggered event. Not all tracks that come from the triggered event will match to the CTB because a track must reach the CTB and not exit the TPC through the end-caps. This requires the track to have a $p_\perp$ of at least 160 MeV/c in order to reach the 213 cm radius of the CTB while being bent by the 0.5 Tesla magnetic field as discussed in Appendix B. One must also take into account the CTB efficiency and two tracks projecting to the same CTB slat, but this can be corrected for and will be discussed in Section 3.5.2. Nevertheless, the CTB is a good detector for rejecting pileup. Figure 3.5(a) shows the relative track matching probability of the CTB: the ratio of the number tracks that match hits in the CTB to the number of tracks that are within the acceptance of the CTB. This is a measure of pileup because as pileup gets larger, fewer tracks will match to the CTB.

One expects the pileup to be proportional the luminosity of the beams. If there

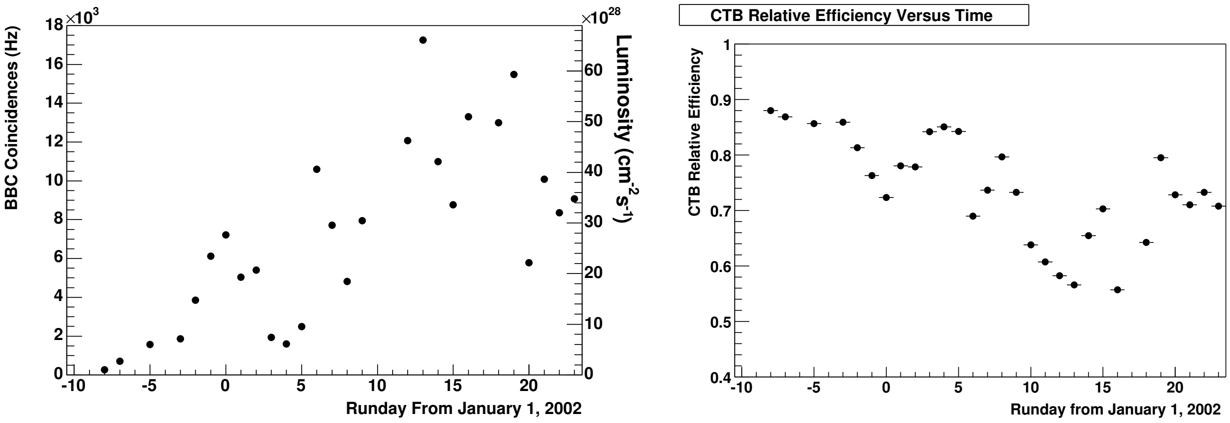

(a) (b)

Figure 3.5: (a) Relative RHIC luminosity and (b) CTB matching efficiency during the p+p run.

are more ions in each bunch, there is a higher probability to have a collision in each bunch crossing. Therefore, one would expect the CTB relative matching efficiency to decrease as the luminosity increases. The luminosity, in fact, did increase as the operators became more experienced at storing the beams. Figure 3.5(a) shows the number of BBC triggers received by STAR per second. This is the RHIC luminosity if one divides by the trigger cross section, σ_{BBC}, which will be discussed in Section 3.6. Figure 3.5(b) shows the CTB relative matching efficiency. The two plots are inversely proportional, indicating that the luminosity increased over time leading to higher pileup rate.

We can now employ CTB matching to assist in identifying pileup. Figure 3.6 shows the same events as in Figure 3.4, but the tracks that do not match the CTB are now shown as dotted lines. Although the event shown Figure 3.6(a) was easy to identify as pileup from topology alone, one can see that most of the solid tracks point back to the event located at the center of the TPC. The pileup event at the far right of the TPC is pointed to mostly by dotted lines. CTB matching also helps in the understanding of the display of Figure 3.6(b), as one can see more easily the two separate events. The event with tracks going off towards the left is the pileup event, because most of the tracks do not match to the CTB. Many of the tracks going off to the right match the CTB, leading to the conclusion that this event must be

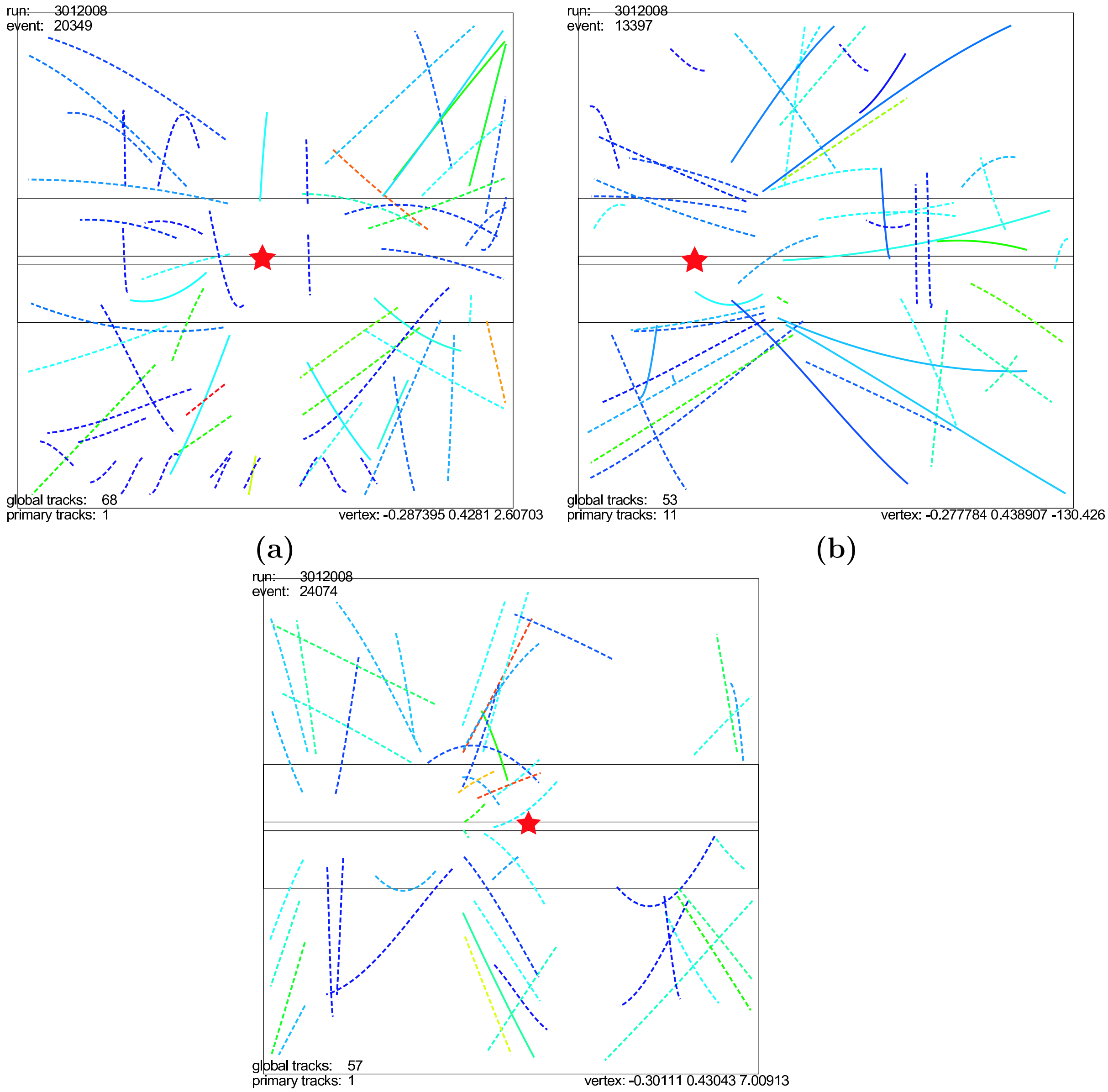

(a) **(b)**

(c)

Figure 3.6: Pileup events showing CTB matched tracks in the TPC. The software assigned vertex position is symbolized with a red star.

the original triggered event. Figure 3.6(c) shows that almost all tracks fail to match the CTB. This supports our previous conclusion that all the tracks shown are from pileup events. While event topology alone could not identify the pileup events, the

CTB provided the necessary information to untangle the events.

The CTB is an effective tool for identifying tracks that come from the current trigger, which allows us to untangle pileup events. The standard vertex finder however, does not use only CTB matched tracks to determine the vertex, because not all primary tracks fall within the acceptance of the CTB. Therefore, the standard vertex finder uses CTB matched tracks as a seed to begin the vertex finding. The vertex finder is allowed to wander from this seed position, which sometimes produces undesirable results. While seeding the vertex finder does help in vertex finding, pileup events still confuse the vertex finder as will be discussed in Section 3.3.

3.2.2 Cosmic Rays

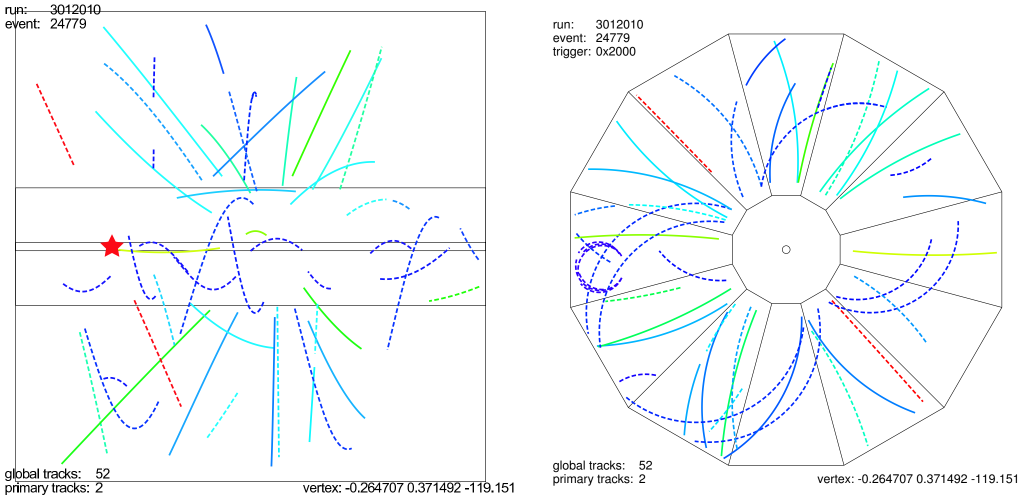

(a) **(b)**

Figure 3.7: (a) Side view and (b) end view of a proton+proton event with a cosmic ray. The software assigned vertex position is symbolized with a red star.

Another concern which is related to pileup is the effect of cosmic rays entering the TPC during a trigger. Cosmic rays are usually muons with $p_\perp$ greater than 8 GeV/c. Due to the $p_\perp$ weighting used in the standard vertex finder, these cosmic rays alone can define the vertex. For example, examine the event display shown in Figure 3.7(a). One clearly can see that most of the tracks and all of the solid CTB matched tracks come from a vertex located near the center of the TPC. However, notice the high $p_\perp$ red track in the left of the TPC. The vertex assigned to this event is the intersection of the red track with the beamline and not the true vertex. This occurs because the $p_\perp$ weighting of the vertex finder overruled the seed due to the CTB matching.

Fortunately, topological algorithms can be used to reject cosmic events. Since cosmic events occur at random, by rejecting these events there is no bias. One can readily identify cosmic tracks because they have very high $p_\perp$ and stream through both the top and bottom of the TPC. Sometimes the cosmic rays get split at the central membrane because they occur out of time with the trigger, but this still leaves two high $p_\perp$ tracks that are perfectly back-to-back in the r,ϕ plane as shown in Figure 3.7(b). This topology is easy to identify and the high $p_\perp$ bias which would result from their inclusion is removed by rejecting these events. This cut does not remove any significant signal in the high $p_\perp$ region.

3.3 Quantifying the Vertex Efficiency

The presence of pileup and having only a small number of tracks with which to fit the vertex sometimes causes the vertex to be found in the wrong place. Other times, the fits do not converge and the vertex is not found at all. One must therefore quantify the efficiency of the standard vertex finder to determine if a bias exists. In real data it is impossible to know where the actual vertex is located, so one must use simulations. In order for the simulations to be valid, they must accurately reproduce the detector environment. The main environmental background in the p+p data set is pileup, therefore it must be accurately reproduced. Although it is possible to simulate pileup, it would be much better to use real detector backgrounds and then overlay a simulated event. In Au+Au events, vertex efficiency and pileup was not a major concern, so this simulation infrastructure was specially created for this analysis.

The real detector backgrounds are taken from the abortgap events that are described in Section 2.1.2. In an abortgap event the detector is triggered but one of the beams does not have a filled bunch. This means a real collision could not have occurred. Therefore, the STAR TPC is recording the underlying background without

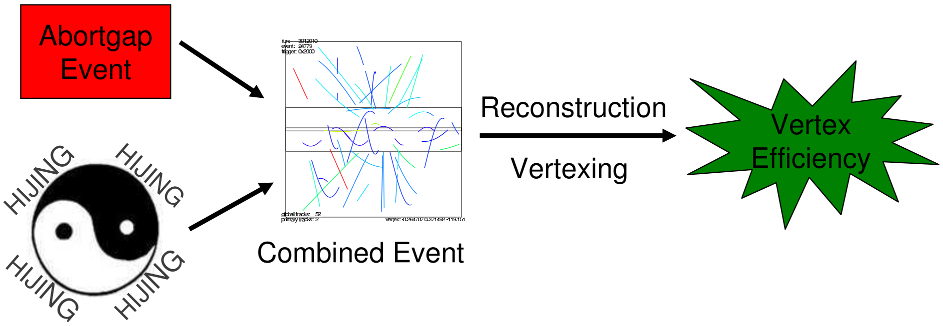

Figure 3.8: Vertex efficiency simulations flow chart.

a real event present. As one can see from Figure 2.5, there are very few events that occur in the abortgap. These rare events must be extracted from the raw data files. Once these events are collected, a simulated event produced by HIJING [31] is added into the abortgap event. The standard reconstruction and vertexing packages are then run just as if the abortgap+HIJING event is a real data event. The process is illustrated in the flow chart of Figure 3.8.

By comparing the vertex position from the simulated event versus the vertex position reconstructed by the standard software, one can extract a vertex resolution and vertex efficiency. Figure 3.9 shows the vertex resolution for p+p events in the above simulation framework. What is plotted is the residual (or difference) between the reconstructed vertex position and the simulated vertex position, for when the vertex is reconstructed. As one can see in Figures 3.9(a,b), both transverse positions are reconstructed with $\sim$0.08 cm resolution due to the beamline constraint. The longitudinal position is reconstructed less accurately (0.213 cm) than transverse directions as shown in Figure 3.9(c). Moreover, this resolution is only for events where the vertex finder returns a vertex and does not take into account when the fits do not converge and an error is returned. The above plots can be fit with a Gaussian to extract the resolution and the results are summarized in Table 3.1 and also compared to d+Au collisions.

In analyses of charged hadron spectra in Au+Au events [19, 28], tracks are considered background if they do not come within 1 cm of the vertex. Therefore, the

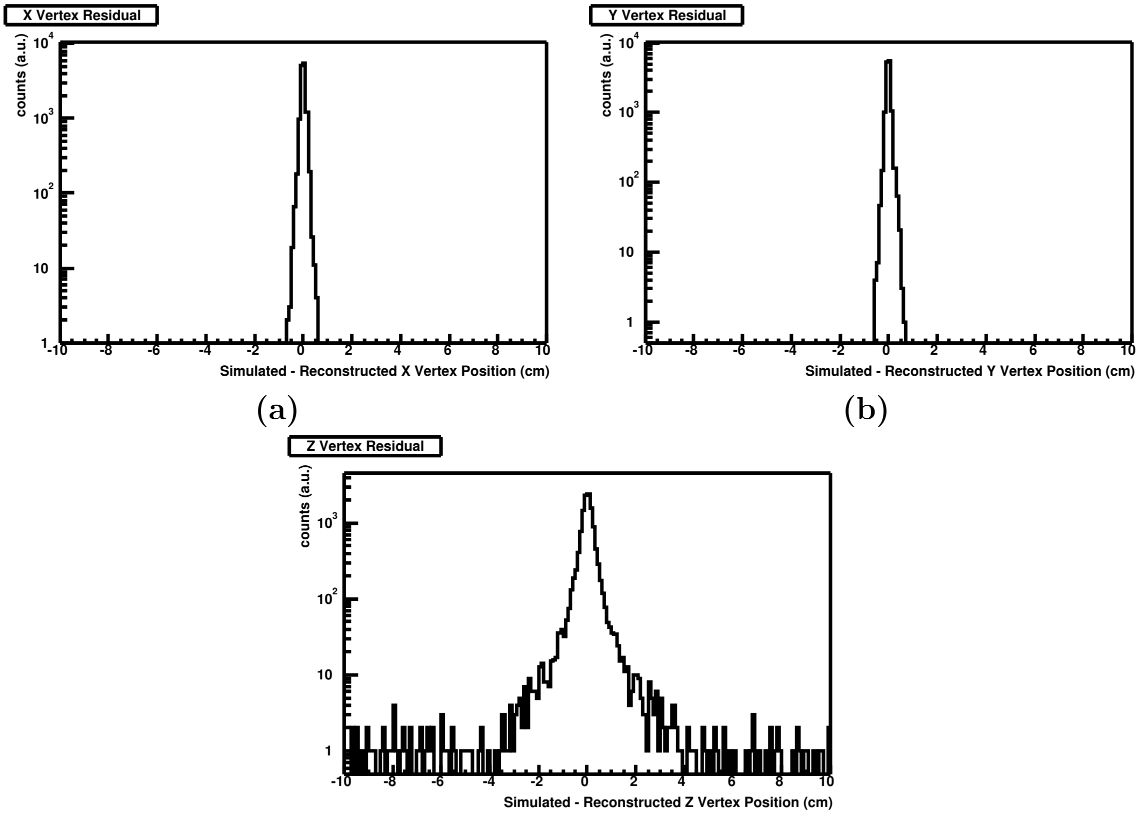

(a) (b)

(c)

Figure 3.9: Vertex location residuals: simulated - reconstructed (a) transverse X direction (b) transverse Y direction (b) longitudinal Z direction.

	X	Y	Z
Vertex Resolution p+p	0.083 cm	0.080 cm	0.213 cm
Vertex Resolution d+Au	0.059 cm	0.068 cm	0.149 cm

Table 3.1: Proton+proton and d+Au vertex resolution in the three spacial directions.

vertex is defined to be found correctly when it is within 1 cm longitudinally of the correct position. A vertex is defined to be found incorrectly, or contaminated, when the residual is greater than 1 cm. The final case is when the fits fail and no vertex is returned for the event. Table 3.2 summarizes these vertex efficiencies for the proton+proton simulated data set.

If the vertex inefficiencies were random, then this effect easily could be corrected.

Found Correctly $\Delta Z \leq 1$ cm	Found Incorrectly Δ Z > 1 cm	Not Found
81.5%	11%	7%

Table 3.2: Proton+Proton simulated vertex efficiency integrated over all multiplicities.

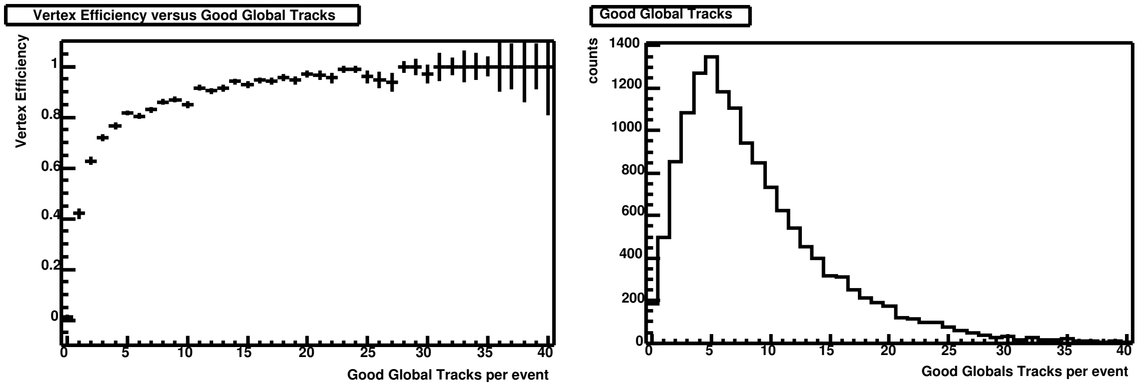

(a) (b)

Figure 3.10: (a) Vertex efficiency versus "Good Global Tracks." (b) Distribution of the number of "Good Global Tracks" per event.

However, if the vertex inefficiencies are a strong function of an observable, the observable will be biased. The most obvious observable to study is the event multiplicity, which is the number of tracks per event. One would except when there are fewer tracks in an event, the fits become more difficult. Figure 3.10(a) shows the vertex efficiency (residual < 1 cm) versus the number "Good Global Tracks" which are high quality tracks reconstructed in the TPC that came from the simulated event and not the pileup event. As one clearly can see this is a very strong function of multiplicity. Predominantly low multiplicity events are lost by the vertex finder. Figure 3.10(b) shows the input distribution of "Good Global Tracks". Notice much of the cross section lies in the inefficient region. If one takes the vertex efficiency shown in Figure 3.10(a) and integrates over the Good Global Track distribution shown in Figure 3.10(b), one will recover the integrated vertex finding efficiency shown in the first column of Table 3.2. This is a very large bias and cannot be ignored.

If this was the only factor to contend with, one could correct observables by weighting by the inverse of the vertex efficiency. However, the vertex contamination

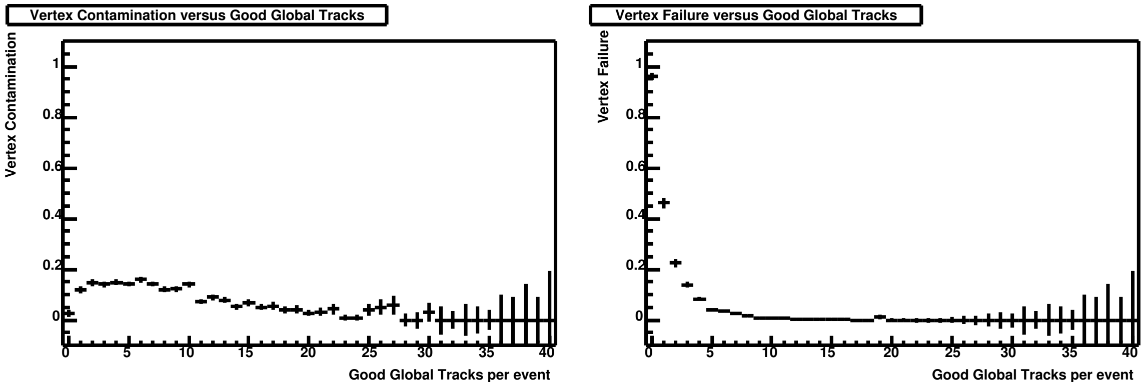

(a) **(b)**

Figure 3.11: (a) Probability of vertex contamination versus “Good Global Tracks.” (b) Probability of vertex finder failure versus “Good Global Tracks.”

and the vertex finder’s absolute failure are also strong functions of multiplicity as shown in Figure 3.11. Since there is no way to tell experimentally when the vertex is found in the wrong place, corrections based on vertex contamination become difficult. Moreover, placing the vertex in the wrong place has an undesired effect on tracking. In the standard tracking method, all tracks that are within 3 cm of the vertex are forced to intercept the vertex. Therefore, as described in Appendix B.1, the momentum of the tracks is altered. This effect is difficult to correct.

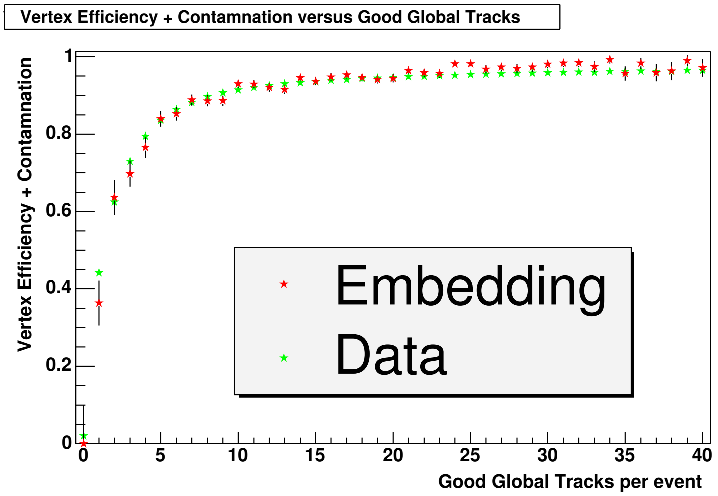

Figure 3.12: Vertex efficiency in data and simulation.

As there are very few abortgap events, obtaining a statistically significant sample is difficult. The abortgap sample is enhanced by looking at another trigger type, called zerobias. In zerobias events, the trigger is randomly fired, consequently it should accept mostly background events. The zerobias sample consists of approximately 150,000 events. Unfortunately, the zerobias events were taken only once on day 15 of the run when the pileup was the highest as shown in Figure 3.5. Since the frequency of pileup is time dependent, one would assume the vertex efficiency also will be. Comparisons of the vertex efficiency from abortgap and zerobias events, however, are consistent.

The embedded events are also generated with the HIJING model, therefore any corrections will be strongly dependent on this model. In addition, one needs to check if the simulations are consistent with data. Whereas in simulation one can discriminate between the actual event and pileup, this cannot be done perfectly in data. Therefore, when comparing simulation to data, one must redefine "Good Global Tracks" as all high quality reconstructed tracks in the TPC, thus relaxing the requirement that these tracks come from the simulated event. As already mentioned, one also cannot experimentally discern between correctly and incorrectly found vertices. However, we can compare the sum of these quantities in simulation with all found vertices in real data. This is shown in Figure 3.12. The magnitude and the dependence on multiplicity of vertex finding are consistent, although there is some discrepancy at low multiplicity. Nevertheless, one can claim that the abortgap and zerobias simulations reasonably reproduce the detector environment.

Although the data matches the simulation on average, using the vertex efficiency numbers to correct the data has many drawbacks. There is some discrepancy in the above vertex efficiency calculation in simulation and data at low multiplicity where much of the cross section resides. These corrections also should be time and luminosity dependent. Moreover, all corrections will be dependent on the particular model used to simulate entire events. Therefore, this analysis devised a new approach to vertexing to avoid these shortcomings.

3.4 An Alternative To Vertexing

By applying the lessons learned in evaluating the vertex finder one can devise a custom alternative to vertexing. In this analysis the main reasons for vertexing is to separate signal tracks from background tracks and to restrict the location of the event in the center of the TPC to maintain a constant tracking acceptance. If these two criteria are met, one can forgo traditional vertexing. With this type of method all vertex efficiency related corrections can be avoided.

In order to remove pileup, the CTB is used in a similar fashion as in the standard vertex finder. All tracks that fall within the desired kinematic region (namely pseudorapidity $|\eta| < 0.5$) are projected to the CTB and if they match to hit slats they are accepted. See Appendix B.3 for details on projecting tracks to the CTB. Whereas the standard vertex finder uses matched CTB tracks to find a seed, in this method all tracks that do not match the CTB are rejected summarily. A correction, as will be discussed in Section 3.5.2, is later applied to take into account the absolute CTB efficiency. As discussed earlier, this cut effectively removes pileup tracks.

Next, all tracks that match the CTB are projected to the beamline as defined in Section 3.1. Tracks are accepted if their distance of closest approach to the beamline in the transverse direction is less than 1 cm. This cut is used to be similar to the standard method of vertexing. See Appendix B.3 for details on projecting tracks to the beamline. Since the vertex must occur along the beamline, this cut removes many of the background tracks that cannot come from the primary vertex. The effect of this cut can be seen from simulations in Figure 3.13. This cut effectively separates most of the signal from the background in the same way as standard vertexing, albeit in only two dimensions. The remaining background can be corrected for statistically as will be discussed in Section 3.5.3.

Now that background tracks have been removed from the sample, one must restrict the location of the event to the center of the TPC. The longitudinal location of the beamline projection of all CTB and beamline matched tracks is determined. A pure arithmetic mean of this position for all tracks in the event is calculated. This mean longitudinal position (meanZ) is used as a pseudo-vertex. The resolution of the meanZ

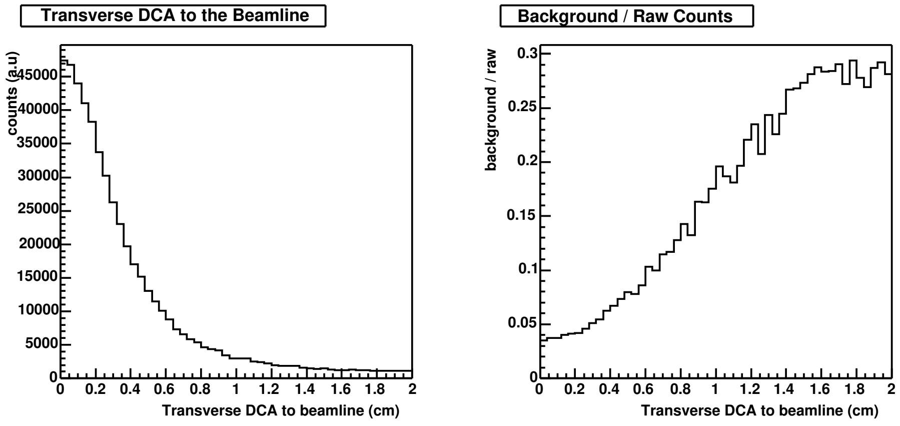

(a) (b)

Figure 3.13: (a) Transverse distance of closest approach (DCA) to the beamline for all tracks. (b) Ratio of background tracks to all tracks versus transverse DCA to the beamline.

position is shown in Figure 3.14(a).

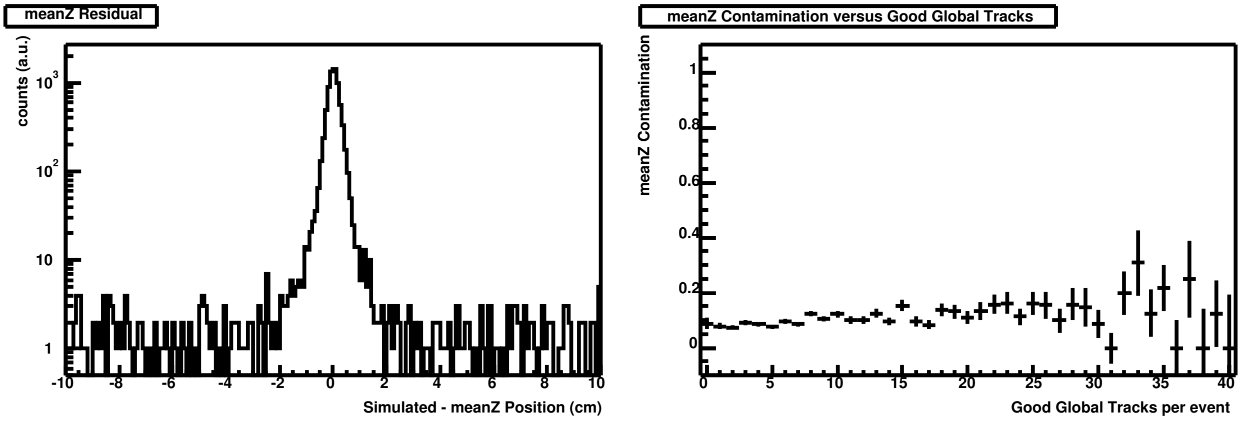

(a) (b)

Figure 3.14: (a) The meanZ position residual: simulated - reconstructed position. (b) meanZ contamination versus "Good Global Tracks."

What is striking is the contamination of this method, |meanZ - simulated vertex| > 1 cm, is no longer a strong function of multiplicity as shown in Figure 3.14(b). Therefore this can be used to restrict the event to the center of the TPC. The only effect the contamination has is that these events actually may have occurred slightly outside the desired acceptance window. This has a minimal effect because the momentum of the track is not refit to the meanZ position and the effects on efficiency can be corrected for as will be described in Section 3.5.2.

The meanZ method has several benefits to the standard vertex finder in a low multiplicity environment. This method only uses tracks that fall within the desired kinematic region and acceptance cuts. The standard vertex finder uses all tracks in the event, leading the inclusion of many background tracks. Another benefit is that the meanZ method does not fit the vertex position, it only performs an arithmetic mean. Therefore, it only returns an error if there are no tracks within the acceptance, while the standard vertex finder returns an error if the fits do not converge. Consequently, the only correction that needs to be applied is to account for events that fall within the center of the TPC, but do not produce any tracks in the acceptance. This correction will be discussed in Section 3.6.4.

As another alternative analysis, one could use the standard vertex finder only on events with tracks that satisfy the CTB and beamline matching constraint. This brings the vertex contamination of the standard vertex finder versus multiplicity in line with the meanZ method. However, one would still have to contend with the contamination affecting the reconstructed momentum of the tracks. Also, there is still some failure rate associated with this method. Therefore, this analysis solely uses the meanZ method because it effectively removes background tracks and constrains the events position without being strongly dependent on multiplicity or requiring model dependent corrections.

3.5 Corrections To the Data

Now that events and tracks have been selected, one can perform many different analyses such as studying the multiplicity and the $p_\perp$ spectrum. Before showing these results, however, corrections for detector efficiency must be performed in order to make legitimate comparisons to other experiments. Because the meanZ method is very different from previous analyses [19, 28] the correction methods will be discussed in detail.

3.5.1 Tracking Efficiency Corrections

Embedding

By using simulations, one can compare the input track distribution with the reconstructed track distribution to determine an efficiency. The simulated environment should be as close as possible to the real detector environment. A detailed simulation framework already has been designed, tuned, and used for the previous Au+Au spectra analyses. This framework incorporates the geometry of the detectors and energy loss in the various detector materials with the GEANT modeling program [32]. In this framework, one takes a real Au+Au event to act as the background and embeds a few simulated tracks emanating from the vertex of the real event. By running many events, these simulated tracks can be produced to cover the entire measured phasespace. Because this method only adds a few tracks into an event that already has approximately one- to five-thousand tracks, it does not distort significantly the event's multiplicity. This is important because previous analyses have shown the tracking efficiency is inversely proportional to event multiplicity. One then studies how the software reconstructs these added simulated tracks to compute an efficiency. This process is illustrated in Figure 3.15.

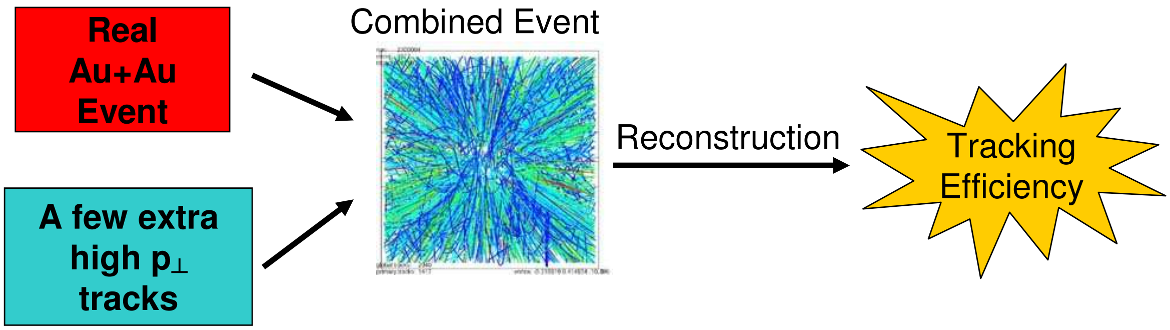

Figure 3.15: Gold+gold tracking efficiency simulations flow chart.

In the low-multiplicity p+p environment, the standard simulation framework must be modified for various reasons. First, since the vertex location in real data is often found in the wrong place, one could introduce serious errors by embedding extra tracks at the wrong vertex position. Secondly, one cannot add many tracks into each event, because these simulated tracks would comprise a significant fraction of the total event multiplicity, which would make the tracking environment unrealistic. For these reasons, the above embedding framework was redesigned specifically for this p+p analysis. Just as with the simulations produced for evaluating vertex efficiency, one takes an abortgap event as the background and adds in a full simulated HIJING event to realistically mock-up a real p+p event. As this analysis seeks to study high $p_\perp$ tracks, one needs an additional embedding step. Many HIJING events would have to be run in order to get a large enough sample of high $p_\perp$ tracks because high $p_\perp$ tracks are produced orders of magnitude less frequently that low $p_\perp$ tracks. Therefore, one adds a single extra high $p_\perp$ track into an abortgap+HIJING event at the HIJING vertex in order to study efficiencies in this region of phase-space. This method of embedding is illustrated in Figure 3.16.

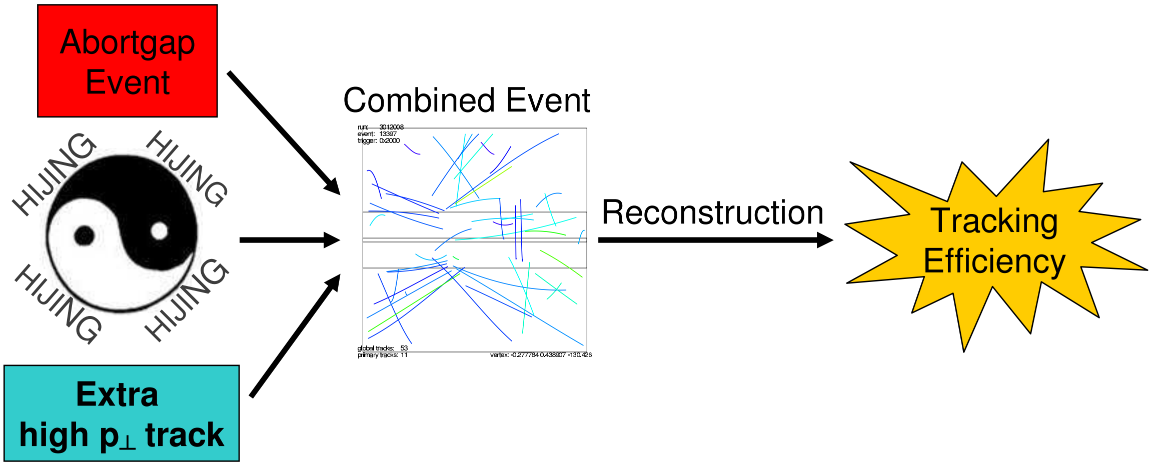

Figure 3.16: Proton+proton tracking efficiency simulations flow chart.

3.5.2 Tracking Efficiency

Now that a suitable embedding framework has been designed, one can perform the corrections. Efficiency corrections due to tracking in the TPC are applied first. As discussed in Section 2.2.2, there are some inactive areas in the TPC. Moreover, the tracking software used to group drift electrons into tracks, as discussed in Appendix

B.1, sometimes misses tracks. The ratio of the TPC reconstructed track distribution over the produced track distribution gives us the efficiency, ϵ_{TPC}. A more detailed discussion on how the efficiency calculations are done can be found in [19] and [28]. The efficiency corrections are functions of event and track variables. The previous analyses categorized the efficiency corrections on $p_\perp$, η, and z vertex. One would expect the efficiency to be dependent on these variables. For instance, high $p_\perp$ tracks should have a higher efficiency than low $p_\perp$ tracks because they undergo less scattering in the detector material. Tracks with $\eta \sim 0$ and/or tracks that come from events with a vertex near the center of the TPC should be more efficient because the tracks should pass through more active detector elements and do not exit the TPC through the inactive end-caps.

Although the meanZ position does give an approximate vertex position, one would like to avoid its use in tracking corrections and rely solely on track-based parameters. Instead, this analysis uses the z position of the first radial point reconstructed on the track (fpz). This variable, along with the standard $p_\perp$ and η variables will serve as the dependent variables for $\epsilon_{\mathrm{TPC}}(p_\perp, \eta, \mathrm{fpz})$. For the $p_\perp$ spectra, this correction is looked-up and applied track-by-track by weighting each track by the inverse of its reconstruction efficiency. The applied correction, weighted by the actual data distribution of $p_\perp$, η, and fpz is shown in Figure 3.17(d).

Figure 3.17 shows the efficiency values for tracks in the simulated p+p events. The efficiencies are projected along the three axes to illustrate the dependence on each variable. What is shown is the actual applied efficiency: ratio of the number of tracks reconstructed in the TPC that match to the beamline and fall within the acceptance of the Central Trigger Barrel (CTB) to the simulated track distribution when the track is reconstructed. The applied correction is smoothed along all three variables to reduce fluctuations due to limited statistics. The simulations have limited statistics in the $p_\perp$ = 2-3 GeV/c because of computing resources constraints.

First Radial Point in Z Correction

In addition to the above tracking efficiencies, an extra efficiency must be used to take into account when the track's reconstruction fails, because these tracks do not have

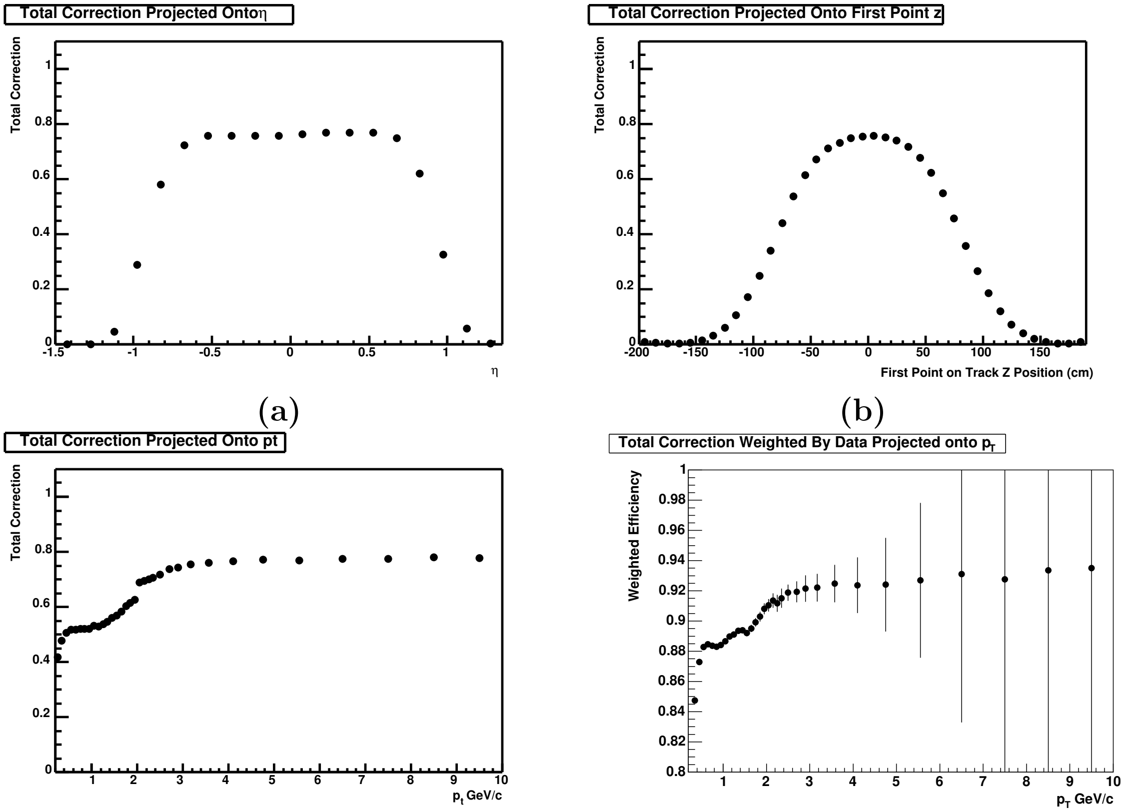

(a) (b)

(c) (d)

Figure 3.17: Proton+proton tracking efficiencies. (a) Efficiency projected along η (b) Efficiency projected along fpz (c) Efficiency projected along $p_\perp$ (d) Efficiency correction weighted by data projected along $p_\perp$. Error bars in a,b,c are smaller than the points. Error bars in d are dominated by the statistics of the data.

a first radial point reconstructed in the TPC. From the simulations this value can be determined and plotted versus $p_\perp$ and η. There is little dependence on η, therefore this correction is applied only as a function of $p_\perp$ and is shown in Figure 3.18(a). This efficiency is then smoothed by fitting to the functional form:

$$\epsilon_{\text{fpz}} = \text{Saturation} \times (1 - \text{AmplitudeExp}) \times e^{-p_\perp/\tau}, \tag{3.2}$$

where Saturation gives the asymptotic plateau level and both AmplitudeExp and τ characterize the curvature. As one can see, this function fits the data and saturates at 98% which is approximately the inactive space between the TPC sectors. This correction is then applied to the $p_\perp$ spectrum.

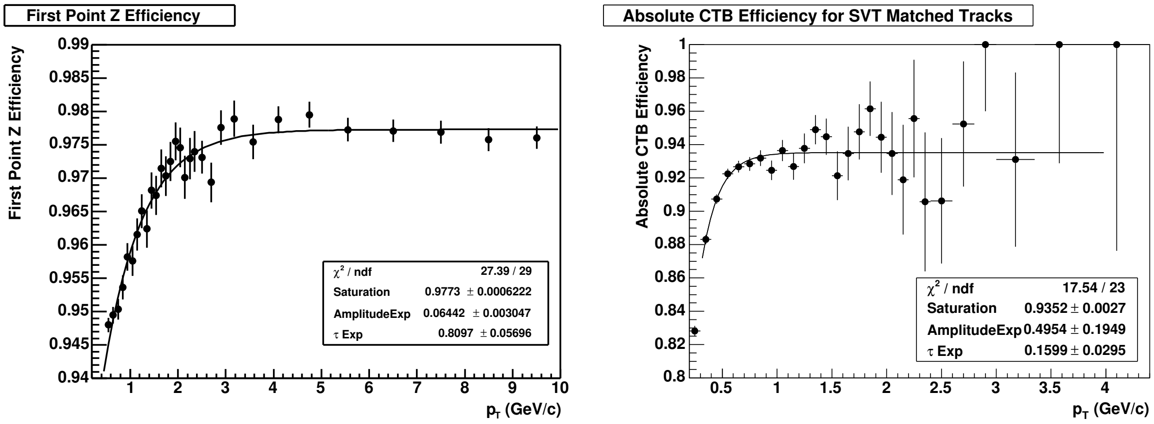

(a) **(b)**

Figure 3.18: (a) Efficiency of reconstructing first radial point in z. The larger error bars from $p_\perp$ = 2-3 GeV/c are due to limited statistics. (b) Absolute Central Trigger Barrel (CTB) Efficiency. The large uncertainty at high-$p_\perp$ is due to the low statistics of available SVT data.

CTB Efficiency and Contamination

The final tracking correction to be applied is the absolute efficiency of the Central Trigger Barrel (CTB) . The above corrections only require that the track passes within the acceptance of the CTB. Because the CTB previously was used only as a trigger detector, the simulations are not as precise as necessary to use the CTB as a tracking detector. Another way, besides simulations, is needed to evaluate the absolute CTB efficiency ($\epsilon_{\rm CTB}$). In Section 3.2.1 the relative CTB efficiency was discussed, but not the absolute efficiency. To evaluate this efficiency, one needs a method independent from the CTB to determine if tracks came from the current trigger and thus are not from pileup. The SVT, as discussed in Section 2.2.2, fortunately provides this cross-check as it has a much faster drift time than the TPC. Tracks that match both the SVT and TPC are treated as the input distribution. This is not sensitive to the SVT absolute efficiency because the TPC to SVT association has occurred already. The reconstructed track distribution is the SVT+TPC tracks that also match to hit CTB slats that are in time with the trigger. This provides the absolute CTB efficiency ($\epsilon_{\rm CTB}$) and is shown in Figure 3.18(b). Just as with the first radial point correction, the function is plotted versus $p_\perp$ and fit to the functional form of Equation 3.2 to smooth out any fluctuations. Because the SVT was not fully commissioned in the p+p run and has a very limited acceptance, it cannot be used as the primary method of pileup rejection. Moreover, only half of the reconstructed data contained usable SVT data. Nonetheless, significant statistics were accumulated to provide a reliable ϵ_{CTB}.

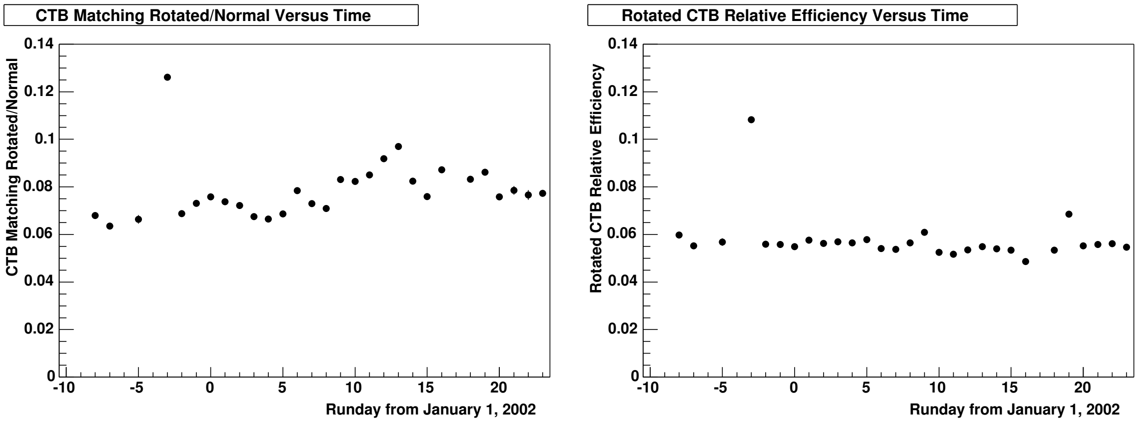

(a) **(b)**

Figure 3.19: (a) CTB matching in rotated events to normal events versus time. (b) CTB matching efficiency for rotated events versus time. The runs that contribute to the abnormally high value on Day -3 have been removed from the final event sample.

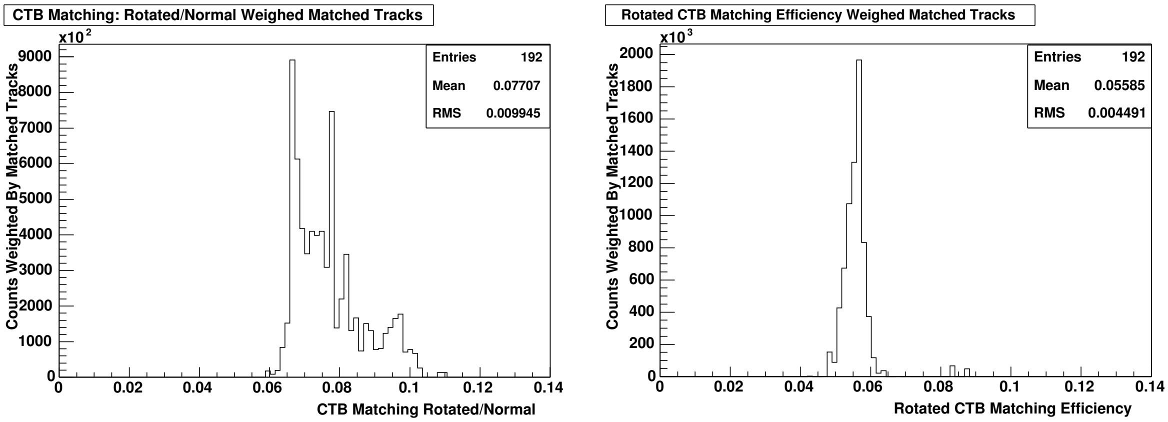

(a) **(b)**

Figure 3.20: (a) CTB matching in rotated events to normal events weighted by the number of tracks in each event. (b) CTB matching efficiency for rotated events weighted by the number of tracks in each event.

Not only does the efficiency of the CTB need to be accounted for, but so does the contamination of the CTB. There is a small chance that two or more tracks in an event project to the same hit CTB slat. Therefore, one of these tracks may not have come from the triggered event. This extra track is contamination and should not be in the spectrum. One can remove any true correlations between the TPC tracks and CTB hits by rotating the assumed CTB slat positions by 90° in azimuth. The ratio of tracks that match the rotated CTB to the tracks that match the normal CTB measures the mismatching of the CTB plus mean occupancy of the CTB. This is shown in Figure 3.19(a). To find the mean occupancy of the CTB, one computes the matching efficiency just as in Figure 3.5(b), but using tracks that match the rotated CTB. This is shown in Figure 3.19(b). Therefore, the CTB mismatching rate is the difference between Figure 3.19(a) and Figure 3.19(b). Because both quantities change with time, one takes difference of the mean of these values weighted by number of matched tracks in each time bin as shown in Figure 3.20 to get the final correction. The difference between the means is $\sim$2% with a systematic error of the same magnitude. Therefore, one multiplies the entire $p_\perp$ spectrum by 0.98 ± 0.02 to account for the CTB mismatching. It is unfortunate that the error on the correction is the same magnitude as the correction itself.

3.5.3 Corrections Due To Weak Decays

This analysis seeks to study primary tracks that are generated in the collision, not decays of these tracks. The daughters of the decays sometimes pass the beamline requirement, as discussed in Section 3.4, and are accepted into the spectrum. In order to correct for this, one uses simulations to quantify how much of the accepted spectrum are, in actuality, products of decays. The simulation framework used for the decay corrections is identical to that used for the determination of the vertex efficiency discussed in Section 3.3. The ratio of accepted HIJING tracks that are products of decays to all accepted HIJING tracks is the decay contribution. This is parameterized versus $p_\perp$ and removed from the final $p_\perp$ spectrum. Figure 3.21 shows this ratio for different parent particles, whose daughters pass the analysis cuts. In the low $p_\perp$ range, the largest contribution to this background are the weak decays of κ_0^{short} mesons. Also in this $p_\perp$ range, γ rays from the decays of π^0 and other mesons, tend to produce $e^\pm$ pairs that are reconstructed in the detector. In the mid-$p_\perp$ range, we also see the weak decays of Λ baryons contributing. After 4.5 GeV/c, the background contribution is taken as a constant at the 4.5 GeV/c level.

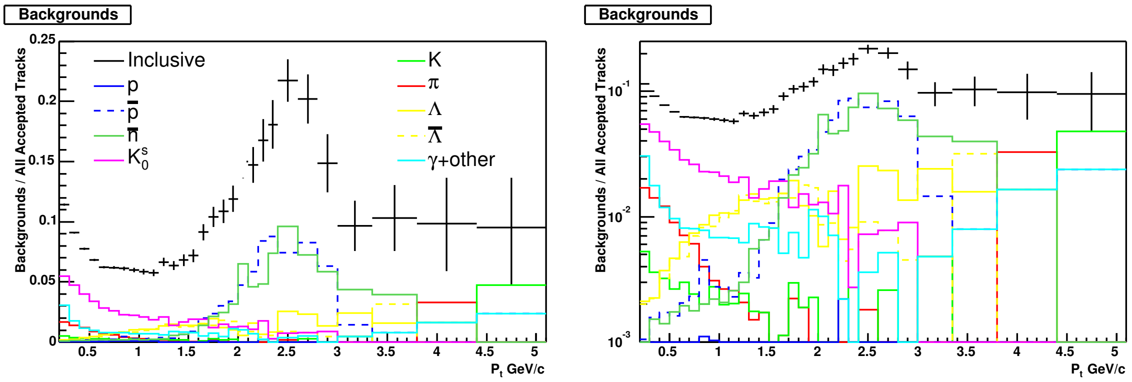

(a) **(b)**

Figure 3.21: Decay background contribution to spectrum (a) linear scale (b) semi-log scale. The legend is common to both figures.

The most striking contribution is the $\bar{p}$ (anti-proton) and $\bar{n}$ (anti-neutron) contribution at $p_\perp \approx 2.5\pm0.5$ GeV/c. This is due to these particles annihilating in the Beryllium beam pipe, producing particles with an extra ~2 GeV/c of energy due to the annihilation. The raw data does not show a bump due to this process. The HIJING production of $\bar{p}$, as well as the other particles, agrees with values obtained by preliminary p+p STAR analyses [33, 34, 35]. Therefore, this anomaly is not due to HIJING over-predicting the yields. It seems that the GEANT package which accounts for particle decays, has a feature where the decays of $\bar{p}$ and $\bar{n}$ in the beam pipe produce a large shower of particles that do not conserve energy and momentum. As shown in Figure 4.4(a), this feature causes maximally a 15% effect in this analysis and only in this limited $p_\perp$ range. Since this correction does not affect the high $p_\perp$ spectrum it is used but a larger systematic error bar is assigned to the affected $p_\perp$ range. As an alternative, one could smoothly interpolate between the data points outside this $p_\perp$ range to get an accurate description of the data between $p_\perp$ = 2.0

and 3.0 GeV/c.

3.5.4 Momentum Resolution Correction

The final $p_\perp$-dependent tracking correction is due to momentum resolution. As discussed in Appendix B, software calculates momentum by reconstructing a track's position and fitting the curvature to a helix model. Therefore, the real momentum and the reconstructed momentum can be different. Even if the momentum resolution is constant in $p_\perp$, this effect softens the spectra by adding more tracks at high $p_\perp$. Although a track has an equal probability of being reconstructed at a higher or a lower $p_\perp$, there are more tracks at low $p_\perp$ available to be shifted to higher $p_\perp$ than the opposite. Also, the meanZ method does not refit the track to the vertex position. This refit, as described in References [19, 28, 36], tends to improve the resolution because the vertex position can better constrain the momentum due to its large lever arm to the outer points. To obtain the correct spectral shape at high $p_\perp$ this correction is crucial.

The simplest measure of momentum resolution is to look at the fractional $p_\perp$ difference defined as

$$\frac{\delta p_\perp}{p_\perp} = \frac{p_{\perp real} - p_{\perp reconstructed}}{p_{\perp real}}, \tag{3.3}$$

where $p_{\perp real}$ is the real (input) momentum and $p_{\perp reconstructed}$ is the momentum reconstructed by the tracking software. This quantity is plotted in Figure 3.22 for a few different $p_\perp$ ranges. The dashed red lines are Gaussian fits to the distribution. The σ, or fractional momentum resolution, for the .5, 2.25, and 9.25 GeV/c $p_\perp$ bins are 1.9 ± 0.1%, 2.7± 0.1%, 7.1± 0.1%, leading to a momentum resolution 9.5±0.1, 61±0.6, and 657±6.6 MeV/c respectively. The resolution (both the RMS and the gaussian σ) increases as $p_\perp$ increases. High $p_\perp$ tracks appear almost as straight lines in the 0.5 Tesla magnetic field of STAR, therefore one expects a larger error at high $p_\perp$.

Notice, the Gaussian fits do not describe the data very well. The distributions are skewed towards higher reconstructed $p_\perp$. This occurs because the software does not fit $p_\perp$, but rather the curvature defined as

$$k \equiv 1/p_\perp. \tag{3.4}$$

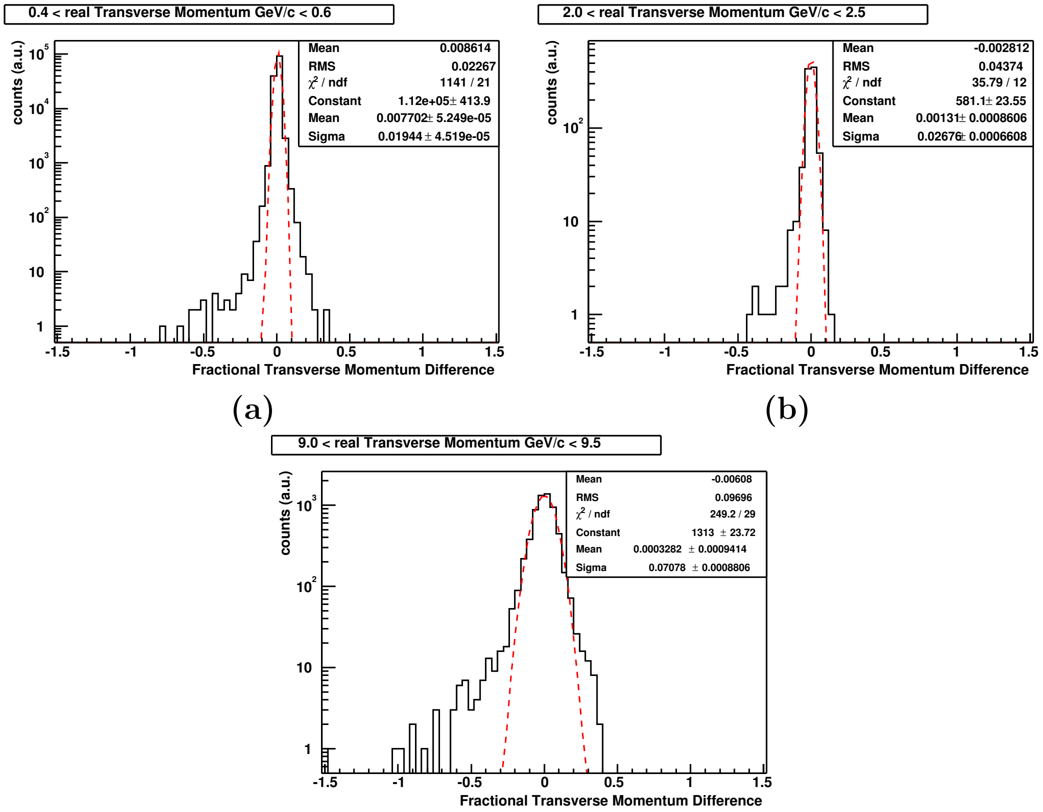

(a) **(b)** **(c)**

Figure 3.22: Fractional $p_\perp$ difference in various $p_\perp$ ranges. (a) $0.4 < p_\perp < 0.6$, (b) $2.0 < p_\perp < 2.5$, (b) $9.0 < p_\perp < 9.5$.

Therefore, the fractional curvature difference

$$\frac{\delta k}{k} = \frac{k_{real} \; - \; k_{reconstructed}}{k_{real}} \tag{3.5}$$

should be Gaussian. Figure 3.23 shows fractional curvature difference for the same data as in Figure 3.22. Although the Gaussian fits are not perfect, one notices the distributions are more symmetric.

The curvature resolution can be parameterized versus $p_\perp$ and is plotted in Figure 3.24(a). The curvature resolution versus $p_\perp$ can be fit to a linear function

$$\frac{\delta k}{k}(p_\perp) = a + b \cdot p_\perp . \tag{3.6}$$

The fit between 1.5 GeV/c $< p_\perp <$ 7 GeV/c yields $\frac{\delta k}{k}(p_\perp) = 0.018 + 0.0063\, p_\perp/\mathrm{GeV/c}$.

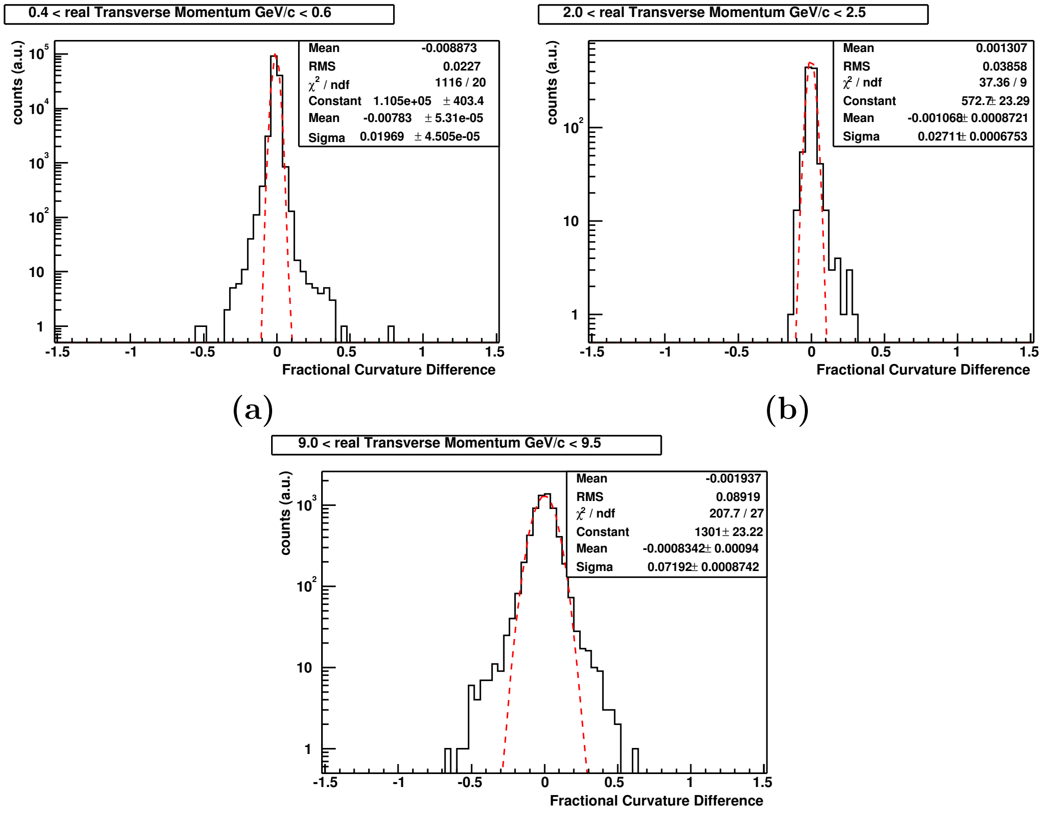

(a) **(b)**

(c)

Figure 3.23: Fractional curvature difference in various $p_\perp$ ranges.

In order to transform the fractional curvature resolution to a correction, the method of convolution is used. Defining

$$x \equiv p_{\perp real} \quad \text{and} \quad y \equiv p_{\perp reconstructed} \quad \text{and} \quad \sigma(x) \equiv \delta k, \tag{3.7}$$

the real spectrum, $f(x)$, is convoluted with the Gaussian curvature resolution keeping x fixed,

$$\frac{1}{2\pi\sigma(x)} \exp(-\frac{(1/x - 1/y)^2}{2\sigma(x)}). \tag{3.8}$$

Now, we want to convolute these functions over y, so the substitution

$$z = 1/y \quad and \quad dz = -1/y^2 \tag{3.9}$$

is made. After these substitutions, the measured yield for $p_{\perp low} < p_\perp < p_{\perp high}$ is given

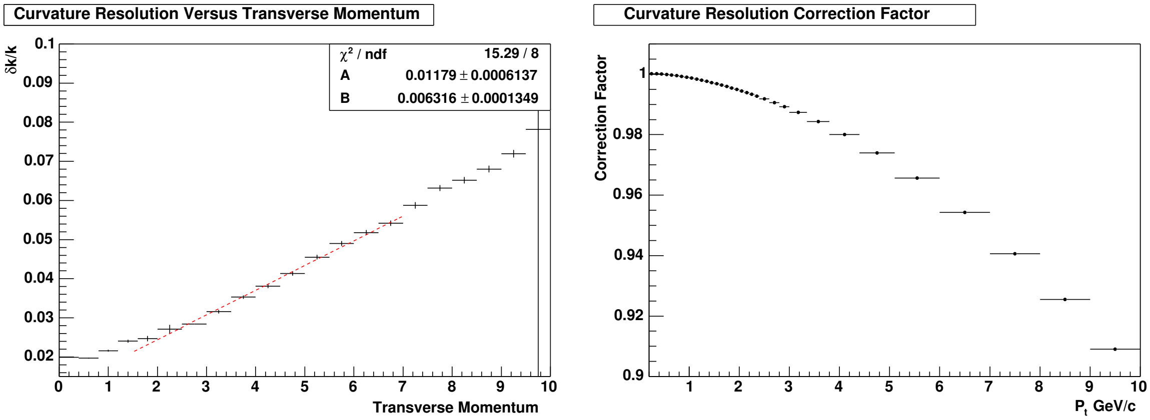

(a) **(b)**

Figure 3.24: (a) Curvature resolution versus $p_\perp$ and the (b) curvature resolution correction.

by

$$N_{measured}(p_\perp) = \int_{p_{\perp low}}^{p_{\perp high}} dy \int_0^\infty dx \frac{1}{\sqrt{2\pi}\cdot(ay^2/x + by^2)} \exp(-\frac{(x-y)^2}{2(ay+bxy)^2}). \quad (3.10)$$

The real yield in this $p_\perp$window is given by

$$N_{real}(p_\perp) = \int_{p_{\perp low}}^{p_{\perp high}} f(x)dx. \quad (3.11)$$

The multiplicative correction factor applied to the spectra is

$$Correction(p_\perp) = \frac{N_{real}(p_\perp)}{N_{measured}(p_\perp)} \quad (3.12)$$

An iterative approach is needed because $f(x)$ is not known. Therefore, the measured spectrum is used first, then the corrected spectrum from the first pass is used as the new $f(x)$. This procedure converges by the third iteration and is shown in Figure 3.24(b).

3.5.5 Summary of Tracking Corrections

A summary of the individual tracking corrections is shown in Table 3.3 along with the approximate magnitude of each correction. Figure 3.25 shows the sum of the corrections applied versus $p_\perp$. One may notice the large dip in the correction factor at 2.5 GeV/c. This is due solely to anti-nucleon annihilation feature in the background correction discussed in Section 3.5.3.

The magnitude of the total correction applied is less than 20% over the majority of the $p_\perp$ range. At high $p_\perp$ the corrections are on the order of 5%. The integrated correction factor defined as:

$$\text{Integrated Correction Factor} = \frac{\sum N(p_\perp)\ C_{TOTAL}(p_\perp)}{\sum N(p_\perp)} \tag{3.13}$$

where N($p_\perp$) is the number of measured counts at the given $p_\perp$ bin and $C_{TOTAL}(p_\perp)$ is the $p_\perp$ correction factor displayed in Figure 3.25, is 1.27 ± 0.02 for $p_\perp > 0.2$ GeV/c. The value is dominated by the low $p_\perp$ region. This value will be needed to correct the multiplicity distribution in Section 3.7.

Correction Applied	Correction Factor
TPC Acceptance Correction	∼1/0.88 to 1/.92
First Point Z Correction	∼1/0.97
CTB Acceptance Correction	∼1/.93
CTB Mismatch Correction	0.98 ± 0.02
Decay Track Correction	∼1/0.9
Momentum Resolution Correction	∼ 1-0.9

Table 3.3: Summary of tracking correction factors.

3.6 Absolute Normalization of the Cross Section

This is the first analysis at $\sqrt{s} = 200$ GeV that absolutely normalizes the p+p → $\text{h}^\pm$ + X spectra to the measured cross section at this energy. Previous analyses of p+p̄→ $\text{h}^\pm$ + X from the UA1 and UA5 Collaborations interpolated or measured the difference in the cross section from measurements at lower and higher energies [8, 37]. This section will detail the measurement and the corrections needed to obtain the absolutely normalized non-singly diffractive (NSD) cross section.

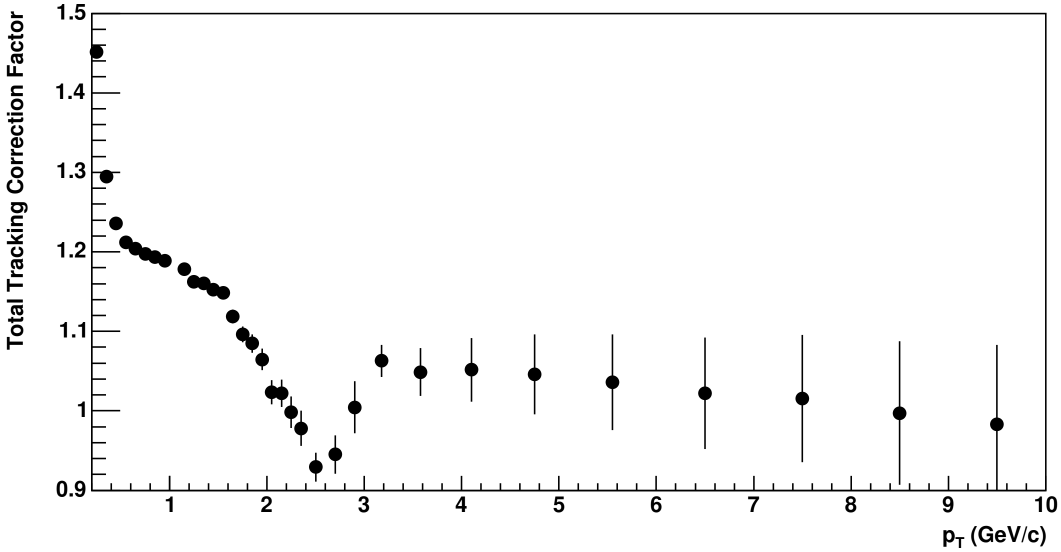

Figure 3.25: Total tracking correction factor versus $p_\perp$. Details are discussed in the text.

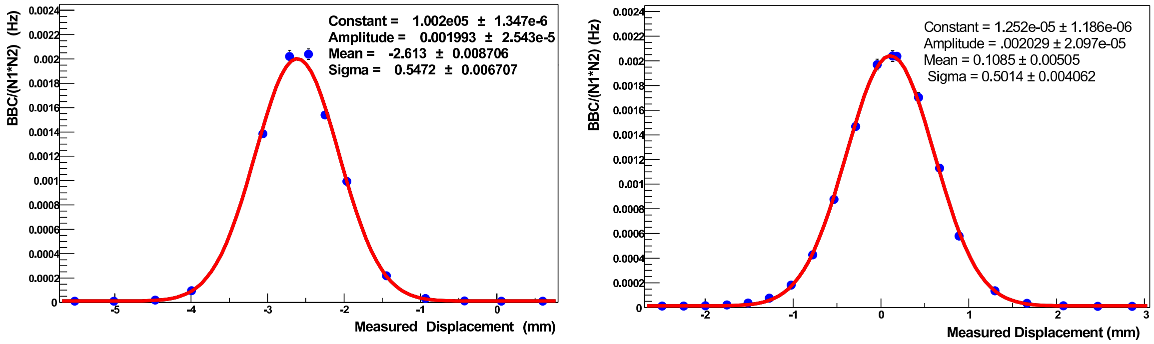

(a) **(b)**

Figure 3.26: Vernier scan beam displacement profiles for the (a) horizontal and (b) vertical directions.

3.6.1 Vernier Scan and Luminosity

To obtain the cross section of p+p → $h^\pm$ + X, one must first determine the cross section sensitivity of the trigger detectors. As discussed in Section 2.2.1, the trigger detectors are the BBCs which are two annular scintillators located at high forward and backward rapidity. A technique called a van de Meer or Vernier Scan is used to determine this cross section [38]. In this method, the two counter rotating beams are swept across each other and the coincidence rate of the BBCs as a function of the beam displacement is measured. Figure 3.26 shows one measurement of this for the horizontal (x) and vertical (y) direction. The vertical axis is normalized by the total number of ions in each beam multiplied together. This is fit to a Gaussian to extract the effective beam width in the ith (x or y) direction

$$\sigma_{Vi} = \sqrt{\sigma_{i1}^2 + \sigma_{i2}^2} \tag{3.14}$$

which is the convolution of the two individual beam widths. The maximum of this curve, R$_{max}$, is the maximum BBC coincidence rate obtainable divided by the number of ions in each beam multiplied together.

As discussed in Section 3.2.1, the BBC coincidence rate is the luminosity of the beams times the BBC cross section. The luminosity also is given by

$$\mathcal{L} = \frac{k_b\ f_{rev}\ N_1\ N_2}{2\pi\ \sigma_{Vx}\ \sigma_{Vy}} \tag{3.15}$$

where k_b is the number of filled bunches in each beam (56), N_i is the number of ions in each bunch ($\sim 100 \times 10^9$) and f_{rev} is the frequency of revolution (78 kHz). It can be derived that

$$\sigma_{BBC} = 2\pi\ R_{max}\ \sigma_{Vx}\ \sigma_{Vy}\ k_b\ / f_{rev}. \tag{3.16}$$

From this equation and four of the above beam profile measurements spaced over time, it was determined that the measured BBC cross section in STAR, $\sigma_{BBC} = 26.1 \pm 0.2 \pm 1.0 \pm 0.8$ mbarn [38].

The absolute determination of the luminosity cannot be determined every run because a van de Meer scan cannot be performed during a run. Once σ_{BBC} is known, however, the luminosity can be computed as

$$\mathcal{L} = \frac{\text{BBC Coincidence Rate}}{\sigma_{BBC}} \tag{3.17}$$

Figure 3.27(a) shows the BBC coincidence rate on the left axis, and the resulting luminosity on the right axis, versus time. The luminosity is averaged over the time when the data of this analysis was taken. The quoted average luminosity of the beams is 1.2×10^{30} cm^{-2} s^{-1} [39]. However this value is taken from the peak luminosity at

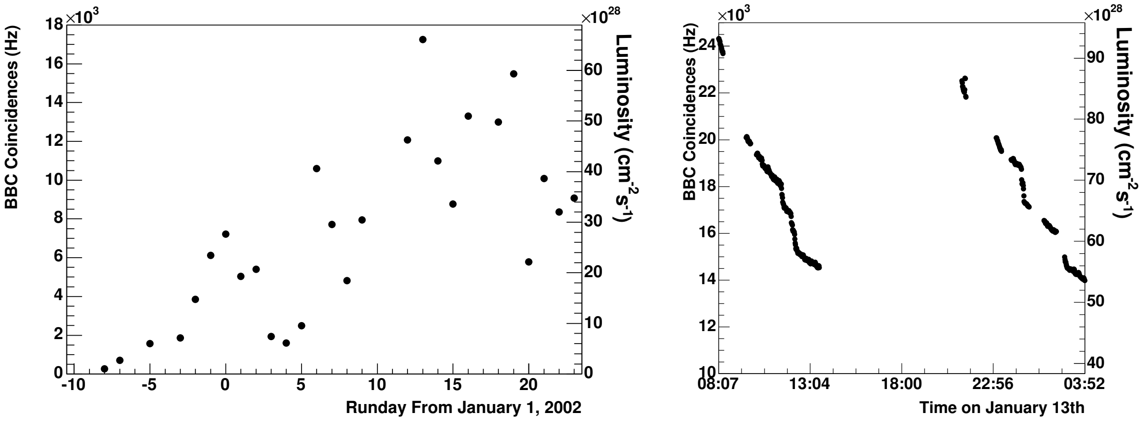

(a) (b)

Figure 3.27: (a) Average daily luminosity versus time, averaged over the entire active run day. (b) Luminosity versus time for Day 13 of the run.

the beginning of the store, not when data is actually being recorded. An example of the luminosity decay is shown in Figure 3.27(b). The gaps are due to down time of the detector. During the large gap in the middle of the figure, the beams were re-filled.

3.6.2 BBC Efficiency

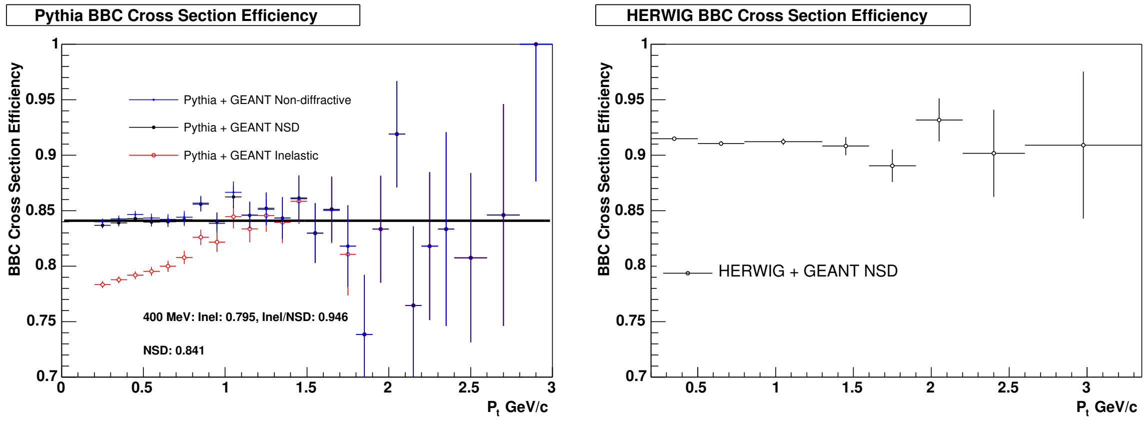

(a) (b)

Figure 3.28: BBC efficiency from (a) Pythia and (b) HERWIG.

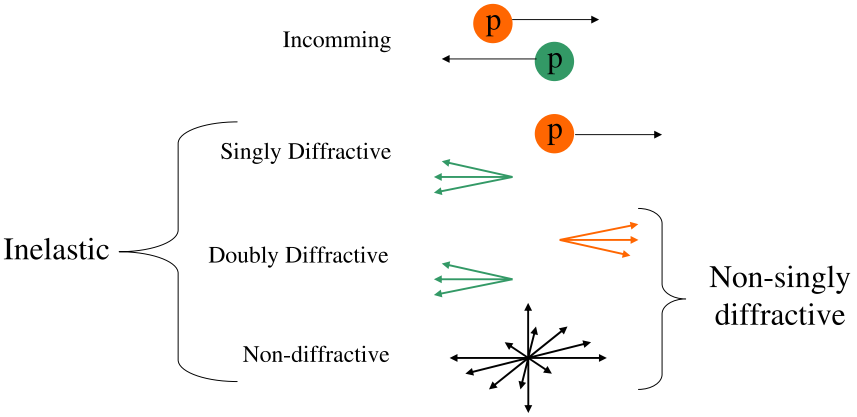

Figure 3.29: Illustration of p+p cross sections.

The efficiency of the BBC must be found in order to determine the cross section. Due to the dual-arm configuration, the trigger is sensitive to the non-singly diffractive (NSD) cross section which is the sum of the non-diffractive and doubly diffractive cross section. The inelastic cross section is the sum of the NSD and singly diffractive cross section as illustrated in Figure 3.29. Simulations from both the Pythia [40] and the HERWIG [41] event generators were passed through GEANT and a full simulation of the STAR geometry including a BBC response simulator [42]. The efficiency of the BBC, ϵ_{BBC}, is defined as the ratio of the simulated $p_\perp$ spectrum ($|\eta| < 0.5$) for events that triggered a BBC coincidence to the simulated $p_\perp$ spectrum for all events. The results for Pythia and HERWIG are shown in Figure 3.28 and are broken down by the collision type: NSD, non-diffractive and inelastic. In the Pythia simulated NSD events, the BBC has negligible bias versus $p_\perp$ and $\epsilon_{BBC} = 84.1\%$. From the HERWIG simulations of only NSD events, a slightly higher value of $\epsilon_{BBC} = 91.3\%$ is obtained. The final correction to the differential cross section is $\epsilon_{BBC}^{d\sigma/dp_\perp} = 0.877 \pm 0.8\%$. This correction is due to the fact that 17.5% of the events do not trigger the BBC; therefore accounting for the HERWIG and Pythia differences, the total NSD cross section is adjusted to $\epsilon_{BBC}^{NSD} = 0.860 \pm 0.8\%$.

From Figure 3.28(a), one can see the inelastic events do have some $p_\perp$ bias. Therefore, the histogram is fit by a straight line between 400 MeV/c and 1.3 MeV/c resulting in a $p_\perp$ dependent correction the form $\epsilon_{\sigma_{inel}} = 0.922 + 0.06\ p_\perp$which is only applied between 400 and 1.3 GeV/c. This correction only is applied to the inelastic cross section as it is not applicable to the NSD cross section. The correction also adds an additional 3% point-to-point error as the fraction of the total inelastic cross section due to singly-diffractive events is unknown to a factor of two. Other Pythia simulations also determine that 2.5 ± 1% of the BBC triggers are due to singly diffractive events that do not produce tracks at mid-rapidity. This NSD contamination must be removed from the final NSD spectra.

3.6.3 Trigger Backgrounds

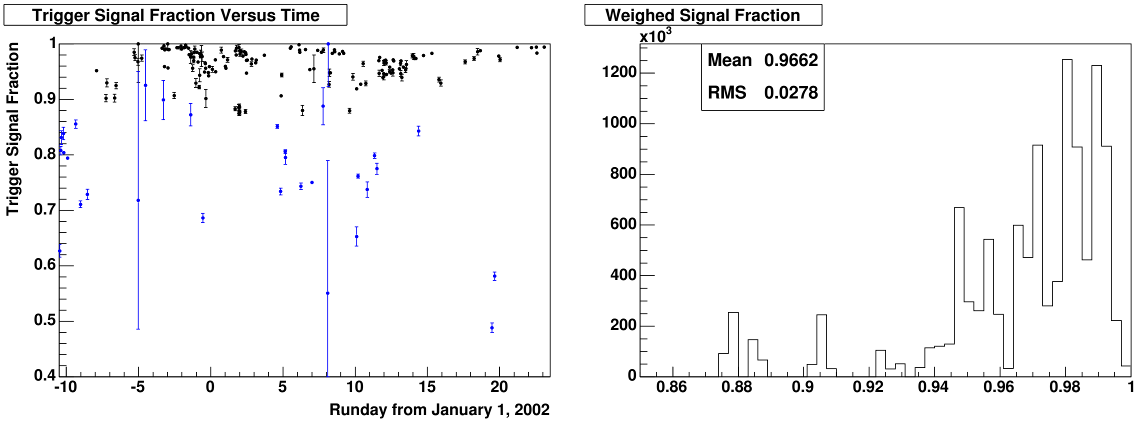

(a) **(b)**

Figure 3.30: (a) Trigger backgrounds versus time. Accepted runs are shown in black, rejected runs are shown in blue. (b) 1 dimensional projection of accepted runs weighted by the number of triggers.

In addition to the trigger efficiencies explained above, the BBC trigger sometimes erroneously fires due to beam gas backgrounds. This background rate can be quantified experimentally with the abortgap events discussed in Section 2.1.2. There should not be any triggers that occur in the abortgaps because it is impossible to have a bunch-bunch interaction when one of the bunches is not filled. By counting the number of triggers that occur in the abortgap versus the total number of triggers, one can determine a false triggering rate. The total number of events that occur in the 10 abortgap bunches is defined as A and the total number of events in all

60 bunches is defined as T. Since each abortgap bunch crossing has one of the two beams filled, then the non-abortgap bunches must have twice the contamination of the abortgap bunches if one assumes that the background is distributed uniformly. Therefore, the total background present in all 50 signal bunches is 50×2×A/10. The efficiency, or signal over total, is 1 - 11 A/T after subtracting the contribution from the two abortgaps. Figure 3.30(a) shows this efficiency over the entire run. All runs with an efficiency minus 2 sigma of less than 0.85 were rejected from the data sample because the background levels were too high. The rejected runs are shown in blue and the accepted runs in black. The weighted average of efficiency for accepted runs is determined to be 0.97 ± 0.02 as shown in Figure 3.30(b). This is not needed to correct the NSD cross section as backgrounds are accounted for in the Vernier Scan.

3.6.4 Lost MeanZ Events

The cross section also must account for lost events. Although the spectra only contains the 5×10^6 events with tracks within $|\eta| < 0.5$ that produce a meanZ within ±75 cm, it must be normalized to all events that occur within ±75 cm, not just events that contain these tracks. This cut was chosen to maximize the event acceptance and stability of the correction. In principle this is a simple correction to find: place a cut at 75 cm and see the fraction of events taken within that cut. This gives the percentage of BBC triggers that should produce an event within ±75 cm. However, one must avoid issues such as vertex efficiency and acceptance effects which can be multiplicity dependent. In order to avoid vertex efficiency issues, only high multiplicity events ($dN/d\eta$ = 10-15) are used for this study. This requires the assumption that the shape of the actual longitudinal vertex distribution is the same for both low and high multiplicity events. The assumption is defendable because the vertex distribution should be only a function of the initial beam parameters and not the final state of the collision.

Acceptance at the edges of the TPC also affect the large longitudinal reconstructed vertex tails as shown in Figure 3.2(a). To account for this, a method is devised to obtain the true input vertex distribution that produced the data. First, for high multiplicity events, one constructs the ratio of the reconstructed longitudinal vertex probability distribution from the real data to the reconstructed longitudinal vertex probability distribution from HIJING simulations that was produced from a flat input distribution that covered the entire TPC acceptance. This ratio, shown in Figure 3.31(a), is the observed longitudinal vertex distribution corrected for edge effects for dN/dη = 10-15 where the vertex efficiency is approximately unity.

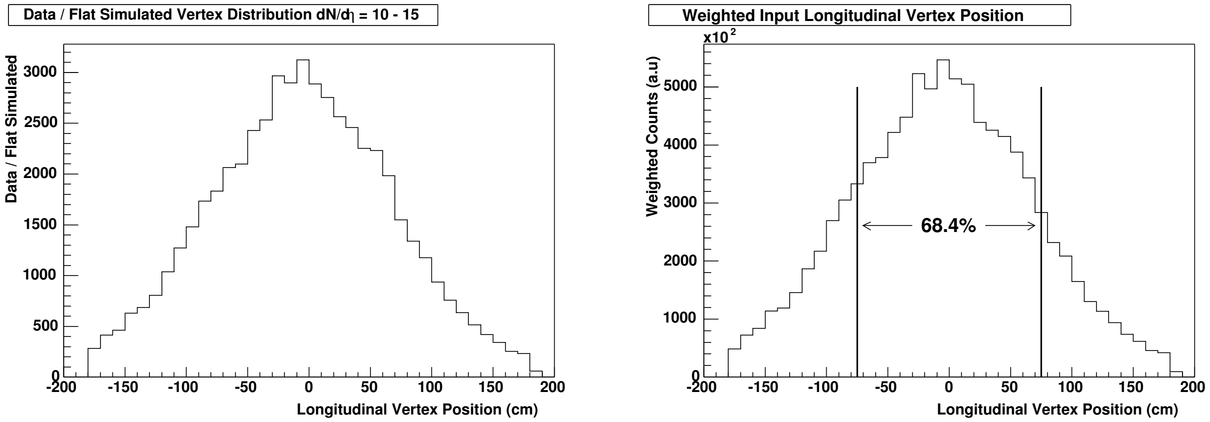

(a) (b)

Figure 3.31: (a) Ratio of data to simulated flat longitudinal vertex distribution for high multiplicity events (dN/dη = 10-15). (b) Input longitudinal vertex distribution for all multiplicities weighted to match the data.

To obtain the input vertex distribution for all multiplicities, one weights the flat HIJING simulation by this ratio for all multiplicities. This is shown in Figure 3.31(b). The ratio of simulated events that fall within the cut of ±75 cm to the total distribution represents the fraction of BBC triggers that lie within ±75 cm which is shown to be 68.4%. This ratio, defined as f$_{vert}$, times the number of BBC triggers represents that true number of events that occurred within this range. The spectra should be normalized to this true number of events instead of to the number of events that have tracks within $|\eta| < 0.5$.

As a cross check, one can also look at the experimental measure of f$_{vert}$ by studying the ratio of number of events within ±75 cm from the output of the standard (ppLMV) and the alternate (meanZ) vertex finder. These quantities are plotted versus the two measures of multiplicity in Figure 3.32(a,b,c). The quantities are also plotted for both

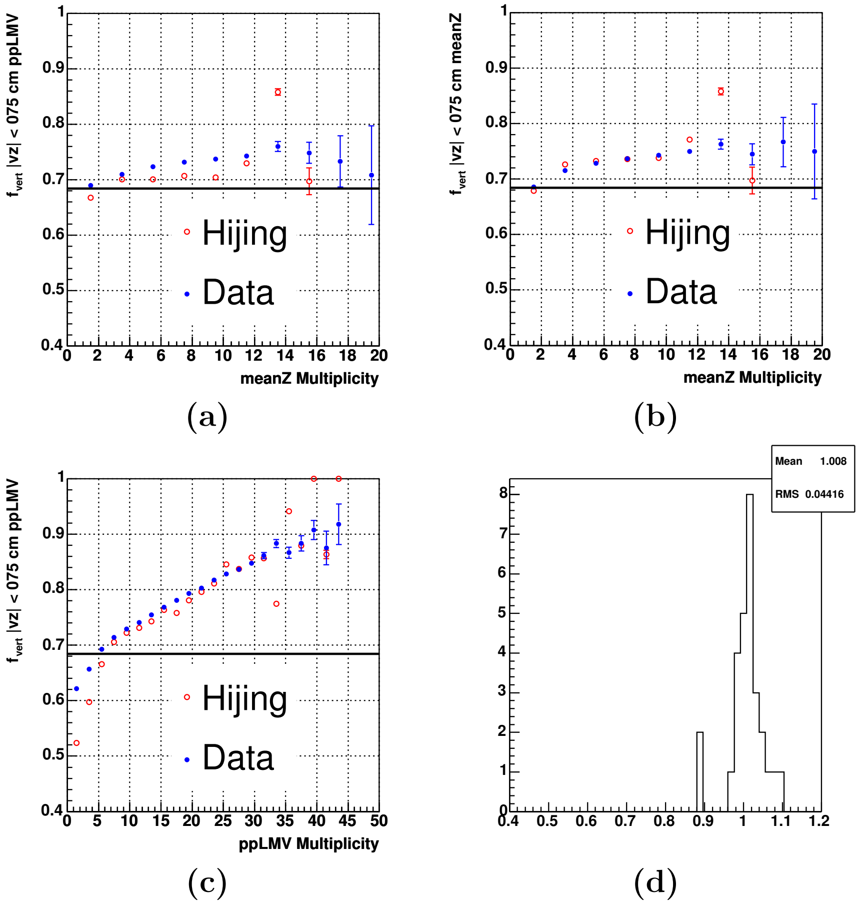

Figure 3.32: (a) f$_{vert}$ from meanZ versus meanZ multiplicity (a) f$_{vert}$ from ppLMV versus meanZ multiplicity (c) f$_{vert}$ from ppLMV versus ppLMV multiplicity. (d) Ratio of data over HIJING from (a,b,c).

real data and re-weighted HIJING simulations. Notice the ratios are approximately flat versus multiplicity, except versus the standard vertex finder multiplicity, but this multiplicity is not a valid measure because of the effects discussed in Section 3.1. However, the simulations seem to underestimate the data by about 1% on average of the three plots as shown in 3.32(d). Therefore, the f$_{vert}$ is boosted up by 1% and the final f$_{vert}$ value used is .69 ± 0.035.

3.6.5 Summary of Absolute Cross Section Measurement and Corrections

Now that the trigger cross section has been measured and the various corrections have been applied, the final value can be reported. The measurements and the corrections for two cross sections are summarized in Table 3.4.

Correction Applied	Non-Singly Diffractive Trigger Cross Section
Measurement From Vernier Scan	26.1 ± 1.9 mb
BBC Acceptance Correction	1/(0.860 ± 0.08)
NSD Contamination	0.975 ± .01 %
Total Value of σ_{NSD}	31.1 ± 3.7 mb

Table 3.4: Summary of σ_{NSD} measurement and corrections.

3.7 Charged Particle Multiplicity Distributions

Another experimental observable is the event multiplicity, which is number of charged particles per event. This section will discuss the efficiency corrections to the multiplicity distributions. The actual distributions will be discussed in Chapter 4. In this analysis the multiplicity distributions are produced by counting the number of tracks within the pseudorapidity range $|\eta| < 0.5$ that pass the meanZ analysis cuts of a CTB and a beamline match as discussed in Section 3.4. However, the analysis must also account for the efficiency of accurately reconstructing said particles. In the $p_\perp$ spectra analysis, the particles are weighted by the inverse of the reconstruction efficiency, but this method does not produce desirable results when studying the multiplicity because of discrete integerization. In p+p collisions, the multiplicities are small enough that one should bin the distribution with single particle widths. If a particle has a reconstruction efficiency less than unity and the standard weighting procedure is used, the particle would always count as two particles. Therefore the distributions will be systematically skewed towords higher multiplicity. Another method of statistically assigning particles to either the higher or lower bin depending on the reconstruction efficiency also produces a non-uniform distribution.

A matrix method based on combinatorics and probability is the most robust solution to this problem. The meanZ method only counts events when a track that matches the analysis cuts is found. Therefore, this method intrinsically cannot determine the contribution in the zero multiplicity bin, e.g. an event occurs but does not produce a track at mid-rapidity. However, from the f_{vert} correction discussed in Section 3.6.4, we know this number to be 69%, this is used as the initial contribution to the zero multiplicity bin.

Next a correction for efficiency must be done. A matrix method is used to model the bin sharing and has the form of:

$$P(m,n;\epsilon_{global}) = C_n^m \times \epsilon_{global} \times (1-\epsilon_{global})^{m-n}, \tag{3.18}$$

where m is the real number of tracks, n is the reconstructed number of tracks, and ϵ_{global} is the total reconstruction efficiency summed over all variables. The first component of ϵ_{global} is found by integrating the total efficiency correction over the entire measured $p_\perp$ spectrum. This is the reciprocal of the integrated correction factor of Section 3.5.5. The second component of ϵ_{global} takes into account the tracks not reconstructed to due the $p_\perp$ cut off of 200 MeV/c from the CTB matching requirement. This contribution is determined by integrating the powerlaw functional form of the spectrum, as described in Appendix C, over this unmeasured region to determine the loss and is found to be 0.286 ± 0.015 %. The error is determined by varying the fit parameters within their uncertainties. Adding the contributions together, ϵ_{global} is determined to be 64.5 ± 1.0 %.

The first term of equation 3.18, C_n^m, accounts for the binomial combinatorics. For example, if there are four real tracks (m=4), and three reconstructed tracks (n=3), then this term accounts for the combinatorics because one does not know which of the four real tracks are lost. The second term is the probability to reconstruct n tracks, and the third term is the probability not to reconstruct the $m-n$ missing tracks. Therefore the array element P(m,n) is the total probability to reconstruct n tracks when there are in fact m real tracks. Since this matrix evolves the real distribution to the reconstructed distribution, if one inverts this matrix it will evolve the reconstructed distribution to the real distribution. The data and comparisons to other experiments data and theoretical models will be presented in the following chapter.

Chapter 4

Results from p+p Collisions

4.1 Proton+Proton Total and Non-Singly Diffractive Cross Section at $\sqrt{s} = 200$ GeV

This is the first analysis to measure the cross section of p+p or p+p̄ at $\sqrt{s} = 200$ GeV. As already stated, all previous published numbers did not measure directly the cross section. The UA5 collaboration at CERN published a phenomenological fit to higher and lower energy data to interpolate the value at $\sqrt{s} = 200$ GeV [8, 43]. The UA1 collaboration at CERN measured the ratio of the cross section between $\sqrt{s} =$ 200 GeV and 546 GeV [37] and used the measured value from $\sqrt{s} = 546$ GeV from the UA4 collaboration at CERN [44]. The fits of the UA5 collaboration also relied heavily on this single UA4 point. Figure 4.1 shows a compilation of cross sections at different $\sqrt{s}$ including the results from this analysis.

Upon inspection of Figure 4.1, one may notice the measured cross section from this analysis is approximately 86% of the value from UA1 and 79% of the value of UA5. As discussed earlier, the UA1 and UA5 points are not completely independent measurements. It is understandable that these measurements are systematically different than the value from this analysis. All values, including the ones from this analysis, depend on models and simulations to extract the efficiency of the detectors as discussed in Section 3.6. Many elements, such as simulations and computing power have improved in the nearly 20 years since the UA4 measurement. Therefore, this analysis is not concerned with the nearly 1 sigma discrepancy in the cross section measurement and considers the STAR result to be the more reliable measurement. Moreover, as will be discussed in the following sections, the roughly 20% difference does not change drastically the physics conclusions. The analysis also measures the

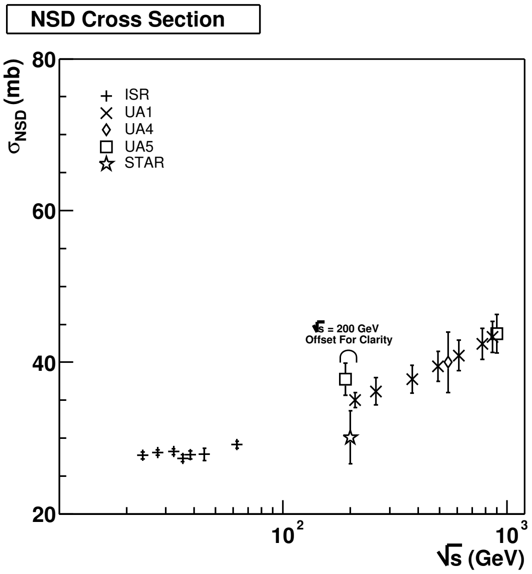

Figure 4.1: Non-singly diffractive cross section versus $\sqrt{s}$. The three points at $\sqrt{s}$= 200 GeV are offset for clarity. STAR points are p+p and all other points are p+p̄.

p+p cross section, where the other experiments above $\sqrt{s}$ = 200 GeV solely run p+p̄ collisions.

4.2 Inclusive Charged Hadron Spectra

The fully corrected inclusive charged hadron $p_\perp$ spectra from p+p collisions at STAR are shown in Figure 4.2. The left vertical axis gives the invariant $p_\perp$ distribution per event. The right vertical axis gives the invariant non-singly diffractive cross section. For legibility, the inelastic cross section is not shown, but can be found by applying the linear correction described in Section 3.6.2. The only published similar measurement at $\sqrt{s}$ = 200 GeV was performed by UA1 [37]. The kinematics of the UA1 experiment are different: it studied p+p̄ collisions in the pseudorapidity range of $|\eta| < 2.5$, while this analysis measures p+p collisions in the pseudorapidity range of $|\eta| < 0.5$. Despite these differences, both spectra are plotted in Figure 4.3(a) for comparison.

Although the spectra look consistent, the semi-log scale of Figure 4.3(a) can be deceiving. One should compare the two spectra on a linear scale bin-by-bin. The

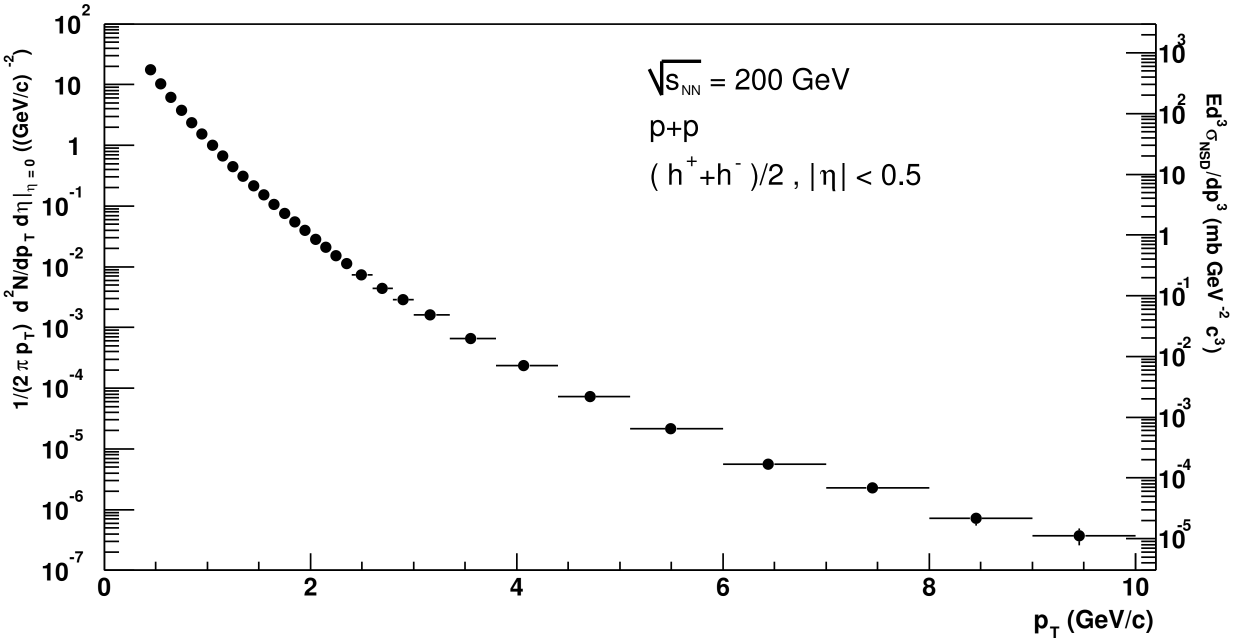

Figure 4.2: p+p inclusive charged hadron $p_\perp$ spectra. The left axis labels the invariant $p_\perp$ distribution. The right axis labels the invariant non-singly diffractive cross section.

UA1 analysis uses different $p_\perp$ bins than the current analysis. This, along with the pseudorapidity acceptance difference, makes an accurate and model free comparison difficult. One can minimize the differences by rebinning the current analysis to match UA1. The rebinned STAR data, divided by the UA1 data bin-by-bin, is shown in the top panel of Figure 4.3(b). The comparison is done only out to $p_\perp = 4$ GeV/c because the UA1 binning is ambiguous past this point. The larger error bars at high $p_\perp$ are dominated by the reported uncertainty from the UA1 data. The small curve in the ratio at low $p_\perp$ is due to the different pseudorapidity acceptances of the two experiments. A correction to the ratio is computed with the Pythia event generator and plotted along with the data. If the spectra are equivalent, the ratio will lie along this correction curve. The ratio seems to track the shape of the curve, but is systematically lower. The normalization value is determined by the differences in the measured cross section as described in Section 4.1. By scaling the normalization of the UA1 data by 79%, the ratio of the two spectra lies along the correction curve as

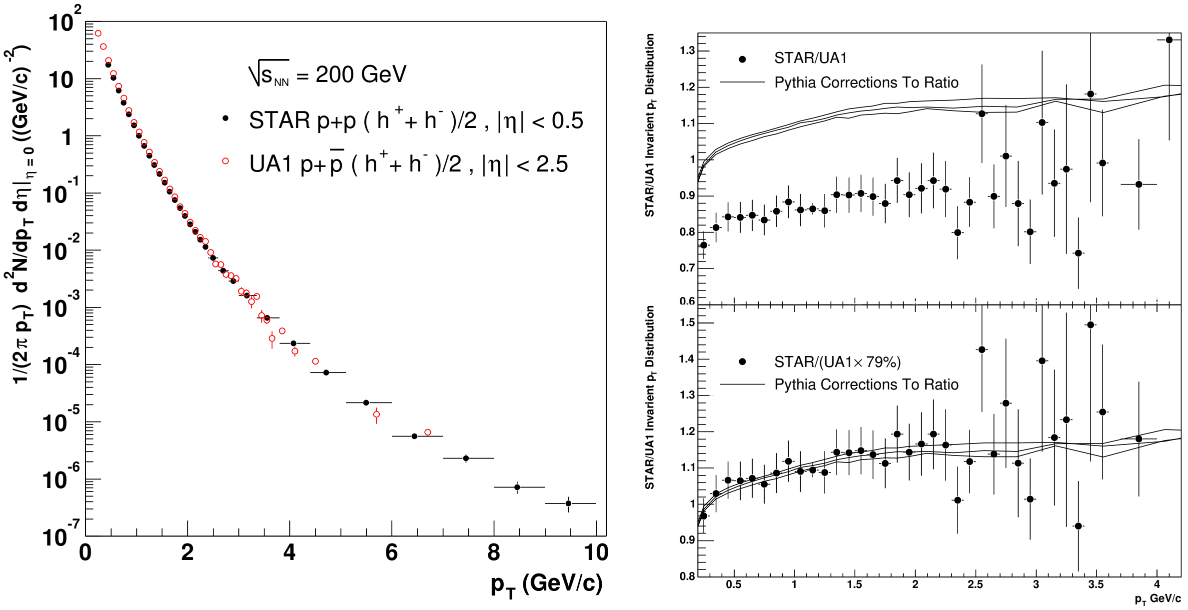

(a) **(b)**

Figure 4.3: (a) STAR p+p and UA1 p+$\bar{\mathrm{p}}$ [37] inclusive charged hadron $p_\perp$ spectra (b) Top: Ratio of STAR data divided by UA1 data. The STAR data has been rebinned to match UA1. The black lines are Pythia corrections to the ratio for the different measured pseudorapidity ranges. Three correction lines are shown, each with different contributions due to higher order effects. Bottom: Same as top panel, but UA1 data is scaled by 79%.

shown in the bottom panel of Figure 4.3(b). This demonstrates that after correcting for the different pseudorapidity acceptances and measured cross sections, the spectra are consistent versus $p_\perp$. The spectra from this analysis reaches over 3 GeV/c farther in $p_\perp$ than the UA1 measurement.

4.2.1 Mean $p_\perp$

The first global observable that can be extracted from the $p_\perp$ spectra is the mean $p_\perp$ ($\langle p_\perp \rangle$) of all the particles that come from the collision. Because the spectra is only measured in the range 0.4 GeV/c $< p_\perp <$ 10 GeV/c, a simple arithmetic mean cannot be used to find the $\langle p_\perp \rangle$. A model of the spectra's generating function must be assumed. This analytic function can then be integrated over all $p_\perp$ to extract the $\langle p_\perp \rangle$. A perturbative-QCD inspired powerlaw function commonly is chosen to represent $p_\perp$ spectra and it has the form

$$g(p_\perp) = A(1 + p_\perp/p_0)^{-n} \tag{4.1}$$

The mean of this function can be found by integration as shown in Equation 4.2.

$$\langle p_\perp \rangle = \frac{\int_0^\infty p_\perp \; g(p_\perp) \; dp_\perp}{\int_0^\infty g(p_\perp) \; dp_\perp} = \frac{2p_0}{n-3} \tag{4.2}$$

Notice the absolute normalization value, A, does not factor into the $\langle p_\perp \rangle$ calculation. The parameters p_0 and n, unfortunately, are correlated highly so a detailed error analysis of $\langle p_\perp \rangle$ from this form of the powerlaw is difficult. To remove the correlation, one can substitute for p_0 in Equation 4.1 in terms of $\langle p_\perp \rangle$ and n as shown in Equation 4.3.

$$g(p_\perp) = A(1 + \frac{2p_\perp}{(n-3)\langle p_\perp \rangle})^{-n} \tag{4.3}$$

Now that the function is written in terms of $\langle p_\perp \rangle$, this variable can be fit directly with a standard error analysis. The binning and fitting techniques of Appendix C are used to obtain the most accurate fit. This fit is done in different $p_\perp$ ranges to obtain the systematic error as summarized in Table 4.1. The final value is taken to be $\langle p_\perp \rangle$ = 0.388 ± 0.008 (stat) $^{+.001}_{-.008}$ (sys) GeV/c.

Fit	Minimum $p_\perp$ (GeV/c)	Maximum $p_\perp$ (GeV/c)	$\langle p_\perp \rangle$ (GeV/c)	χ^2 / ndf
A	0.4	2	0.389 ± 0.015	0.95 / 13
B	0.4	5	0.388 ± 0.008	3.09 / 24
C	0.4	10	0.380 ± 0.007	10.31 / 29

Table 4.1: $\langle p_\perp \rangle$ Fitting systematics showing extracted $\langle p_\perp \rangle$ from different fit ranges.

The extracted $\langle p_\perp \rangle$ vary with the fit range because the powerlaw model breaks down at high $p_\perp$. To illustrate this fact, the fractional residuals versus $p_\perp$ are shown for fits A and C in Figure 4.4(a). In both fits, the residuals grow after $p_\perp = 6$ GeV/c, showing that a single powerlaw cannot describe both the low and high $p_\perp$ spectra. Therefore, fits using only the low $p_\perp$ region of the spectra are more reliable to extract the $\langle p_\perp \rangle$ since most of the yield is at low $p_\perp$. In fact, the value of $\langle p_\perp \rangle$ is below the first reported $p_\perp$ bin of 0.4 GeV/c. The dip in the fractional residual from $p_\perp$ = 2 - 3 GeV/c is due to the feature in the GEANT model of background subtraction previously discussed in Section 3.5.3.

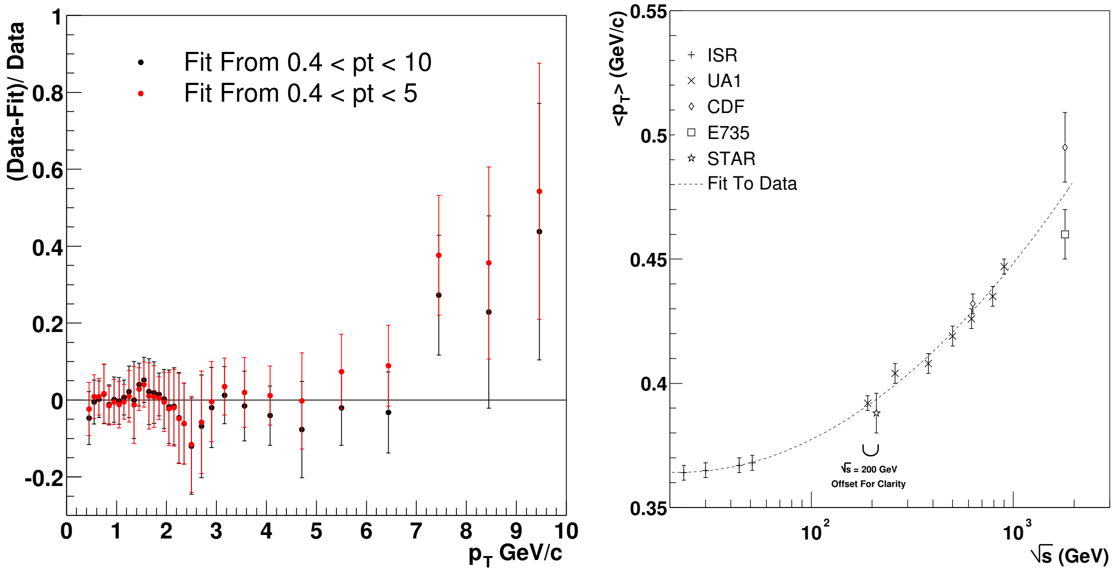

(a) (b)

Figure 4.4: (a) Fractional residuals from $\langle p_\perp \rangle$ fits. Red is for the fit performed between 0.4 GeV/c $< p_\perp <$ 10 GeV/c. Black is for the fit performed between for .4 GeV/c $<$ $p_\perp <$ 5 GeV/c. (b) $\langle p_\perp \rangle$ versus $\sqrt{s}$ from various experiments. Figure adapted from [37].

The extracted $\langle p_\perp \rangle$ agrees with the p+p̄ measurement at the same energy by the UA1 Collaboration of $\langle p_\perp \rangle = 0.392 \pm 0.003$ (stat) $\pm$ 0.024 (sys) [37]. Figure 4.4(b) shows the $\langle p_\perp \rangle$ from this analysis and other p+p̄ analyses versus the center of mass energy. The data are well described by a fit to a quadratic logarithmic function of the form: $\langle p_\perp \rangle(\sqrt{s})$ = (0.4192 $\pm$ 0.0190) - (0.0357 $\pm$ 0.0080) $\log(\sqrt{s})$ + (0.0057 $\pm$ 0.0008) $\log^2(\sqrt{s})$.

4.2.2 Event Multiplicity

Another observable is the inclusive event multiplicity. For all accepted events, the number of tracks within $|\eta| < 0.5$ are counted. The multiplicity distributions are corrected with the statistical methods previously described in Section 3.7. Figure 4.5 shows the multiplicity distribution from the present analysis, both raw and corrected, along with a similar analysis done by the UA5 collaboration for p+p̄ collisions [45]. The uncorrected data is shown to illustrate the scale of the correction. One can see the corrected STAR data matches the UA5 data quite well except at high multiplicity where the correction method begins to become unstable. As one can see from the plot, less than 1% of the total events belong to this multiplicity bin. The STAR corrected data can better match the UA5 data if one uses $\epsilon_{global} = 69\%$. The corrected multiplicity distributions using this efficiency are shown in Figure 4.6.

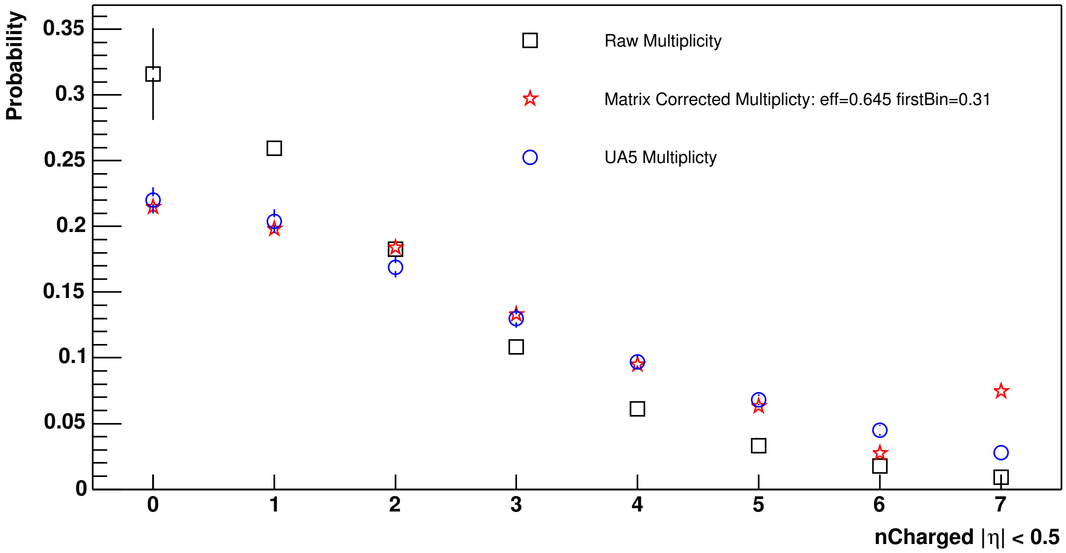

Figure 4.5: p+p event multiplicity using computed $\epsilon_{global} = 64.5\%$.

A negative binomial function (NBN) empirically describes the multiplicity distributions. The NBN functional form is given by

$$P_n(\bar{n}, k) = \begin{pmatrix} n+k-1 \\ k-1 \end{pmatrix} \left(\frac{\frac{\bar{n}}{k}}{1+\frac{\bar{n}}{k}}\right)^n \left(\frac{1}{1+\frac{\bar{n}}{k}}\right)^k. \tag{4.4}$$

The parameter $\bar{n}$ gives the mean of the distribution and k is related to the shape. The fit published by UA5 gives $\bar{n} = 2.48 \pm 0.06$ and $k = 2.3 \pm 0.02 \pm 0.01$ and the the fit to this analysis gives similar values of $\bar{n} = 2.391 \pm 0.007$ and $k = 2.0002 \pm$

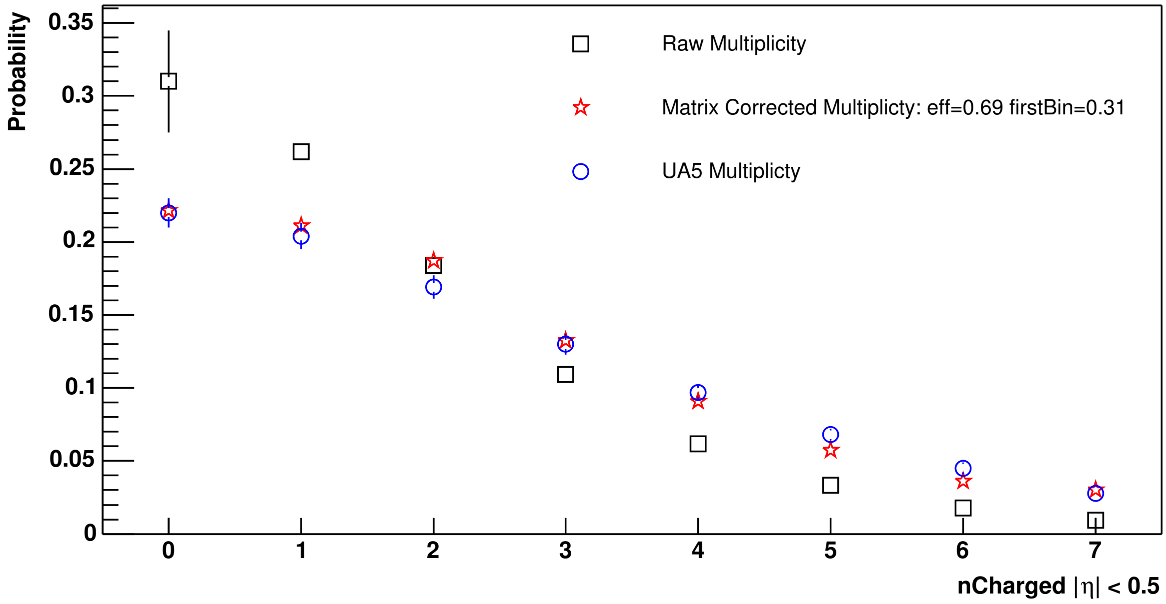

Figure 4.6: p+p event multiplicity using $\epsilon_{global} = 69\%$.

0.003 ± 0.004. The systematic error on k in this analysis is found by holding $\bar{n}$ fixed and varying the fit ranges.

4.2.3 $\langle p_\perp \rangle$ versus Event Multiplicity

Now that the $\langle p_\perp \rangle$ and multiplicity can be found, one would like to study the two quantities versus each other. A collaboration at the ISR first reported that the $\langle p_\perp \rangle$ of a p+p̄ collision increases with the multiplicity [46]. Figure 4.7 shows the $p_\perp$ spectra from the present analysis broken down into three arbitrary uncorrected multiplicity bins. The spectra have been normalized at 0.4 GeV/c. By 6 GeV/c, there is an order of magnitude difference in the yield between the low and high multiplicity classes. This illustrates that high multiplicity events produce high $p_\perp$ particles more frequently than low multiplicity events. In retrospect, this is why great care was used to develop an unbiased vertexing technique in Section 3.4. If the event selection is biased versus multiplicity, then the minimum bias spectra would not sample correctly the differently shaped spectra in each multiplicity class.

The $\langle p_\perp \rangle$ versus the uncorrected multiplicity distribution is shown in Figure 4.8(a).

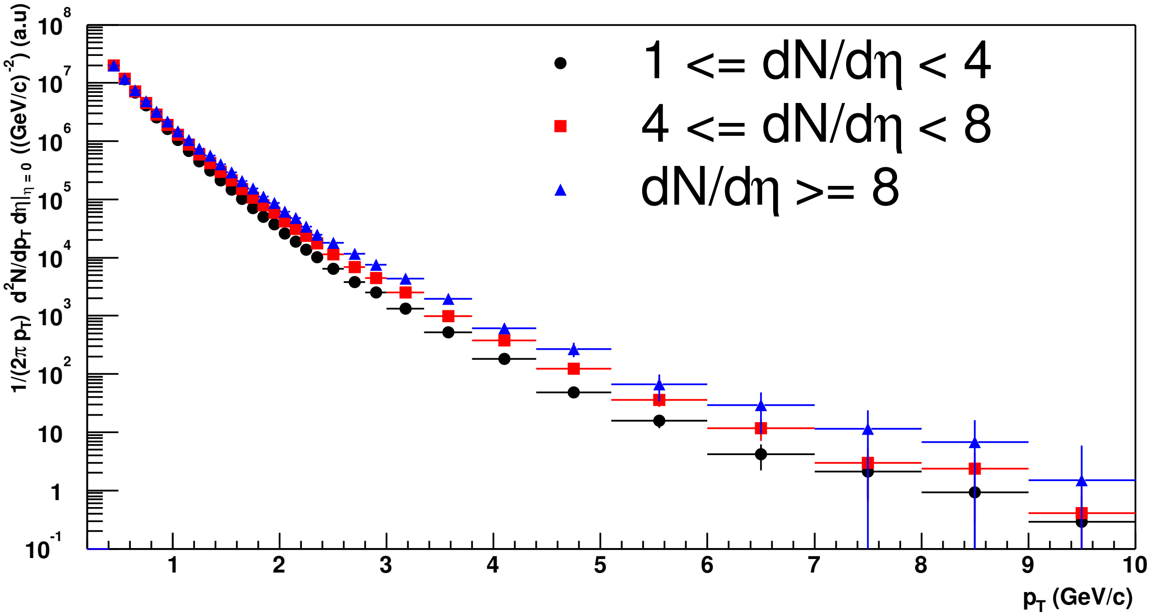

Figure 4.7: p+p inclusive charged hadron $p_\perp$ spectra binned versus multiplicity. Spectra are normalized arbitrarily at 0.4 GeV/c.

Due to the statistical methods needed to correct the multiplicity distribution, the $p_\perp$ spectra cannot be binned with respect to the corrected multiplicity distribution. As the correction is relatively small, as shown in Figure 4.5, this should not impact significantly the physics. The result from a similar analysis of p+p̄ collisions from the UA1 experiment is shown on the same plot. Because the UA1 experiment measured tracks with $|\eta| < 2.5$, the axis for the UA1 collaboration is drawn scaled down by a factor of 5 to account for this difference. A correction done with the HIJING event generator confirms this mapping with a correction valid for more than 5 tracks of $\int_{-.5}^{.5} \frac{dN}{d\eta}\, d\eta = -0.33 + \frac{1}{5}\int_{-2.5}^{2.5} \frac{dN}{d\eta}\, d\eta$

The total $p_\perp$ versus multiplicity is shown in Figure 4.8(b). The corresponding data from the UA1 collaboration also are shown. There is agreement between the two data sets. Moreover, one notices a linear relationship between the total $p_\perp$ from charged particles from the event versus the number of charged particles. Fitting the data from this analysis to a 1^{st} order polynomial gives: $\Sigma p_\perp$= (-0.285 ± 0.169) + (0.490 ± 0.030) dN/dη. This suggests that each additional particle adds roughly 0.5

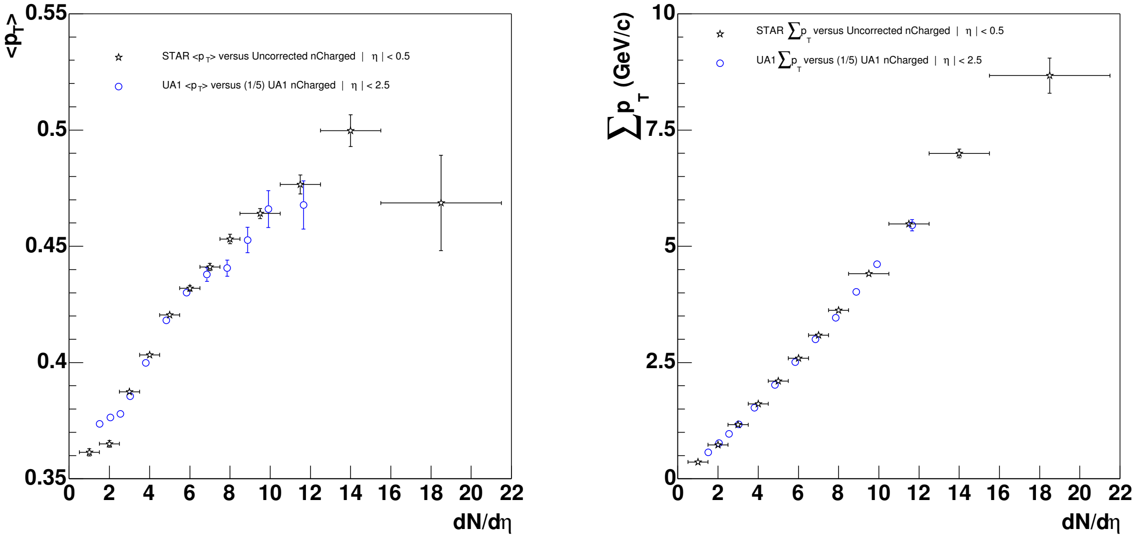

(a) **(b)**

Figure 4.8: (a) $\langle p_\perp \rangle$ versus multiplicity (b) $\Sigma p_\perp$ versus multiplicity. Similar data from UA1 shown for comparison.

GeV/c to the total $p_\perp$ of the event.

Unfortunately, UA5 never published a $p_\perp$ spectrum, and UA1 never published a multiplicity distribution so a more detailed cross-check cannot be performed. Nevertheless, these comparisons verify that the $p_\perp$ spectra do not suffer from a multiplicity bias.

Chapter 5

Comparing Data to Models

5.1 Spectra and the Nuclear Modification Factor

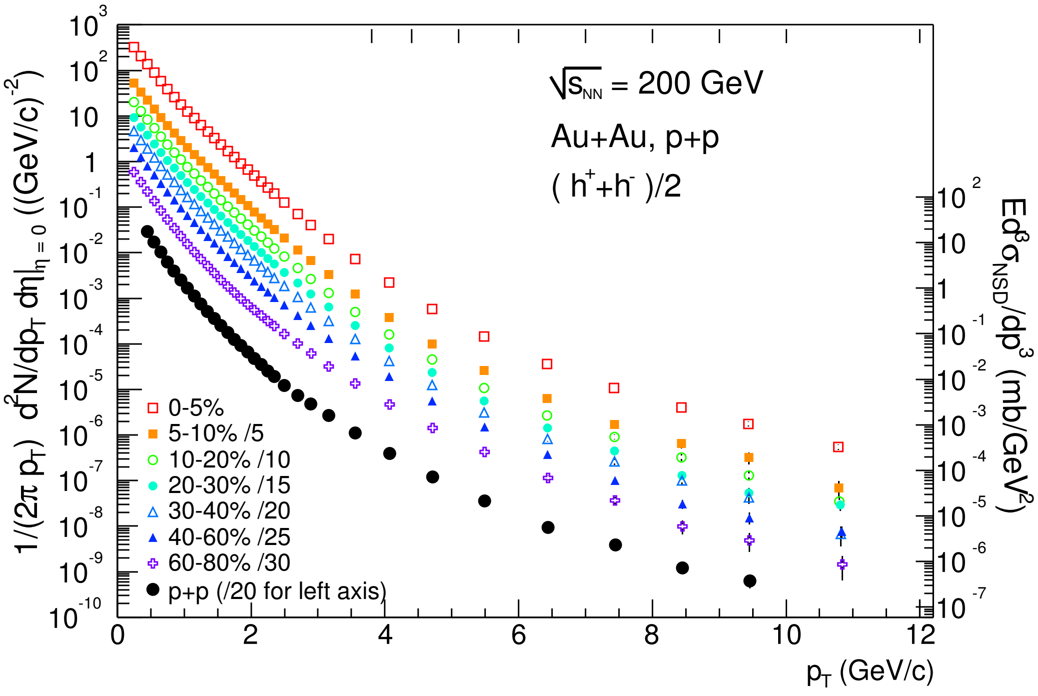

Figure 5.1: Inclusive invariant $p_\perp$ distributions of $(h^+ + h^-)/2$ for centrality-selected Au+Au and p+p NSD interactions. The invariant NSD cross section for p+p is indicated on the right vertical axis.

This analysis will compare the inclusive charged hadron spectra from Au+Au collisions at $\sqrt{s_{\rm NN}}$ = 200 GeV from the STAR collaboration [47] to the inclusive charged hadron spectra from p+p collisions at $\sqrt{s} = 200$ GeV which has been discussed earlier. The spectra from both Au+Au and p+p collisions are shown in Figure 5.1 and the Au+Au spectra are broken down into centrality bins as discussed in Appendix E. This is currently the highest energy set of inclusive charged hadron spectra where both heavy-ions and p+p (or p+$\bar{\text{p}}$) are measured in the same detector. Moreover, the Au+Au analysis extends over 50% higher in $p_\perp$ than the previous highest energy Au+Au measurements at $\sqrt{s_{\text{NN}}} = 130$ GeV [28, 48] due to greater statistics.

Nuclear effects on the inclusive spectra from heavy ion collisions are measured by comparison to the p+p spectra via the nuclear modification factor:

$$R_{AA}(p_\perp) = \frac{d^2N^{AA}/dp_\perp d\eta}{\mathrm{T}_{\mathrm{AA}} d^2\sigma^{NN}/dp_\perp d\eta} \ , \tag{5.1}$$

where $\mathrm{T}_{\mathrm{AA}}=\langle \mathrm{N}_{\mathrm{bin}} \rangle/\sigma_{inel}^{NN}$ from a Glauber calculation accounts for the nuclear collision geometry discussed in Appendix E and we adopt $\sigma_{inel}^{NN} = 42$ mb. The term $d^2\sigma^{NN}/dp_\perp d\eta$ refers to inelastic invariant differential cross section from p+p collisions discussed in Section 3.6.2.

In the absence of any nuclear effects described in the following sections, one expects the high-$p_\perp$ hard process inclusive yield to scale as $\langle \mathrm{N}_{\mathrm{bin}} \rangle$, the mean number of binary nucleon-nucleon collisions. Therefore, if heavy ion collisions behave as a mere superposition of p+p collisions, one would expect $R_{AA}(p_\perp)$ to follow the binary collision limit at high-$p_\perp$ where the hard processes dominate. Because $R_{AA}(p_\perp)$ is scaled by $\langle \mathrm{N}_{\mathrm{bin}} \rangle$, $R_{AA}(p_\perp) = 1$ is the binary scaling limit.

The nuclear modification factors computed from the above spectra are shown in Figure 5.2. Horizontal dashed lines show the Glauber model expectations for scaling of the yield with $\langle \mathrm{N}_{\mathrm{bin}} \rangle$ and $\langle \mathrm{N}_{\mathrm{part}} \rangle$, the mean number of participants, with the shaded bands showing their respective uncertainties summed in quadrature with the p+p normalization uncertainty. The error bars represent the quadrature sum of the Au+Au spectra and the remaining p+p spectrum uncertainties. $R_{AA}(p_\perp)$ extends to higher $p_\perp$ than any previous charged hadron measurement because the previous analyses had lower statistics and used a nucleon-nucleon reference spectrum measured at a different detector, at different center of mass energy, and had a slightly different phase-space acceptance that required many model dependent corrections [28, 48].

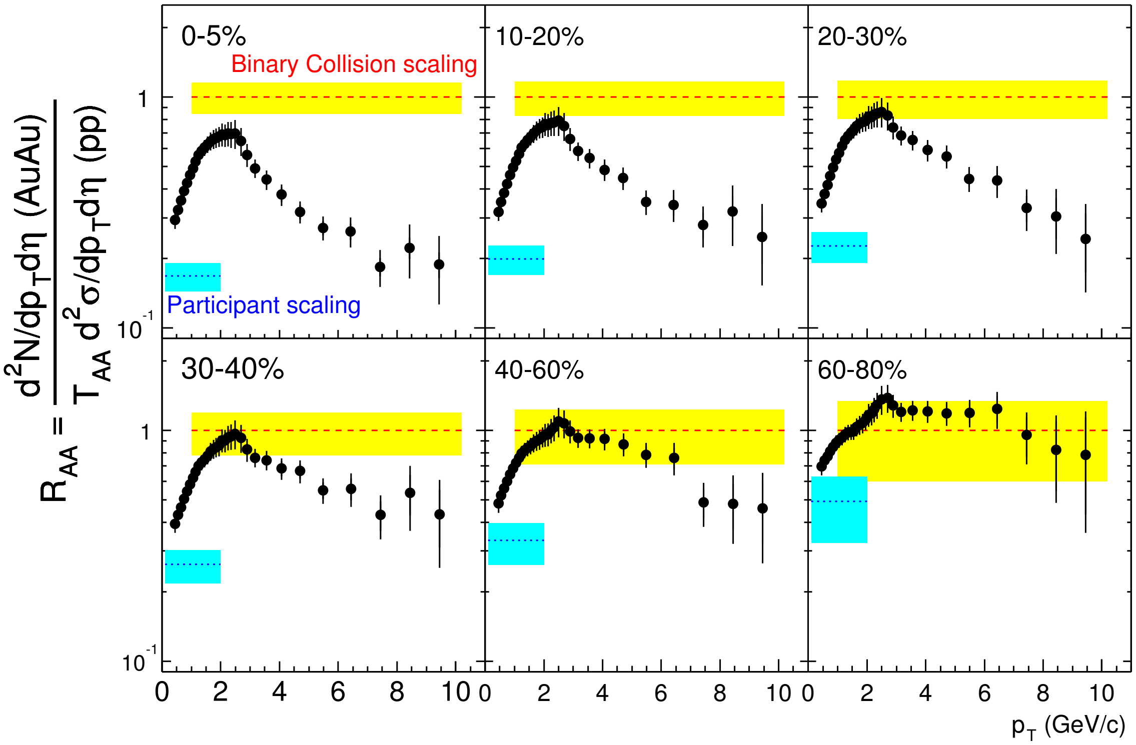

Figure 5.2: $R_{AA}(p_\perp)$ (Eq. 5.1) for $(h^+ + h^-)/2$ in $|\eta|<0.5$, for centrality-selected Au+Au spectra relative to the measured p+p spectrum. Each Au+Au centrality is shown in its own panel while the the p+p spectrum is common to all panels. Uncertainties are described in the text.

There are several striking features to point out in Figure 5.2. First is the steady rise of $R_{AA}(p_\perp)$ towards unity until $p_\perp \sim 2$ GeV/c for all centralities. This area of phase-space is dominated by soft physics that cannot be calculated in perturbative-QCD and therefore offers little predictive power. For the most peripheral collisions (60-80%), $R_{AA}(p_\perp)$ is consistent with unity for $p_\perp > 2$ GeV/c. This shows that peripheral Au+Au collisions behave very much like a superposition of many p+p collisions, which implies the absence of any nuclear effects within errors. As one goes to more central collisions, evidence for nuclear effects becomes apparent by the suppression of $R_{AA}(p_\perp)$ below unity. In the most central Au+Au events, hadron production is suppressed by a factor of 4-5 relative to binary scaled p+p collisions. Figure 5.3(a) displays the data from all centralities on the same scale, without systematic error bars for clarity. As $R_{AA}(p_\perp)$ remains relatively constant for $6 < p_\perp < 10$ GeV/c, Figure 5.3(b) shows the weighed mean of $R_{AA}(p_\perp)$ in this range plotted versus centrality. As one can see from these figures, the suppression of $R_{AA}(p_\perp)$ from unity is smooth as one goes to more central collisions.

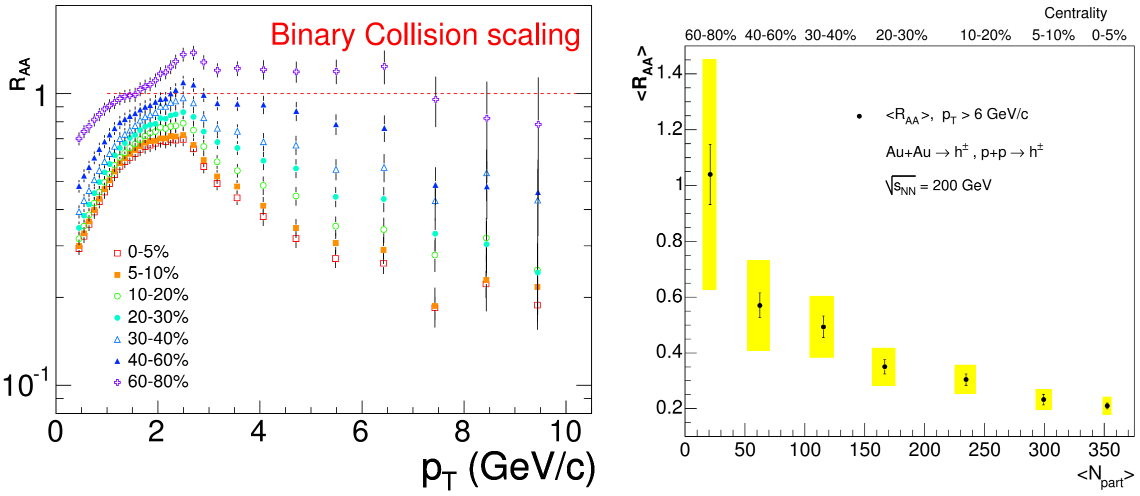

(a) **(b)**

Figure 5.3: (a) $R_{AA}(p_\perp)$ for $(h^+ + h^-)/2$ in $|\eta|$<0.5, for centrality-selected Au+Au spectra relative to the measured p+p spectrum. Systematic uncertainties are not shown for clarity. (b) Weighted mean of $R_{AA}(p_\perp)$ for $p_\perp > 6$ GeV/c versus $\langle \mathrm{N}_{\mathrm{part}} \rangle$. Horizonal systematic uncertainty depends on $\mathrm{N}_{\mathrm{part}}$ while vertical systematic uncertainty depends on $\mathrm{N}_{\mathrm{bin}}$ and p+p normalization uncertainty.

5.2 Models of High-$p_\perp$ Suppression

The characteristics observed in the $R_{AA}(p_\perp)$ measurements, such as the $p_\perp$ and centrality dependence of the magnitude of the suppression, can help to constrain and differentiate between theoretical models that strive to determine the nuclear effects that cause the suppression. This section will discuss various theoretical models and compare these models to the data. The theoretical work will be presented in a quasi-chronological order because the data presented here has led to many modifications of the models. The body of theoretical work can be placed into two distinct categories depending upon the generator of the suppression. The initial-state models argue that the suppression is determined by the properties of the incoming nuclei. The final-state models argue that properties of the system after the initial collision of the nuclei lead to the suppression.

5.2.1 Models incorporating initial-state effects

Parton Saturation Model

A leading initial-state model is the Parton Saturation Model [49], which argues that the *initial* production of high-$p_\perp$ particles is suppressed with respect to $\mathrm{N_{bin}}$ scaling. Consider an external probe interacting with a nuclear target with A nucleons. Due to the uncertainty principle, the interaction develops over large longitudinal distances $z \sim 1/mx$, where m is the nucleon's mass and x is fraction of the nucleon's momentum that the parton possesses. When z becomes larger than the nuclear diameter, the probe becomes sensitive to the entire longitudinal gluon distribution and the system is considered to be saturated. The probe is also sensitive to the transverse distribution within area $\sim 1/Q^2$ as shown in Figure 5.4(a) [50].

Taking the cross-section of probe-nucleon scatterings to be $\sigma \sim \alpha_s/Q^2$, the interaction probability is given by

$$\sigma\rho_A \simeq \frac{xG_A(x,Q^2)\alpha_s}{\pi R_A^2 Q^2}, \tag{5.2}$$

where $xG_A(x,Q^2)$ is the number of gluons, α_s is the running QCD coupling, and R_A is the nuclear radius. Coherence ensues when the interaction probability is much larger than unity. By solving Equation 5.2 for unity, one can determine the saturation scale, which is the approximate upper limit of the momentum transfer where the Saturation Model is applicable:

$$Q_{sat}^2 \approx \alpha_s \, \frac{xG_A(x,Q_{sat}^2)}{\pi R_A^2}. \tag{5.3}$$

Therefore one expects saturation effects to be present for $Q^2 < Q_{sat}^2$. Calculations put $Q_{sat}^2 \sim$ 1-2 GeV for RHIC energies and acceptances [51].

In this model, the gluon distribution function can be derived from first principles [51] and is shown in Figure 5.4(b). Above the saturation scale, the number of gluons

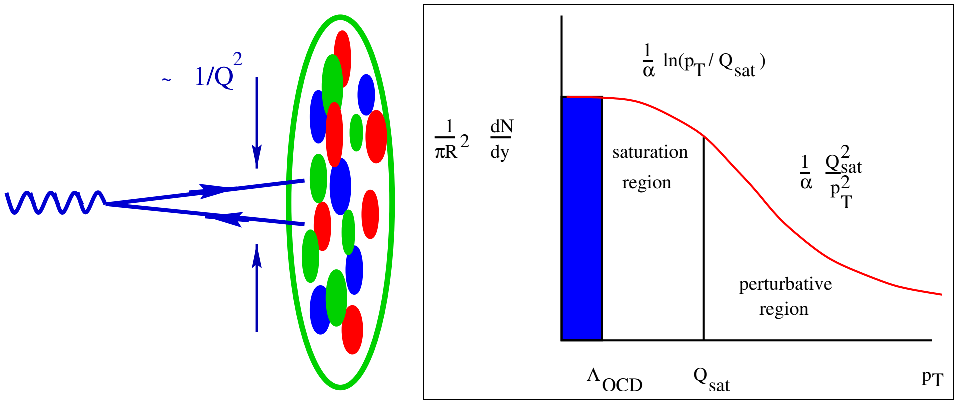

(a) **(b)**

Figure 5.4: (a) Parton density in the Saturation Model. Figure taken from [50]. (b) Gluon distribution function in the Parton Saturation Model. Figure taken from [51].

increases as Q^2_{sat}, but below they have a logarithmic dependence. At this point the cross section saturates since the number of gluons that can be resolved stops growing. By expanding a scattering amplitude equation around Q^2_{sat}, one can demonstrate that in the Saturation Model final state particles should be suppressed up to Q^2_{sat}/Λ_{QCD} which is approximately 5-10 GeV/c at RHIC energies [52, 49].

The Saturation Model can offer predictions for the magnitude of the suppression of high-$p_\perp$ particles in heavy ion collisions. However, this model is based on properties of a dense nuclear wave-function ($\sigma\rho_A > 1$) and quantitative predictions are not possible currently for p+p collisions and thus $R_{AA}(p_\perp)$. The model can predict $R_{CP}(p_\perp)$, the $\langle \mathrm{N_{bin}} \rangle$-normalized ratio of central to peripheral Au+Au spectra. This is roughly equivalent to $R_{AA}(p_\perp)$ as the most peripheral Au+Au spectra were shown to be consistent with binary scaling. $R_{CP}(p_\perp)$ constructed with the numerator from the most central data and the denominator from each of the two most peripheral data sets are shown in Figure 5.5 along with predictions from the Saturation Model [49, 47]. The error bars show the quadrature sum of statistical and uncorrelated systematic uncertainties. The shaded bands illustrate the systematic uncertainty on $\langle \mathrm{N_{bin}} \rangle$ and $\langle \mathrm{N_{part}} \rangle$. The Saturation Model accurately reproduces the magnitude of the high-$p_\perp$ suppression in the left panel but does not reproduce the low $p_\perp$ behavior. Although the $p_\perp$ dependence of the suppression is not modelled correctly, the average value of the magnitude of the suppression is reproduced approximately in the right panel. Despite inaccurately describing the $p_\perp$ and centrality dependence of the data, the Saturation Model must still be considered as a possible mechanism for suppression because of its qualitative agreement with the data at high-$p_\perp$.

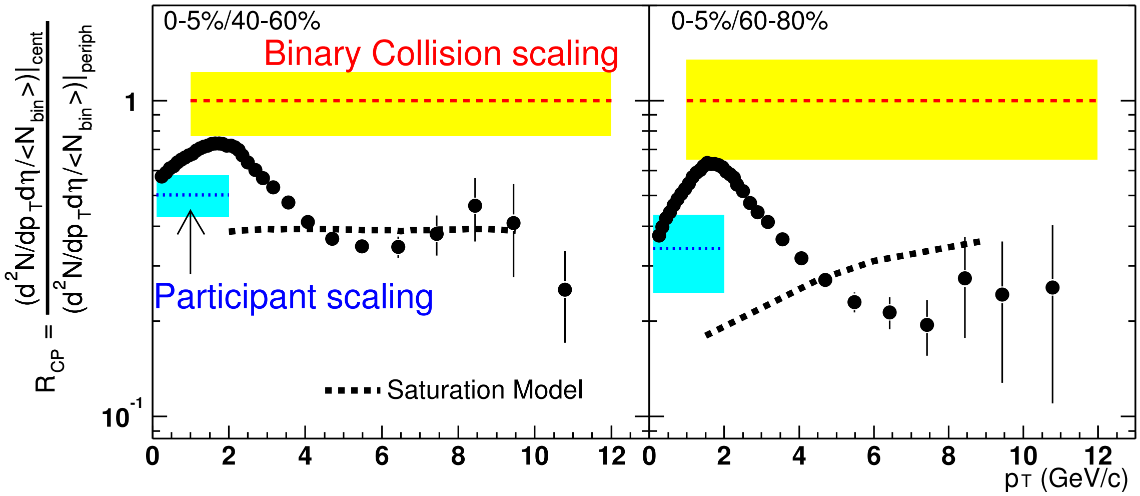

Figure 5.5: $R_{CP}(p_\perp)$ vs $p_\perp$ for $(h^+ + h^-)/2$ in $|\eta|<0.5$ along with predictions from the Saturation Model [49, 47].

Nuclear Shadowing

Nuclear shadowing, the modification of the nucleon structure functions in nuclei, may also lead to the suppression of particles at high-$p_\perp$. It has been established from nuclear deep-inelastic scattering that there is the depletion of the nuclear structure functions at low x and enhancement at intermediate x relative to the proton structure functions [54, 55]. Although the source of the modification is not completely understood, two of the leading explanations of shadowing are recombination of long wavelength partons and multiple interactions of the incoming parton along the path length of the nucleus. The EKS [53] parametrization for the shadowing of nuclear structure functions is shown in Figure 5.6 for up quarks and gluons in Au-197.

Calculations within a perturbative-QCD framework can predict a value of $R_{AA}(p_\perp)$ using the shadowed nuclear structure functions. These predictions are shown in Figure 5.10 labelled as “Shadowing Only”. Though they predict some suppression at

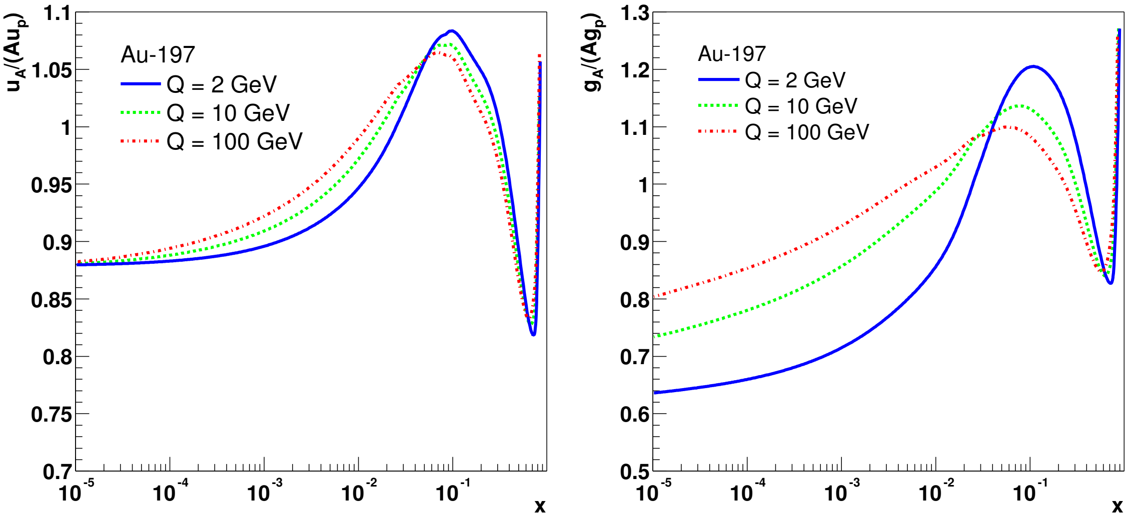

(a) **(b)**

Figure 5.6: Predictions of (a) quark and (b) gluon shadowing for Q = 2 GeV (solid curves), Q = 10 GeV (dashed curves), and Q = 100 GeV (dot-dashed curves). Calculations from [53].

intermediate $p_\perp$, they predict a value at high-$p_\perp$ consistent with unity and inconsistent with the most central data. Clearly shadowing alone cannot be responsible for the large suppression exhibited by the data.

Cronin Effect

Although it leads to an *enhancement* of $R_{AA}(p_\perp)$ with respect to $\mathrm{N_{bin}}$ scaling, the Cronin effect [56] should be included in the discussion of initial-state effects for completeness. This effect usually is attributed to multiple scattering of projectile partons within the incident nucleus. This is accounted for in most models by adding a random Gaussian transverse boost, δk_T^2, to the projectile partons before hadronization. Figure 5.7 shows $R_{AA}(p_\perp)$ in central heavy ion collisions for different center of mass energies. The enhancement seen in the lower energy data is attributed to the Cronin effect. The predictions of the Cronin effect for the $R_{AA}(p_\perp)$ presented in this work are shown in Figure 5.10 labelled as "Shadowing and Cronin". Although a Cronin type enhancement may be present, it must be countered by other phenomena, such as saturation or energy loss, in order to reduce $R_{AA}(p_\perp)$.

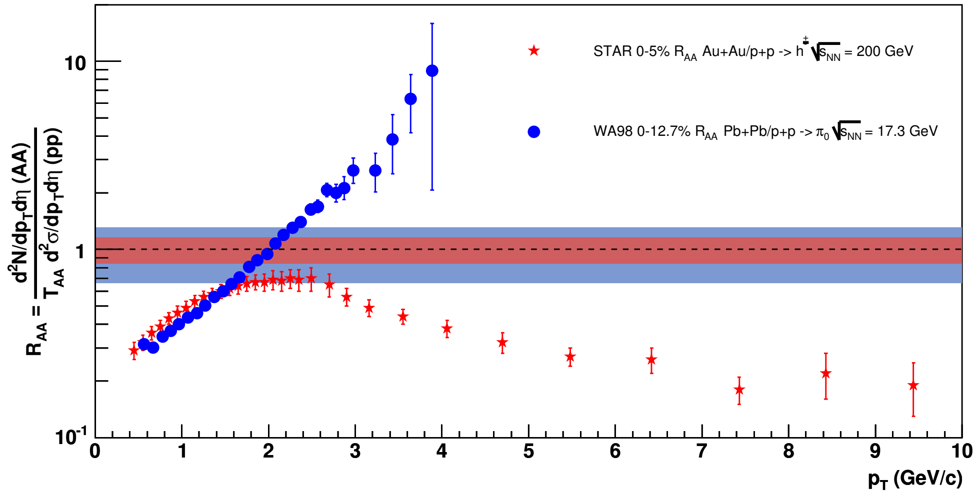

Figure 5.7: $R_{AA}(p_\perp)$ at $\sqrt{s_{\rm NN}} = 17.3$ and 200 GeV for central collisions: red is from STAR, blue is from WA98 [57] data. Uncertainty on $\langle {\rm N_{bin}} \rangle$ shown in respective shaded bands.

5.2.2 Models incorporating final-state effects

Final-state effects that occur after the initial collision also can be used to explain the measured high-$p_\perp$ suppression. These approaches assume that the outgoing "particles" experience some form of energy loss. Partonic energy loss models predict that this energy loss occurs before partons hadronize, while hadronic energy loss models contest that at least some of the energy loss occurs during or after hadronization. The following sections compare these models to data.

Hadronic and pre-hadronic energy loss

Assuming that hadron formation time is dependent upon the time to build up the hadronic wavefunction, basic quantum mechanical arguments lead to a formation time which is linear in energy. Taking hadrons as massless, the formation time $t_f \approx ER^2 \approx$ 10 fm/c at RHIC energies [58]. Under this assumption, particles most likely will hadronize within the fireball [59]. Opponents of this model, argue that since hadrons have mass, an alternate model of the formation time, e.g. $t_f \approx \frac{E}{m}R$, should be used. This formulation gives $t_f \approx$ 35 - 70 fm/c [60] for pions which suggests hadronization will occur outside the fireball. Moreover, these formation arguments only hold in vacuum as interactions in the medium will increase the hadron formation time [60].

Nevertheless, one can argue that inelastic hadronic or "pre-hadronic" interactions could be a dominant nuclear effect. A "pre-hadron" is a parton that is assumed to almost instantly pick up an anti-colored parton from the vacuum to achieve color neutrality, but has not yet built up its wavefunction to form a hadron. This model incorporates interactions between pre-hadrons with nucleons from the projectiles, with other pre-hadrons, as well as produced hadrons. In order to be a purely hadronic model, interactions with quarks and gluons in the early stages of the collision are neglected. A step-wise scattering cross section is used which is reduced for all times before hadronization, and jumps to the full value for all times after hadronization. Also presented is an alternate model of the cross section that assumes a linear increase with time until the full value is reached at hadronization and then remains constant for all later times [58].

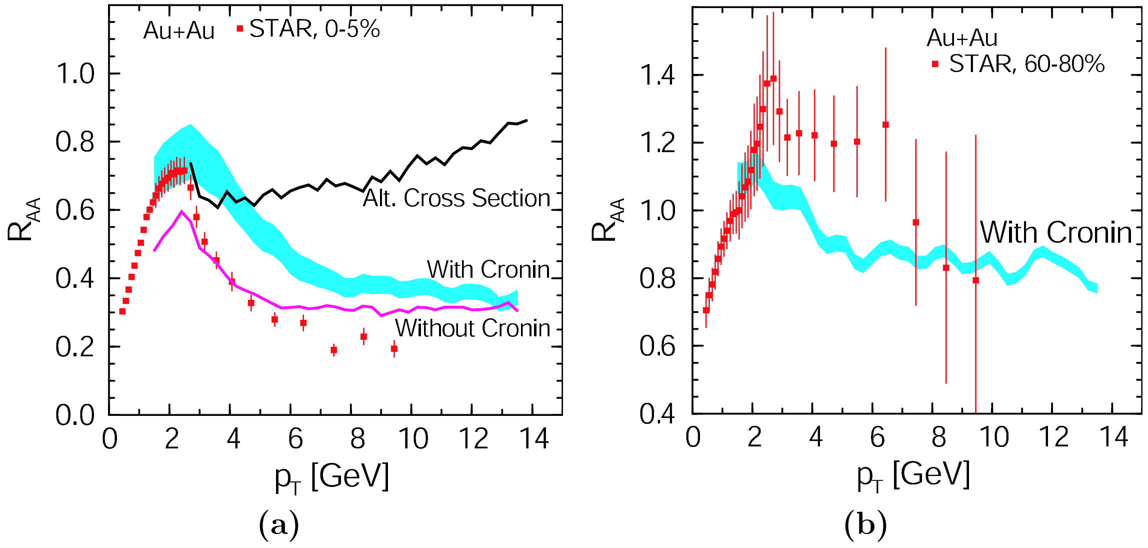

Figure 5.8: $R_{AA}(p_\perp)$ in the Hadronic Energy Loss Model (a) from central collisions. The shaded band incorporates the Cronin effect plus hadronic energy loss, the pink curve neglects the Cronin effect, and the black curve is for the alternate formulation of the pre-hadron scattering cross-section. (b) from peripheral collisions. Shaded band incorporates Cronin effect plus hadronic energy loss. Figures adapted from [61].

Figure 5.8(a) shows the predictions of this model for central Au+Au collisions. The blue shaded band is the range of predictions from hadronic energy loss with the addition of various levels of Cronin enhancement which account for the width of the band. Although the $p_\perp$ dependence is roughly reproduced by the blue band, it underestimates the magnitude of the suppression. The pink curve shows the calculation without the addition of the Cronin effect in order to illustrate that the model, not the Cronin effect, reproduces the peak-structure around $p_\perp = 2$ GeV/c. The alternate cross section model is shown by the black curve in Figure 5.8(a), and it does not match the data as it predicts $R_{AA}(p_\perp)$ increasing to unity at high-$p_\perp$. The prediction for peripheral Au+Au collisions is displayed in Figure 5.8(b). The model over-predicts the level of suppression except at $p_\perp > 7$ GeV/c. Although a hadronic energy loss model roughly describes the trends in the data, it is dependent upon formation time arguments and a step-wise scattering cross section that are contestable.

Partonic Energy Loss

Models incorporating partonic energy loss argue that high energy partons propagating through matter lose energy via induced gluon radiation, with the average energy loss strongly dependent upon the color charge density of the medium

$$\langle\frac{dE}{dL}\rangle \propto \int_{\tau_0}^{R_A} \rho(\tau)(\tau-\tau_0)\ln\frac{2E}{\tau\mu^2}d\tau, \tag{5.4}$$

where $\rho(\tau)$ is the radial gluon density, E is the energy of the parton, and μ^2 is the screening scale taken to be approximately equal to $\langle p_\perp^2\rangle$ of the parton [62]. Due to the presence of thermal gluons, there is a detailed balance between stimulated gluon emission and absorption by the propagating parton [63]. In this model, an effective mean quark energy loss of:

$$\langle\frac{dE}{dL}\rangle_{1d} = \epsilon_0(E/\mu_0 - 1.6)^{1.2}/(7.5 + E/\mu_0) \tag{5.5}$$

is used with $\epsilon_0 = 2.04$ GeV/fm and $\mu_0 = 2.0$ GeV chosen to match the most central data [47, 64] and is shown in Figure 5.9(a). The energy loss experienced by a traversing parton is directly proportional to this quantity, with the exact form dependent upon whether the model of the gluon distribution is assumed to be static or expanding. Assuming a static source, the total energy loss is just this quantity times the source diameter. The maximal energy loss, which occurs at the earliest time when the density is largest is given by:

$$\frac{dE}{dL_0} = (R_A/2\tau_0)\langle\frac{dE}{dL}\rangle_{1d} \tag{5.6}$$

with the source radius $R_A = 6.5$ fm and the source formation time $\tau_0 = 0.2$ fm [64]. For a 10 GeV parton, this formulation gives $\langle\frac{dE}{dL}\rangle_{1d} = 0.7$ GeV/fm and $\frac{dE}{dL_0} = 11.5$ GeV/fm, which is about 23 times higher than in a cold Au nucleus as extracted from lower energy data [62]. Therefore, the gluon density also must be 23 times higher. With the inclusion of parton shadowing in the above calculation, this value increases to 30. Due to the over three-fold increase in the mean transverse energy from cold nuclear matter, this corresponds to an initial energy density of $\epsilon = 15$ GeV/fm^3, well over the critical density needed for deconfinement from lattice calculations [64].

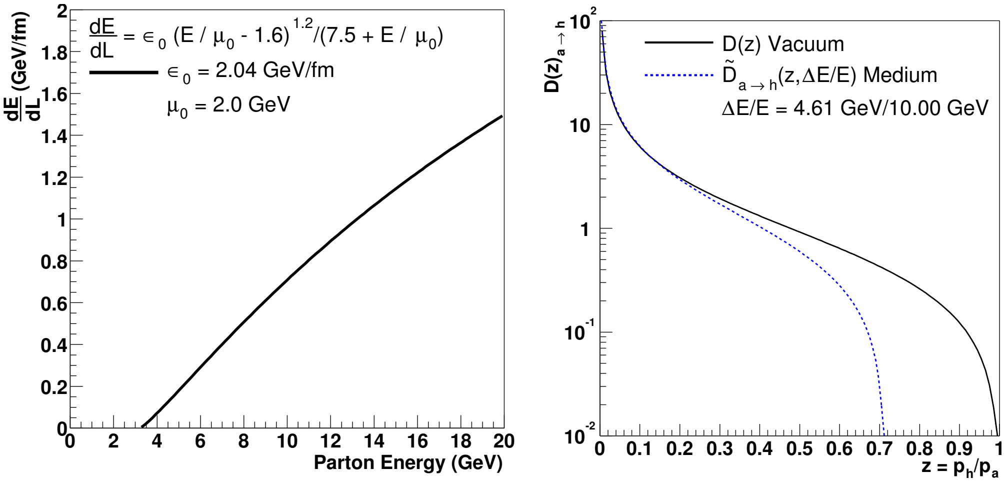

(a) (b)

Figure 5.9: (a) Effective parton energy loss versus parton energy. The values of ϵ_0 and μ_0 have been fit to the data. Calculations from [47, 64]. (b) Modification of the fragmentation functions due to partonic energy loss. Calculations from [7, 65].

The energy loss mechanism is incorporated into the calculation by a softening of the fragmentation function dependent upon the energy loss. For a parton a of energy E to fragment into a hadron h with momentum fraction z of the parent parton:

$$\widetilde{D}_{a\to h}(z) \approx \frac{1}{1-0.6\frac{\Delta E}{E}} D_{a\to h}\left(\frac{z}{1-0.6\frac{\Delta E}{E}}\right), \tag{5.7}$$

where $\frac{\Delta E}{E}$ is the fractional partonic energy loss and 0.6 is primarily a result of a unitarity correction in the pQCD model [65]. An example of the softening of the fragmentation function is shown in Figure 5.9(b) for a 10 GeV parton in a static source. The high z depletion of the fragmentation function generates the suppression of high-$p_\perp$ particles in the calculation.

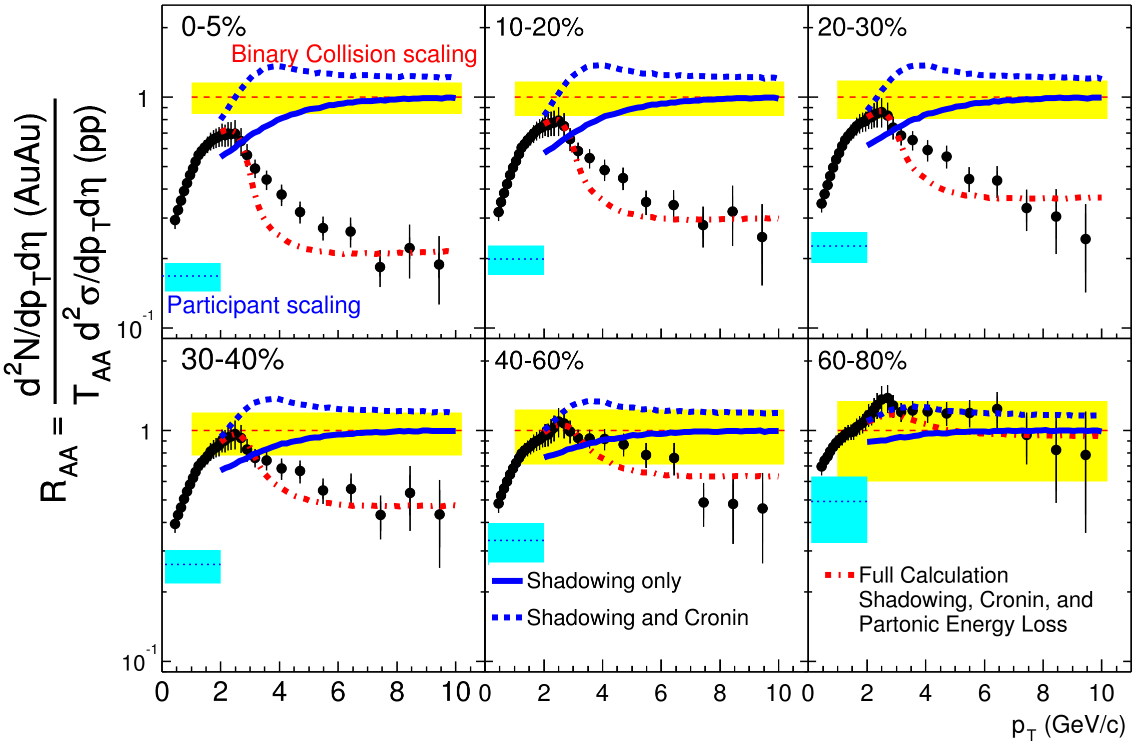

Figure 5.10: $R_{AA}(p_\perp)$ (Eq. 5.1) for $(h^+ + h^-)/2$ in $|\eta|<0.5$, for centrality-selected Au+Au spectra relative to the measured p+p spectrum is shown. Each Au+Au centrality is shown in its own panel as labelled while p+p spectrum is common to all panels. Uncertainties described in Section 5.1.

Figure 5.10 shows the model calculations of $R_{AA}(p_\perp)$ from this partonic energy loss formulation, labelled as “Full Calculation” along with the data. The figure also shows the results from calculations that do not incorporate energy loss: shadowing and shadowing plus the Cronin Effect. In the most peripheral 60-80% bin, one can see that the non-energy loss calculations reproduce the data, suggesting that partonic energy-loss does not occur at this centrality. As one goes to more central collisions, the prediction of the non-energy loss calculations do not change significantly, but the data becomes suppressed with respect to unity. This suggests that shadowing alone cannot explain the magnitude of the suppression in the central collision data.

The predictions of the energy loss model, which also includes shadowing and the Cronin effect (See Sections 5.2.1 and 5.2.1), are more promising. In the most peripheral 60-80% bin, the model matches the data and reduces to the non-energy loss calculations due to the smaller overlap region between the nuclei which leads to a smaller density and traversed path length. The predictions of the magnitude of the suppression continue to match the data as one goes to more central collisions. Throughout all centrality bins, the model accurately reproduces the $p_\perp$ dependence of the data. As previously discussed, the magnitude of the suppression is fit by adjusting ϵ_0 and μ_0 to match the most central data, but the $p_\perp$ and centrality dependence of the suppression is intrinsic to the model. Of all the models presented, partonic energy loss best reproduces the data signaling that partonic energy loss may be the generator of the high-$p_\perp$ suppression observed in Au+Au collisions.

5.3 Applications to d+Au Collisions

While $R_{AA}(p_\perp)$ constructed from Au+Au and p+p collisions is able to constrain the above models, it cannot distinguish between them. Although partonic energy loss best describes the data, the initial-state Saturation Model and the final-state Hadronic Energy Loss Model both qualitatively describe the trends in the data. Deuteron-Gold (d+Au) collisions at the same center-of-mass energy as the previously described p+p and Au+Au collisions serve as an essential control experiment to distinguish between initial- and final-state mechanisms for the high-$p_\perp$ suppression. While p+Au collisions would be ideal for this purpose, the technical constraints described in Section 2.1.2 prevented RHIC from running this system.

Figure 5.11 shows $R_{AB}(p_\perp)$ constructed from the minimum bias and the 20% most central d+Au inclusive charged hadron spectra described in Appendix F. The figure also shows $R_{AA}(p_\perp)$ from the most central Au+Au collisions for comparison. In order to highlight the values of $R_{AA}(p_\perp)$ and $R_{AB}(p_\perp)$ near unity, a linear scale is used. The

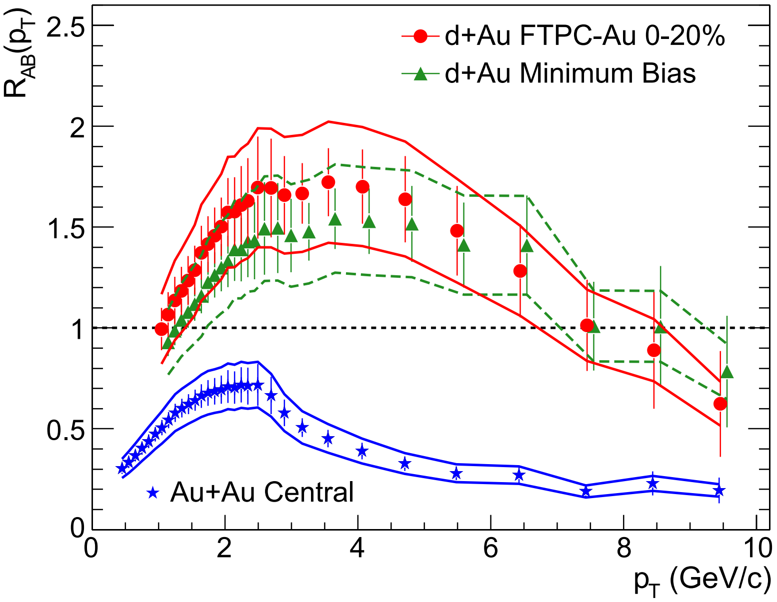

Figure 5.11: $R_{AA}(p_\perp)$ at $\sqrt{s_{\rm NN}} = 200$ GeV for $(h^+ + h^-)/2$ in $|\eta|$<0.5, for centrality-selected d+Au and Au+Au spectra relative to the measured p+p spectrum. Uncertainties are described in text.

vertical lines show the statistical uncertainty while the error bands show the effects of the uncertainty on $\langle \mathrm{N_{bin}} \rangle$ and the normalization of the p+p and d+Au spectra. Clearly, there is no suppression in the range $2 < p_\perp < 7$ GeV/c. Above 7 GeV/c there is a downward trend in the data, but more statistics are needed to confirm this result. This suppression trend may be explained by the shadowed parton distribution function at $x = 0.2 - 0.8$ as will be discussed in Section 5.3.3.

5.3.1 Initial-state Saturation Model

As described in Section 5.2.1, the Saturation Model predicts that properties of the nuclear wave-function prevent the initial production of high-$p_\perp$ particles. Since the Au nucleus is present, and the x and Q^2 in the parton frame are roughly the same as in Au+Au collisions, the Saturation Model originally predicted a suppression of ~30% of high-$p_\perp$ particles in d+Au collisions with respect to binary-scaled p+p collisions [49]. This prediction is summarily ruled out by the data shown in Figure 5.11 and thus the suppression of high-$p_\perp$ particles at mid-rapidity can be attributed to final-state effects.

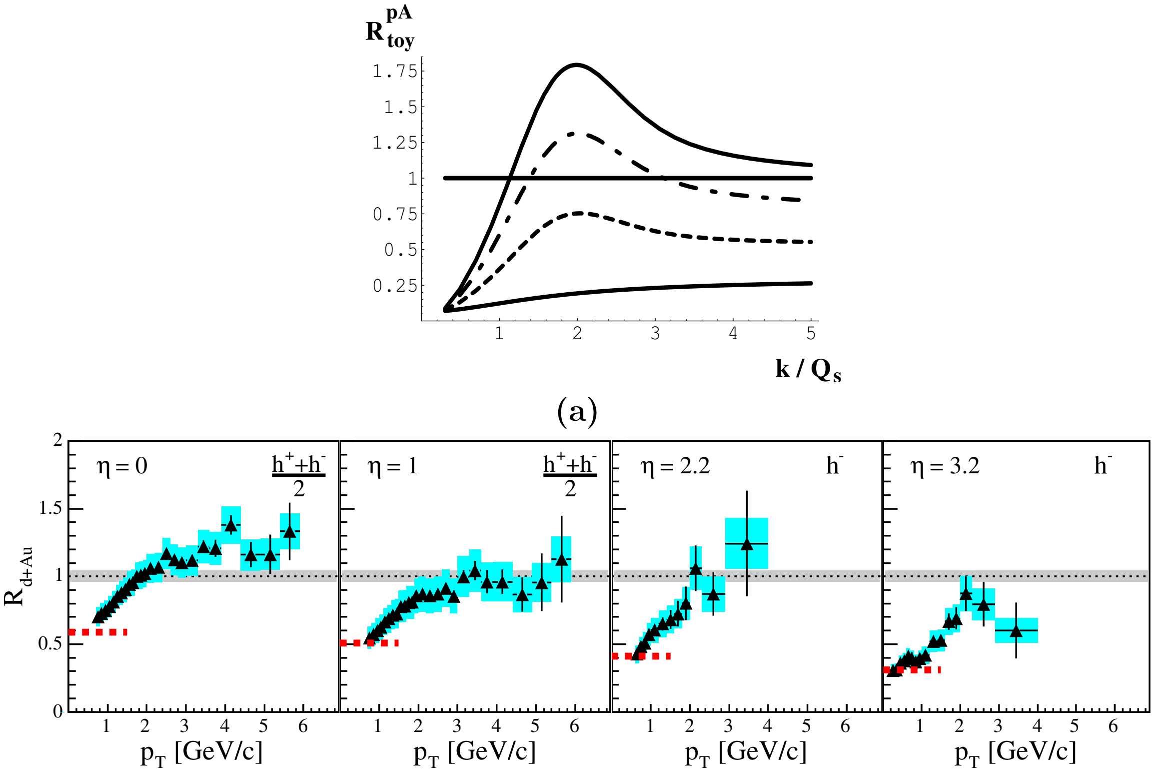

(a)

(b)

Figure 5.12: (a) A toy model of high-$p_\perp$ suppression in d+Au collisions plotted versus $k_t/Q_s \propto p_\perp$. The lower lines are at higher energy or rapidity which are degenerate in this model. Figure taken from [66]. (b) $R_{AB}(p_\perp)$ for d+Au spectra at $\sqrt{s_{\rm NN}} = 200$ GeV versus rapidity from the BRAHMS experiment at RHIC [67].

After the presentation of this data, the Saturation Model was reformulated. It now concedes that suppression at mid-rapidity is due to final-state effects. However, at higher rapidity and thus lower x, since $x \sim e^{-y}\frac{m_\perp}{\sqrt{s}}$, quantum evolution corrections become important, leading to a suppression in the initial gluon production [66]. A toy model of the suppression versus energy or rapidity is shown in Figure 5.12(a). The lower the curve, the higher the energy or rapidity it represents as this model is degenerate in energy and rapidity. Preliminary results from $\sqrt{s_{\rm NN}} = 200$ GeV d+Au collisions at higher pseudorapidity (1<η<3.2) in the deuteron fragmentation region are shown in Figure 5.12(b) [67]. This data indicates an increasing suppression with increasing pseudorapidity, which may lend credence to the Saturation Model at high rapidities (low x).

In order to test this model, one needs to study $R_{AB}(p_\perp)$ as a function of rapidity in both the Au and deuteron fragmentation directions. In the deuteron fragmentation region, the effects of saturation in the Au wavefunction will be enhanced and the low final-state hadron densities preclude energy loss models. The opposite is true in the Au fragmentation region: the final-state particles will be more sensitive to the deuteron wave function and the hadron densities will be higher in this rapidity region [66]. To this date, RHIC experiments have not investigated the full rapidity region as it requires RHIC to interchange the directions of the Au and deuteron beams, or for the experiments that can probe this rapidity region to rotate their apparatus.

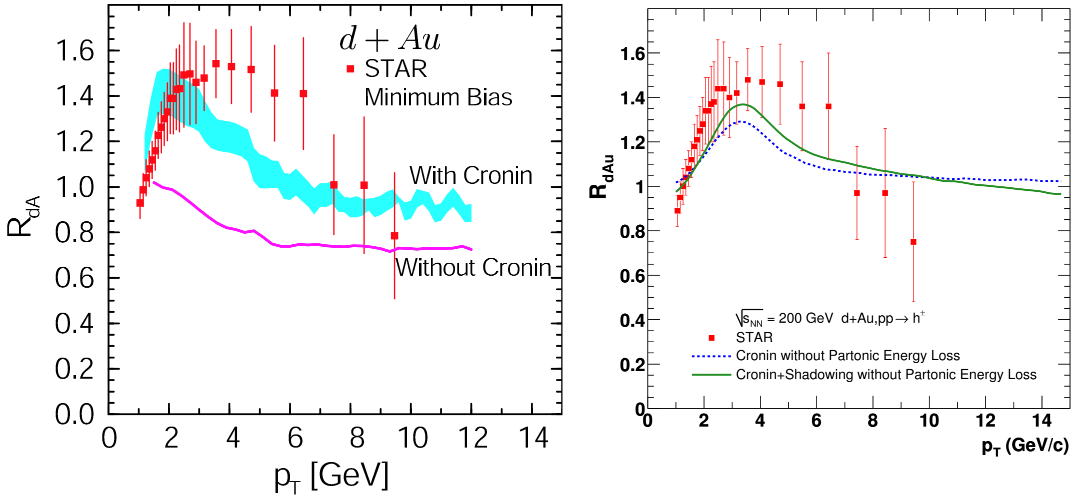

(a) **(b)**

Figure 5.13: (a) Prediction of the Hadronic Energy Loss Model for $R_{AB}(p_\perp)$ along with data from minimum bias d+Au collisions at $\sqrt{s_{\mathrm{NN}}} = 200$ GeV. Figure adapted from [61]. (b) Predictions without partonic energy loss but incorporating the Cronin effect in blue and the addition of shadowing in red. Calculations are from [68].

5.3.2 Hadronic Energy Loss

Hadronic energy loss models still predict some energy loss in d+Au collisions [61] due to inelastic interactions of leading pre-hadrons with the nucleons from the projectiles. A smaller suppression is predicted because pre-hadrons will not interact with other pre-hadrons or secondary formed hadrons as the density is insufficient. The predictions from this model are shown in Figure 5.13(a) along with the minimum bias data presented above. The curve is the prediction from the model alone while the hatched band also has the Cronin effect incorporated. The model does not reproduce the $p_\perp$ dependence as it over-estimates the suppression except in the highest $p_\perp$ bins.

5.3.3 Partonic Energy Loss

In contrast to hadronic energy loss scenarios, one does not expect any suppression in d+Au collisions due to partonic energy loss. There simply are not enough gluons to interact with the traversing parton to induce significant radiation. Therefore, the only nuclear effects present are the Cronin effect and possibly shadowing. This model argues for an enhancement, not a suppression, of $R_{AB}(p_\perp)$. Predictions from this model are shown in Figure 5.13(b) along with the data. The blue dashed line incorporates the Cronin effect while the solid green line has the addition of shadowing with the EKS [53] parametrization of the parton distribution functions. In the above parametrization, the target parton distribution at $x \sim 0.2$ - 0.8 is suppressed, which manifests itself in the suppression of particles of $p_\perp \geq 10$ GeV/c. This is known as the EMC effect [69]. Once again, this model qualitatively describes the data, which reinforces the validity of a partonic energy loss model in describing the high-$p_\perp$ suppression in Au+Au collisions.

5.4 Other Observables To Differentiate Between Models

By comparing to spectra from p+p and d+Au collisions, one can conclude that the high-$p_\perp$ suppression witnessed in $\sqrt{s_{\rm NN}} = 200$ GeV Au+Au collisions at mid-rapidity predominately is a final state effect. The exact mechanism of the energy loss, whether it is partonic or hadronic, cannot be determined from the inclusive spectra or $R_{AA}(p_\perp)$ alone. Fortunately, other analyses of the same data, such as statistical jet studies, can differentiate between these models. Jets are reconstructed on a statistical basis by studying the two-particle azimuthal distribution,

$$D(\Delta\phi) \equiv \frac{1}{N_{trigger}} \frac{1}{\epsilon} \frac{dN}{d(\Delta\phi)} \tag{5.8}$$

for p+p d+Au, and Au+Au collisions [70, 71, 72]. Only particles within $|\eta|<0.7$ are included in the analysis. $N_{trigger}$ is the number of particles within $4<p_\perp^{trig}<6$ GeV/c, referred to as trigger particles which define the jet axis. The distribution results from the correlation of each trigger particle with all associated particles in the same event having $2<p_\perp<p_\perp^{trig}$ GeV/c, where ϵ is the tracking efficiency of the associated particles. The normalization uncertainties are less than 5%. Associated particles that are close in azimuth to the trigger particle ($\Delta\phi \approx 0$) predominately come from the jet defined by the trigger. Associated particles that fall away from the trigger particle ($\Delta\phi \approx \pi$) likely are from the away-side partner of the trigger jet.

Figure 5.14(a) shows the background-subtracted $D(\Delta\phi)$ for p+p, central d+Au, peripheral and central Au+Au collisions. For p+p collisions notice the clear two peak-structure. This is evidence for the back-to-back structure of jets which is expected from momentum conservation. This two peak structure also is evident in d+Au and peripheral Au+Au collisions, which is expected from the $R_{AA}(p_\perp)$ analysis that has shown that these collision systems appear very much like p+p for high-$p_\perp$ particles. However, in central Au+Au collisions, $D(\Delta\phi)$ looks very different with a clear suppression of the away-side peak. Moreover, the suppression of the away-side jet increases with centrality just as the suppression of $R_{AA}(p_\perp)$ increases with centrality. Figure 5.14(b) shows the ratio of the background-subtracted near- and away-side jet

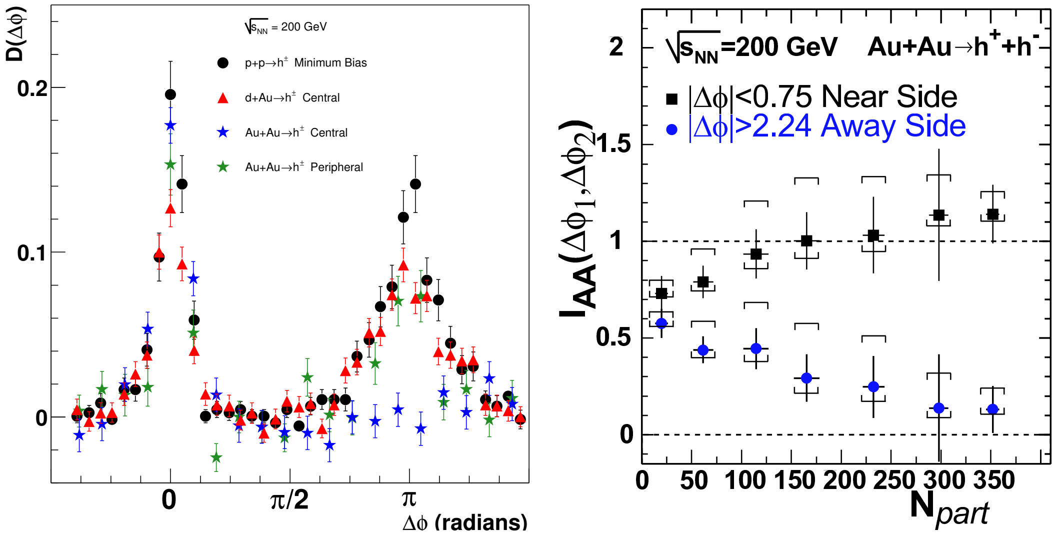

(a) (b)

Figure 5.14: High-$p_\perp$ azimuthal correlations (a) $D(\Delta\phi)$ (Equation 5.8) for background-subtracted p+p d+Au, and Au+Au collisions. Systematic uncertainty not shown for clarity. Data taken from [71, 72]. (b) Ratio of background-subtracted Au+Au over p+p for near-side and away-side azimuthal regions versus $\mathrm{N}_{\mathrm{part}}$. The horizontal bars indicate the dominant systematic error (highly correlated among points) due to the uncertainty in the background. Figure adapted from [70].

in Au+Au to the corresponding jet in p+p. With respect to p+p, the near-side jet gets larger with centrality while the away-side jet decreases with centrality.

From the $R_{AA}(p_\perp)$ studies, we know that there is a strong energy loss of high-$p_\perp$ particles in central Au+Au collisions. Hadronic energy loss models to date cannot explain the total suppression of the away side peak in central Au+Au collisions [73]. Partonic energy loss suggests a surface emission model. For example, in central Au+Au collisions, particles that are emitted near the surface of the dense medium escape without being suppressed, while their back-to-back partners must traverse the medium and consequently are suppressed. The centrality dependence of the suppression of the away-side jet and $R_{AA}(p_\perp)$ lends credence to this model.

5.5 Conclusions

This analysis presented the first measurement of the absolute cross section for charged hadron production from non-singly diffractive p+p collisions at $\sqrt{s} = 200$ GeV. Also presented from this collision system was the charged hadron $p_\perp$ spectra which extends to 50% greater $p_\perp$ than the only previous nucleon-nucleon (p+p̄) measurement at the same center-of-mass energy. Moreover, multiplicity and $\langle p_\perp \rangle$ of these p+p collisions were shown, revealing that the $\langle p_\perp \rangle$ and total event $p_\perp$ increase linearly with multiplicity. A similar analysis was performed on d+Au collisions at $\sqrt{s_{\rm NN}} = 200$ GeV from the same detector.

The measurement of the p+p, d+Au, and the previously measured Au+Au charged hadron spectra, in the same detector and at the same center of mass energy, allowed for a systematic study of nuclear effects with the nuclear modification factor $R_{AA}(p_\perp)$. It was shown that central Au+Au collisions do not behave as a superposition of many p+p collisions as the high-$p_\perp$ particle yield in Au+Au collisions is suppressed. It also was shown that the suppression disappears smoothly as one goes towards the most peripheral collisions. In contrast, the high-$p_\perp$ particle yield in central and minimum bias d+Au collisions exhibit a slight enhancement versus the yield in binary scaled p+p collisions. Of the three leading explanations: saturation, hadronic energy loss, and partonic energy loss, only partonic energy loss was able to mutually explain the system, centrality, and $p_\perp$ dependence of the nuclear modification factor. This model determined that the density of the medium produced in central Au+Au collisions must be at least 90 times greater than normal nuclear matter. According to lattice QCD calculations, this extreme density implies that the medium consists of deconfined quarks and gluons that are not bound into nucleons–a Quark Gluon Plasma.

5.6 Future Directions

This analysis alone, however, is not a definitive measurement of the Quark Gluon Plasma as extreme densities only imply a deconfined state of matter. Moreover, this analysis is not sensitive to whether the medium is thermalized. Thermodynamic models of particle production have been able to fit the particle production ratios in Au+Au collisions at $\sqrt{s_{\mathrm{NN}}} = 200$ GeV with a temperature of 177 MeV [74], which would imply a thermalized source that is above the critical temperature needed for a QGP. However, this only gives the temperature at chemical freeze-out which may not be the temperature of the source. One test to ascertain the temperature of the source would be to measure the direct photon spectrum. Unfortunately, the decays of particles into photons masks this signal and so far it has not been extracted.

On the other hand, there is a simpler test for deconfinement, the suppression of the J/Ψ meson. The J/Ψ is a bound state of a charm and anti-charm quark with a mass of 3.097 GeV/c^2. This large mass leads to a large binding radius. As charm quarks must be produced in correlated pairs, a deconfined medium with a bath of quarks would reduce the probability that a $c\bar{c}$ pair would be formed in favor of open charm [75]. Unfortunately, the J/Ψ production cross section at RHIC energies is 4 orders of magnitude lower than hadron production [76]. Therefore, higher statistics than previously recorded at RHIC are needed for a significant sample. For this reason, RHIC will have a long Au+Au run at $\sqrt{s_{\mathrm{NN}}} = 200$ GeV from 2003-2004. With the analysis of this data, the question of confinement should be answered.

This field is constantly evolving and being refined. The next generation accelerator, The Large Hadron Accelerator (LHC) located at CERN, will bring a plethora of new data into the field after its completion in 2008. The LHC promises a center of mass energy for Pb+Pb collisions of $\sqrt{s_{\mathrm{NN}}}= 5.5$ TeV. This experiment will be able to extend $R_{AA}(p_{\perp})$ to $p_{\perp}\approx 100$ GeV/c, which may better constrain the models presented in this thesis. With the turning on of this accelerator some questions may be answered and new ones may be produced. The data and the conclusions of this thesis are one piece of the larger puzzle that should help to determine the future landscape of nuclear physics and QCD at high energy density.

Appendix A

Coordinate Systems and Kinematics

A.1 Coordinate Systems

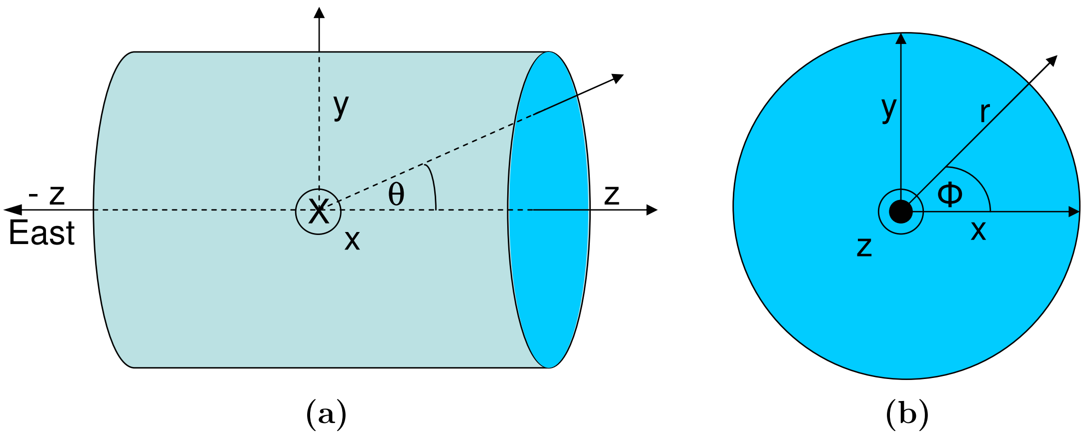

Figure A.1: STAR coordinate systems (a) side view (b) end view.

Most of the detector systems in STAR respect a cylindrical symmetry. Therefore the primary coordinate system utilized by STAR are cylindrical coordinates. The coordinate system is shown on a schematic diagram of the Time Projection Chamber (TPC) in Figure A.1. The direction labelled z runs longitudinally along the radial center TPC. Due to the orientation of the detector at Brookhaven National Laboratory, the negative z side of the TPC also is referred to as the East side and the positive z side is referred to as the West side. The radial or transverse direction is denoted by r. This can be decomposed into the x and y directions which are shown in Figure A.1(b).

$\theta°$	90	62.5	45	40.4	15.4	5.7	2.1	0.77
η	0	0.5	0.88	1	2	3	4	5

Table A.1: Conversions between polar angle θ and pseudorapidity η.

The angular directions used are Φ and θ. The azimuthal angle Φ in the right-handed angle in the xy plane from the x axis to the point. The polar angle θ is the right-handed angle in the yz plane from point to the y axis.

A.1.1 Kinematics

Rarely in heavy-ion or particle physics is the variable θ used. Instead a transformation to pseudorapidity η is performed as shown in Equation A.1. Table A.1 shows examples of the conversion between θ (in degrees) and η.

$$\eta = -\ln \tan(\frac{\theta}{2}) \tag{A.1}$$

The pseudorapidity variable is often used because it is very closely related to the rapidity, defined as:

$$y = \tanh \beta \; or \; y = -\frac{1}{2} \ln \frac{E + p_z}{E - P_z} = -\frac{1}{2} \ln \frac{1 + \frac{p_z c}{E}}{1 - \frac{p_z c}{E}} \tag{A.2}$$

As p_z = p $\cos\theta$, p = γmv, E = γmc^2, then

$$\frac{p}{E} = \frac{v}{c^2} = \frac{\beta}{c} \longrightarrow \frac{p_z}{E} = \frac{\beta}{c} \cos\theta \tag{A.3}$$

and substituting into A.2

$$y = -\frac{1}{2} \ln \frac{1 + \beta\cos\theta}{1 - \beta\cos\theta} \tag{A.4}$$

For a relativistic particle, m $\ll$ p, so $\beta \longrightarrow 1$,

$$y \longrightarrow \eta = -\frac{1}{2} \ln \frac{1 + \cos\theta}{1 - \cos\theta} = -\ln \tan \frac{\theta}{2} \tag{A.5}$$

This variable approximates rapidity and can be used without knowledge of the complete four-momentum.

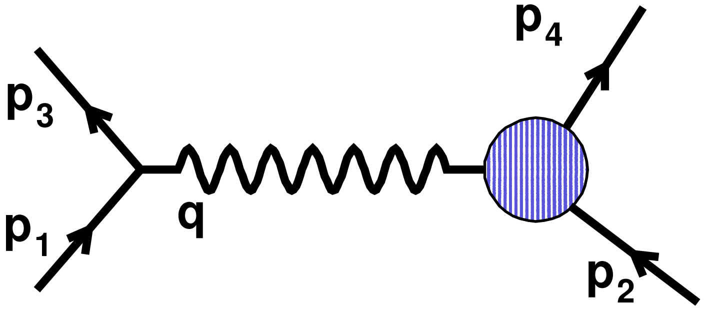

Figure A.2: Hard process kinematics.

Another frequently used variable to describe hard processes is the momentum transfer Q. Figure A.2 shows the Feynman diagram for electron-proton scattering. The cross section depends on $q \equiv (p_1 - p_3)$ with $Q^2 \equiv -q^2$. The quantity x = parton's momentum / nucleon's momentum can also be derived from the above figure. Taking the nucleon to have four-momentum p = (P,0,0,P) (with P $\gg$ m), and a constituent parton to have four-momentum xp = (xP,0,0,xP). If the constituent absorbs the photon, its final invariant mass will be

$$(xp + q)^2 = (xp)^2 - Q^2 + 2xp \cdot q. \tag{A.6}$$

The invariant mass squared of the parton $(yp)^2$ and $(yp+q)^2$ is small compared with Q^2 and $p \cdot q$, thus x = Q^2 / $2p \cdot q$.

Appendix B

Tracking

B.1 Track Finding

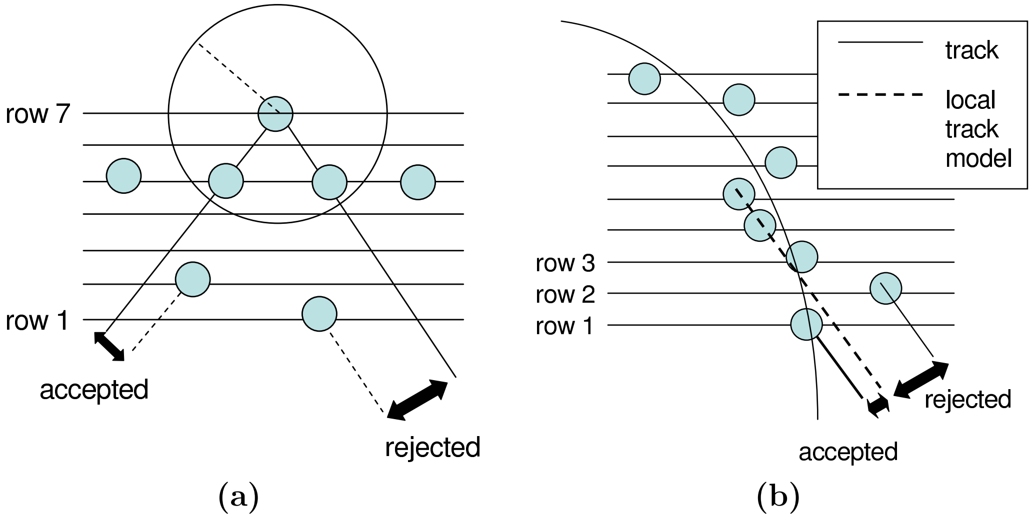

Figure B.1: (a) Finding a track root in the xy plane. (b) Finding a segment in the xy plane. Figures adapted from [77].

The tracking algorithm used in this production of the STAR data is based on an outside to inside method first developed for the ALEPH and NA35 experiments. The process starts at the outer-most row of the TPC where the track density is the lowest and the purest seed can be found. The algorithm first looks for any hit within a certain radius, then it associates other hits that lie near the line between the two. If three hits are found in a line, they are associated as a link. This is shown in Figure B.1(a) for the xy plane, but is also performed in the rz plane as well. Although this algorithm uses a linear track model instead of a helical track model (to be defined in

Appendix B.2), the approximation is valid over small distances.

The link is now extended by looking for any hits that also lie along the line defined by the 3 hits in the link as shown in Figure B.1(b). The dashed line is a linear fit to the root in rows 3,4 and 5. In this example the hit on row 1 would be accepted and the hit in row 2 would be rejected. The original link, plus any added points, is referred to as a segment. Since a segment can contain many hits over large distances, the linear approximation of the helix begins to breakdown. The segment, therefore, is fit to a helix and any outliers of the segment are removed. All of the points used in this final segment are marked and cannot be used again. The process then restarts at the beginning to form more roots from the unused hits.

After all the segments have been formed, starting with the largest to the smallest segment any hits that lie along the helix formed by the segment are added onto the track and removed from the available hits. Next, helixes that overlap in space and have similar curvature are merged together as they most likely were produced by the same particle.

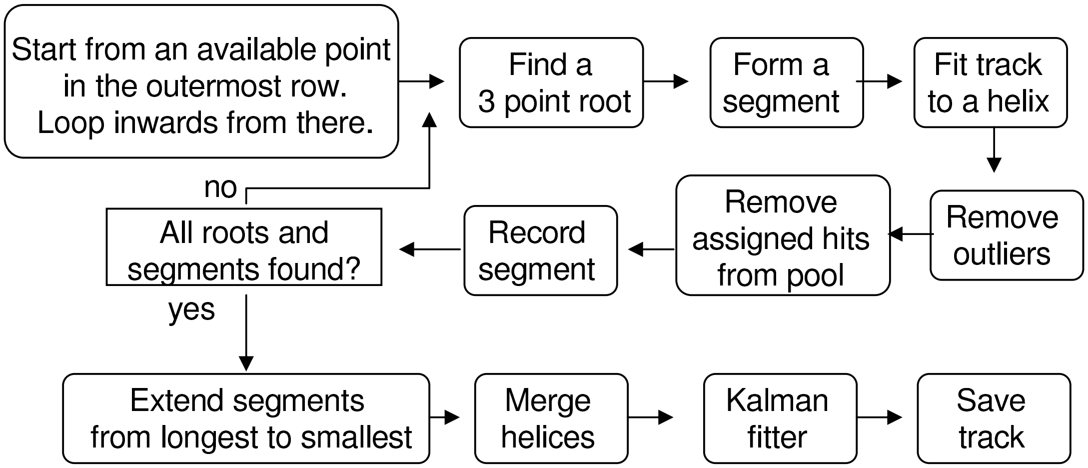

Figure B.2: Tracking algorithm flow chart. Adapted from [77].

The final step is to take the output of the track finder and run it through a Kalman fitter to account for energy loss [78]. The track passes through material as it radially traverses the detectors and thus loses energy. This energy loss causes the helix returned by the track finder to have a systematically lower momentum than the actual track would have if it had been in a vacuum. The Kalman fitter removes hits that do not match a helix model that is adjusted for energy loss. The Kalman fitter also adjusts the momentum of the track to reflect the true momentum at the origin rather than the best helix fit. The current version of the Kalman fitter does not add on new points, but this feature will be implemented in a software overhaul slated in the coming year [79].

The aforementioned tracking model, called global tracking, is used in this analysis. An extension of this model, called primary tracking, also can be used. In this model, the global tracks are found as normal but the vertex of the collision is added on as a highly weighted hit. In fact, any track's helix that passes within 3 cm of the event vertex is forced to go through the vertex in this model. When the vertexing is accurate, as in high multiplicity Au+Au events, the vertex refit improves the accuracy of the momentum determination [19, 28, 36]. However, when the vertex position is not well defined as in low multiplicity p+p events, the vertex refit may have erratic behavior. Therefore, this analysis does not use these vertex refit tracks.

B.2 Helix Parametrization

Without external constraints, particles emerging from a collision will follow the path of a straight line. However, under the influence of a static magnetic field in one direction, for example $\vec{B} = (0, 0, B_z)$, the paths will be helical instead of straight. A helix is basically a circular path that does not close upon itself because it is stretched out like a coiled spring. The equations for a helix in cartesian coordinates x, y and z are expressed as functions of the track length s, the distance along the helix from the starting point,

$$x(s) = x_0 + \frac{1}{\kappa}[\cos(\Phi_0 + h\ s\ \kappa\ \cos\lambda) - \cos\Phi_0] \tag{B.1}$$

$$y(s) = y_0 + \frac{1}{\kappa}[\sin(\Phi_0 + h\ s\ \kappa\ \cos\lambda) - \sin\Phi_0] \tag{B.2}$$

$$z(s) = z_0 + s\ \sin\lambda \tag{B.3}$$

where x_0, y_0, z_0 is the first point of the helix, λ is the dip angle or slope, κ is the curvature or the reciprocal of the radius ($\kappa = 1/\mathrm{R}$), h is the sense of rotation of the helix in the xy plane, and Φ_0 is the azimuthal angle of the track direction at the first point of the helix.

Although these functions directly can be fit to the found tracks, it is more efficient to use the spring-like geometry to simplify the procedure. One can fit the helix in the xy plane with a circle:

$$1/\kappa^2 = (x - x_c)^2 + (y - y_c)^2 \tag{B.4}$$

The dip angle can be found by fitting the helix in the projection of the zs plane. Figure B.3 schematically shows the fits in the two planes.

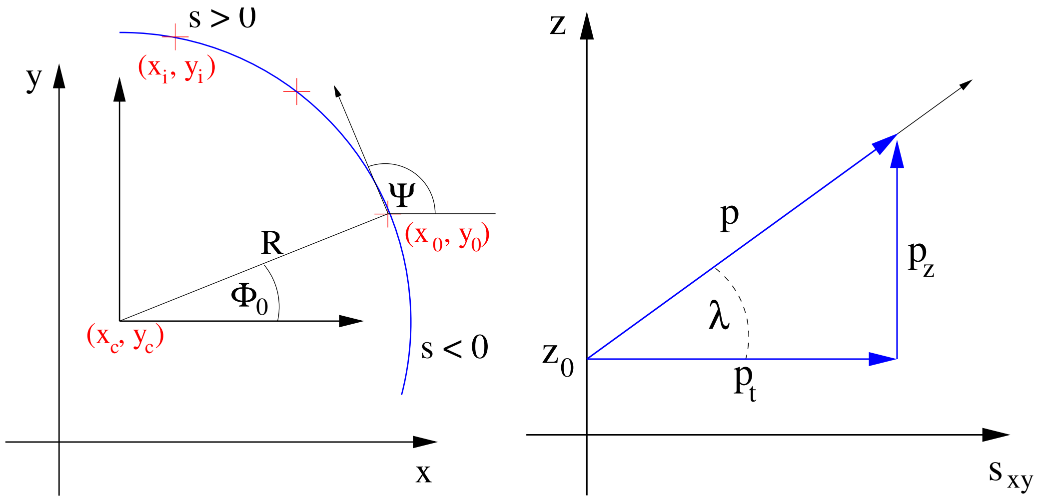

(a) (b)

Figure B.3: Projection of a helix on the (a) xy plane (b) sz plane. Figures taken from [80].

From these fits, the track's parameters can be extracted as:

$$p_\perp = c\, q\, B/\kappa \tag{B.5}$$

$$p_z = p_\perp \tan\lambda \tag{B.6}$$

$$p = \sqrt{p_\perp^2 + p_z^2} \tag{B.7}$$

where κ is the curvature in m^{-1}, B the value of the magnetic field in Tesla, q is the change of the particle in units of electric charge, c the speed of light in m/ns and $p_\perp$ and p_z are the transverse and longitudinal momentum in GeV/c. For a more comprehensive discussion of the helix parameterizations and the computing tools used to perform these fits see References [77, 80].

B.3 Projecting Helixes

The STAR TPC only records hits within $50 < r < 200$ cm. If one requires the track location outside this window, the helix must be projected mathematically. In this analysis, one often wants to calculate the intersection or distance of closest approach (DCA) of a track and a certain geometrical construct. For example, to determine if a track matches a hit CTB slat, the track must be projected to a cylinder surrounding the TPC. To determine if a track matches the beamline, the DCA of the helix to a line near the center of the TPC must be calculated.

In the case of the projection of a helix to the cylinder, an analytic solution of the equation $\rho^2 = x(s)^2 + y(s)^2$ is found by substituting in Equations B.1 and B.2 and solving for s. The case of the helix to beamline match is a more difficult because it is not purely analytic. There is no efficient code available to match a helix to a line, but the code does exist to find the intersection of two helixes. One can mimic a straight line by creating a helix with a small curvature. To find the intersection of two helixes, the intersection of two circles is calculated in the xy plane from the law of cosines. Then an iterative approach is used to find the intersection of the helixes in the other plane. More on these methods can be found in Reference [80].

Appendix C

Fitting Techniques

When fitting a function to a histogram, certain considerations must be made. If the histogram has infinitely small bins, thus infinite statistics, it can be fit with normal Minuit techniques [81]. However, if the statistics are low, one usually increases the bin size to get a larger sample. As the bin size gets large it is not sufficient to treat the histogram as a collection of points with the x position at the center of the bin and the y position at the bin's content [82].

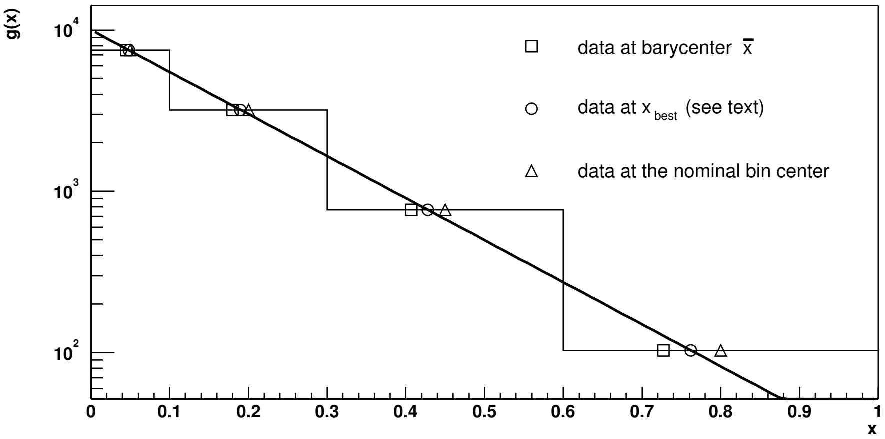

Figure C.1: The function $g(x) = 10^4 \times e^{-6x}$ with three sets of points showing different possible choices for choosing correct bin centers. Figure adapted from [82].

When using a steeply falling fit function, such as an exponential, in a given bin more counts actually would have occurred to the left of the bin center than to the right. Figure C.1 shows the histogram found by sampling the exponential function $g(x) = 10^4 \times e^{-6x}$ along with $g(x)$ itself. The triangles are plotted at the value of the nominal bin centers. One can see that the triangles systematically overestimate $g(x)$.

The squares represent the barycenter, or center-of-gravity, of the bin. This is found by:

$$\overline{x} = \frac{\int_{x_1}^{x_2} x\ g(x)\ dx}{\int_{x_1}^{x_2} g(x)\ dx} \tag{C.1}$$

The squares always underestimate the value of the $g(x)$. Therefore, neither of the methods should be used when fitting the data. As shown in Figure C.1, the differences between the choices of bin centers gets larger at larger x.

The third and correct method is to place the x position of the data point "...where the value of the predicted function is equal to the mean value over the wide bin" [82]. This is mathematically described as:

$$g(x_{best}) = \frac{1}{x_2 - x_1} \int_{x_1}^{x_2} g(x)\ dx. \tag{C.2}$$

This forces the bin center to lie along the predicted function, which removes the systematic offset of which the other two methods suffer. The circles on Figure C.1 are placed at this correct position. One sees they more accurately describe the generating function.

In the above example the predicted fit function was known *a priori*. In a real world example such as the spectra analysis of Section 4.2, the true generating function is unknown. Therefore an iterative procedure must be used. The data is first fit with the function using the nominal bin centers and the results of the fit is used as $g(x)$. The new bin centers are then found and used for a second iteration. For the spectra analysis, the cycle converges by the second interaction. If the spectra went out farther in $p_\perp$, additional iterations would be needed.

In the spectra analysis, a pQCD inspired powerlaw is used to fit the data shown in Figure 4.2. The form of the powerlaw is:

$$g(p_\perp) = A(1 + p_\perp/p_0)^{-n}. \tag{C.3}$$

To find x_{best}, one solves Equation C.2 with a the powerlaw substituted for $g(x)$:

$$\begin{aligned} A(1 + x_{best}/p_0)^{-n} &= \frac{A}{x_2 - x_1} \int_{x_1}^{x_2} (1 + x/p_0)^{-n}\ dx && \text{(C.4)} \\ x_{best} &= p_0 \left(\frac{(x_1 + p_0)(\frac{x_1 + p_0}{p_0})^{-n} - (x_2 + p_0)(\frac{x_2 + p_0}{p_0})^{-n}}{(n-1)(x_2 - x_1)} \right)^{-\frac{1}{n}} - p_0. && \text{(C.5)} \end{aligned}$$

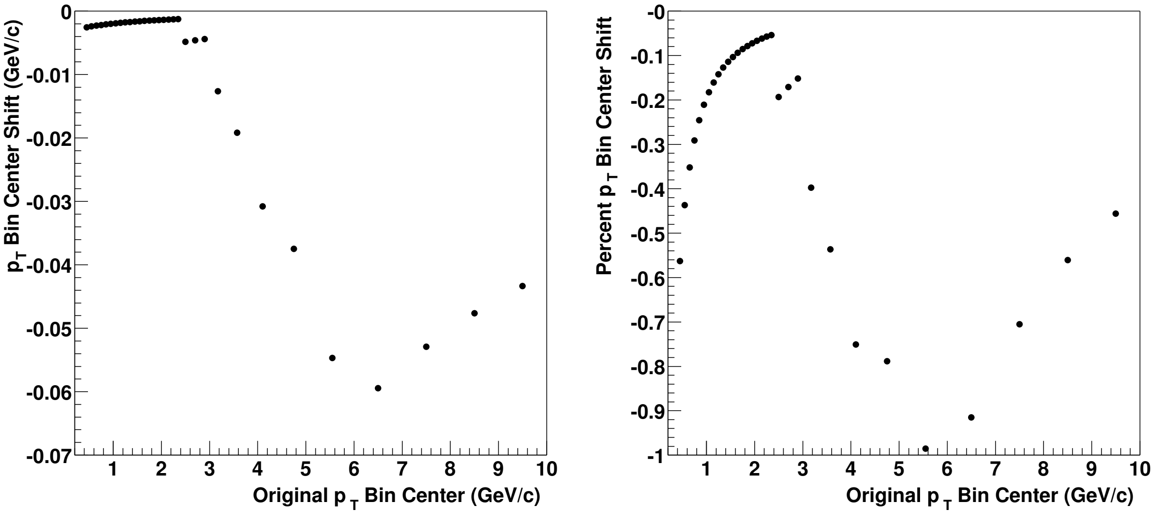

(a) **(b)**

Figure C.2: (a) Absolute shift in the bin center versus $p_\perp$ in GeV/c. (b) Percentage bin shift versus $p_\perp$.

For the data in Figure 4.2, the bins have already been moved by this method. Figure C.2 gives absolute and relative shift from the nominal bin center versus the nominal bin center. This is maximally a 1% effect, but it still should be taken into account because it makes a large difference in the fit parameters. Table C.1 summarizes the fit parameters using both the old and new bin centers.

	Amplitude	p_0	n	χ^2 / ndf
Nominal Bin Centers	339 ± 31	1.35 ± .062	10.15 ± 0.20	10.99 / 29
Adjusted Bin Centers	331 ± 30	1.39 ± 0.064	10.30 ± 0.21	10.31 / 29

Table C.1: Power law fit parameters for different $p_\perp$ binnings.

Appendix D

Pileup Rates

To determine the pileup rate, one must know the number of minimum bias collisions occurring per second f_{ND}, which is given by:

$$f_{ND} = \mathcal{L} \times \sigma_{ND} \tag{D.1}$$

where $\mathcal{L}$ is the luminosity of the beams and σ_{ND} is the total non-diffractive cross section.

As the TPC takes 40 μs to drift, a single TPC event can have information from 40 μs before and 40 μs after the trigger. Therefore, the number of events per TPC frame is:

$$\text{Events per TPC Frame} = f_{ND} \times 80\mu s. \tag{D.2}$$

This quantity plotted versus time is shown in Figure D.1. The right vertical axis gives the number of events per TPC frame averaged over the entire day of active running. This quantity is plotted versus time because the luminosity is changing. It is changing on the long time scale because the accelerator operators were able to extract better performance with experience. The maximum value is approximately 1.6 events per TPC frame.

To determine the probability of a bunch crossing producing an event, one multiplies the minimum bias collision rate, f_{ND}, by the time between each bunch crossing, 213 ns. The left vertical axis of Figure D.1 gives this probability, and it has a maximum value of 0.5%.

The pileup rates and probabilities also change with time on the short time scale, because the luminosity of the beam decreases over the duration of one accelerator fill due to beam losses. Figure D.2 shows this decrease for the accelerator fills on day 13 of the run. From the figures, one can see the average value over the course of the

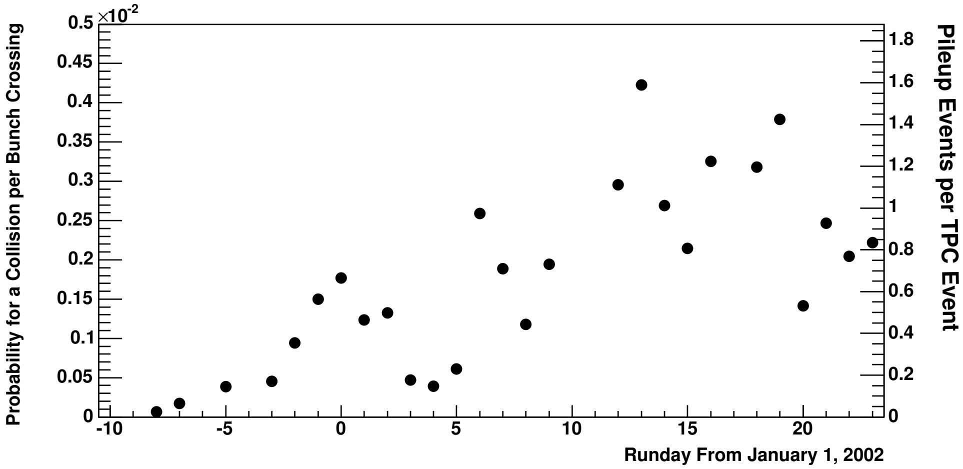

Figure D.1: Pileup rates versus day of run. Left vertical axis is the probability that a bunch crossing results in a p+p minimum bias collision. The right vertical axis is the average number of pileup events that occur ±40 μs from the trigger.

day is slightly less than the average of the minimum and maximum values due to the exponential nature of the decay.

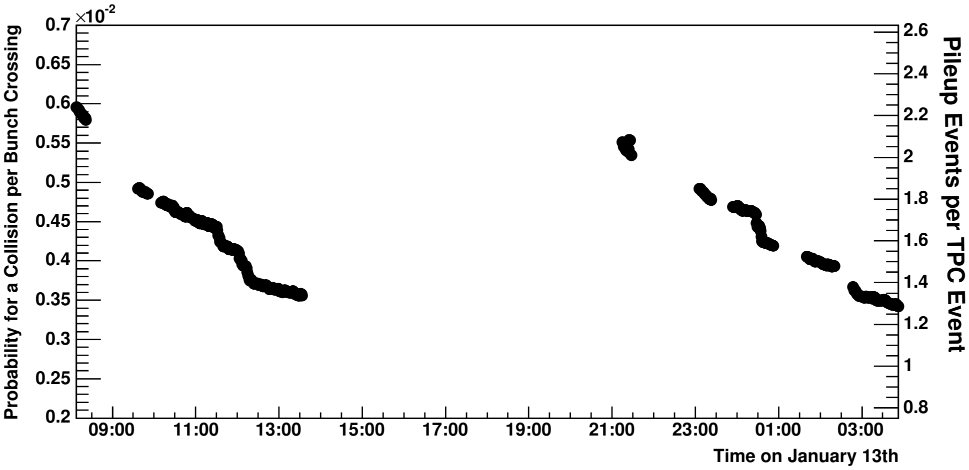

Figure D.2: Pileup rates versus time on Day 13. Left vertical axis is the probability that a bunch crossing results in a p+p minimum bias collision. The right vertical axis is the average number of pileup events that occur ±40 μs from the trigger. The gaps are are due to STAR downtime. The large gap in the middle is due to the beams being refilled.

Appendix E

Nuclear Geometry and Centrality Selection

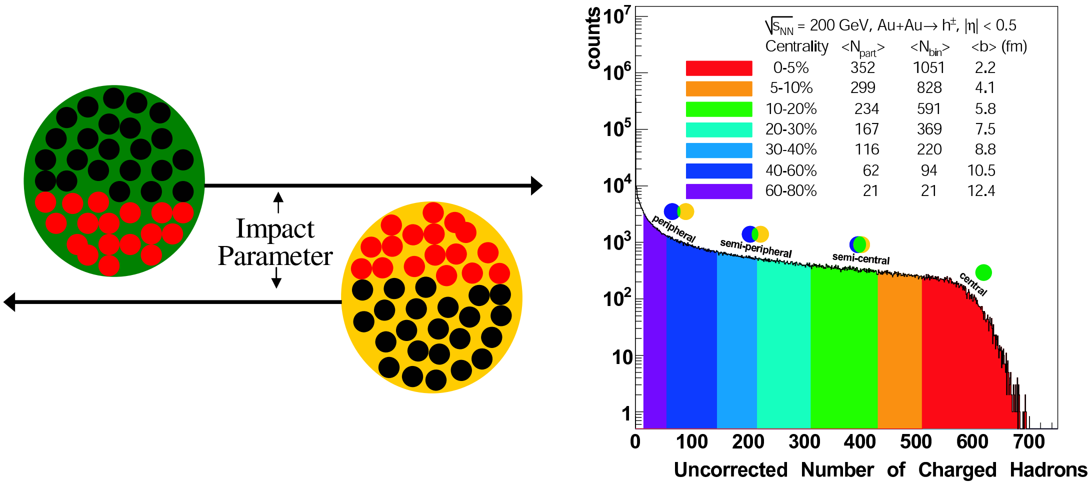

(a) **(b)**

Figure E.1: (a) Illustration of the nuclear collision geometry. Red circles represent participating nucleons and black circles represent spectators. (b) Illustration of the mapping between multiplicity in Au+Au collisions and centrality.

One can approximate of the complex dynamics of heavy-ion collisions as a superposition of many nucleon-nucleon collisions. The number of interacting nucleons depends on the impact parameter, b, of the two nuclei as illustrated in Figure E.1(a). In this illustration, the red nucleons will interact while the black nucleons are spectators and continue to travel at beam rapidity. Commonly, two quantities are used to quantify the level of superposition: the number of participants, N_{part} and the number of binary collisions, N_{bin}. In a perfectly central Au(197)+Au(197) where every nucleon interacts with every other, $N_{\mathrm{part}}=2\times197$ and $N_{\mathrm{bin}}= 197^2$. As it is impossible to measure directly these quantities in experiment, experimental results are compared to model calculations to extract these quantities. Figure E.1(b) shows the mapping between the measured charged hadron multiplicity in Au+Au collisions and the above quantities.

The colloquially named Glauber models [83] are used to determine the level of superposition. In this formalism, all nucleons are assumed to have a constant interaction cross section and follow straight line trajectories even after interaction. The STAR experiment uses a Monte-Carlo Glauber implementation. In this technique, A nucleons are distributed in a nucleus by realistic probability distribution. For Au nuclei, the Woods-Saxon probability distribution is used [84], while the Hulthén form [85, 86] is used for deuterons. Two such nuclei are generated with a transverse offset of b. If the transverse areas (given by the inelastic n-n cross section $\sigma_{in} = 42mb$) of two nucleons overlap, the nucleons are said to interact. The longitudinal component is not needed because of the assumption that all nucleons travel in straight lines. This assumption also prohibits intra-nucleus collisions. Statistical models are used to produce the multiplicity distributions which are then correlated to the measured multiplicity distribution. This produces a mapping between multiplicity and N_{bin} and N_{part} which can be used to categorize centrality classes. For an in depth review of Glauber models see [70].

Centrality(%)	$\langle \mathrm{N_{part}} \rangle$	$\mathrm{N_{bin}}$	$\langle b \rangle$
0-100	$102.0^{+0.9}_{-1.7}$	$235.8^{+13.0}_{-16.0}$	$9.9^{+0.2}_{-0.5}$
0-10	$325.8^{+5.4}_{-5.3}$	$940.0^{+66.9}_{-69.5}$	$3.1^{+0.1}_{-0.1}$
0-5	$352.4^{+3.4}_{-4.0}$	$1051.3^{+71.5}_{-71.1}$	$2.2^{+0.2}_{-0.1}$
5-10	$299.3^{+6.6}_{-6.7}$	$827.9^{+63.8}_{-66.7}$	$4.1^{+0.2}_{-0.2}$
10-20	$234.6^{+8.3}_{-9.3}$	$591.3^{+51.9}_{-59.9}$	$5.8^{+0.2}_{-0.3}$
20-30	$166.7^{+9.0}_{-10.6}$	$368.6^{+41.1}_{-50.6}$	$7.5^{+0.3}_{-0.3}$
30-40	$115.5^{+8.7}_{-11.2}$	$220.2^{+30.0}_{-38.3}$	$8.8^{+0.4}_{-0.4}$
40-50	$76.6^{+8.5}_{-10.4}$	$123.4^{+22.7}_{-27.3}$	$10.0^{+0.4}_{-0.5}$
50-60	$47.8^{+7.6}_{-9.5}$	$63.9^{+14.1}_{-18.9}$	$11.1^{+0.6}_{-0.6}$
60-70	$27.4^{+5.4}_{-7.5}$	$29.5^{+8.2}_{-11.3}$	$12.0^{+0.7}_{-0.6}$
70-80	$14.1^{+3.6}_{-5.0}$	$12.3^{+4.4}_{-5.2}$	$12.9^{+0.7}_{-0.6}$
80-100	$4.5^{+1.1}_{-1.3}$	$3.1^{+1.0}_{-0.9}$	$14.3^{+0.6}_{-0.8}$
20-40	$141.4^{+9.1}_{-11.3}$	$294.2^{+34.8}_{-45.2}$	$8.1^{+0.3}_{-0.4}$
40-60	$62.4^{+8.3}_{-10.4}$	$93.6^{+17.5}_{-23.4}$	$10.5^{+0.6}_{-0.5}$
60-80	$20.9^{+5.1}_{-6.5}$	$21.2^{+6.6}_{-7.9}$	$12.4^{+0.8}_{-0.6}$
5-20	$256.1^{+7.1}_{-8.0}$	$669.8^{+56.5}_{-61.8}$	$5.2^{+0.2}_{-0.3}$
30-50	$95.8^{+8.6}_{-10.2}$	$171.9^{+26.7}_{-32.3}$	$9.4^{+0.4}_{-0.4}$
50-80	$29.7^{+5.8}_{-7.3}$	$35.3^{+9.2}_{-10.9}$	$12.0^{+0.6}_{-0.6}$

Table E.1: Centrality, $\langle \mathrm{N_{part}} \rangle$, $\langle \mathrm{N_{bin}} \rangle$ and $\langle b \rangle$ for Au+Au collisions at $\sqrt{s_{\rm NN}} = 200$ GeV from Monte Carlo Glauber. Tables taken from [70].

Centrality(%)	$\langle \mathrm{N_{part}} \rangle$	$\mathrm{N_{bin}}$	$\langle b \rangle$
0-20 Cut on N_{coll}	$16.3^{+1.1}_{-0.4}$	$16.5^{+0.4}_{-1.0}$	$2.5^{+0.2}_{-0.1}$
20-40 Cut on N_{coll}	$10.4^{+0.5}_{-0.0}$	$9.9^{+0.0}_{-1.0}$	$4.6^{+0.2}_{-0.2}$
40-100 Cut on N_{coll}	$4.3^{+0.0}_{-0.1}$	$3.2^{+0.0}_{-0.5}$	$7.3^{+0.2}_{-0.4}$
0-100 Cut on N_{coll}	$8.3^{+0.3}_{-0.4}$	$7.5^{+0.4}_{-0.4}$	$5.8^{+0.1}_{-0.3}$
$N_{part}^{deuteron} == 2$	$11.0^{+0.4}_{-0.5}$	$10.3^{+0.5}_{-0.5}$	$4.6^{+0.1}_{-0.1}$
$N_{npart}^{deuteron} == 1$	$3.9^{+0.1}_{-0.2}$	$2.9^{+0.1}_{-0.2}$	$7.6^{+0.2}_{-0.2}$
0-20 Cut on FTPCE	NA	$15.0^{+1.1}_{-1.1}$	NA
20-40 Cut on FTPCE	NA	$10.2^{+1.0}_{-0.8}$	NA
40-100 Cut on FTPCE	NA	$4.0^{+0.3}_{-0.3}$	NA
0-100 Cut on FTPCE	NA	$7.5^{+0.4}_{-0.4}$	NA

Table E.2: Centrality, $\langle \mathrm{N_{part}} \rangle$, $\langle \mathrm{N_{bin}} \rangle$ and $\langle b \rangle$ for d+Au collisions at $\sqrt{s_{\rm NN}} = 200$ GeV from Monte Carlo Glauber. Tables taken from [70].

Appendix F

d+Au Analysis and Results

A similar analysis based on the meanZ vertex finding method was performed on the d+Au collisions recorded in the STAR detector. As will be shown, the multiplicities are higher which leads to an improved vertex efficiency compared to p+p collisions. Therefore, both the standard model of vertex finding and the meanZ method can be used to analyze the data. Although the analysis using the standard method of vertex finding was published, comparison to the meanZ method was used as an independent cross check to the minimum bias data as described in [71]. As the meanZ method can better describe the low multiplicity end of the distribution, it will be used when studying observables as a function of multiplicity.

F.1 d+Au Trigger

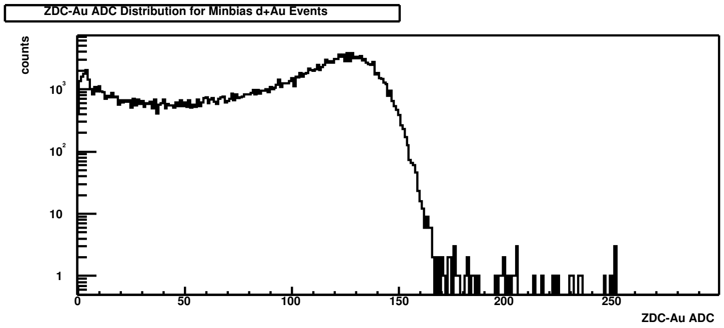

Figure F.1: ZDC-Au ADC distribution for d+Au minimum bias events.

A different trigger is used for d+Au running than p+p as the multiplicities are much higher in d+Au and they would swamp the Beam Beam Counters (BBC) and lead to very high trigger contamination. Instead, the Zero Degree Calorimeter (ZDC), discussed in Section 2.2.1, is used. The minimum bias trigger used for d+Au collisions is a single-arm trigger that required at least one beam-rapidity neutron in the ZDC which lies in the fragmentation region of the Au ions (assigned negative pseudorapidity) as described in Appendix A. The ZDC-Au distribution is shown in Figure F.1. The single neutron peek can be seen at an ADC value of 5. The trigger only recorded events where the ADC is greater 5 which is taken as the lower edge of the single neutron peak.

F.1.1 Trigger Efficiency

Instead of using a simulation to determine the ZDC trigger efficiency, a comparison to the BBC trigger was used. Since the BBC is very sensitive due to its larger phase-space coverage than the ZDC, if a BBC coincidence registers without a nuetron in the ZDC-Au, that the trigger is considered inefficient. It was found that the ZDC-Au trigger misses 3% of the cross-section seen by the BBC after background subtraction. 1% of the BBC triggers have a ZDC-d signal, but no ZDC-Au trigger, while 2% do not have a signal in either ZDC. Since the ZDC is sensitive only to neutrons, the 1% in the ZDC-Au is doubled to account for the fact that the proton, and not the neutron, is the spectator. An extra 1% was added for higher order affects and the final d+Au trigger efficiency is taken to be 95 ± 3% which is used to correct the final spectra.

F.1.2 Trigger Contamination

As with p+p collisions, there is some contamination of the trigger due to upstream beam-gas collisions. The contamination is larger in the d+Au trigger as it is a single-arm trigger that does not require a coincidence of two independent detectors. The trigger contamination is evaluated using abort-gap events as described in Section 3.6.3. For the d+Au analysis a cut was placed at Signal Fraction - $2\sigma < 0.5$. Of the 620 runs, 500 runs were accepted. The 120 rejected runs were mostly low-statistic runs leading to a large σ. Figure F.2(a) shows the signal fraction for accepted runs versus time. The weighted average of the accepted runs in shown in Figure F.2(b)

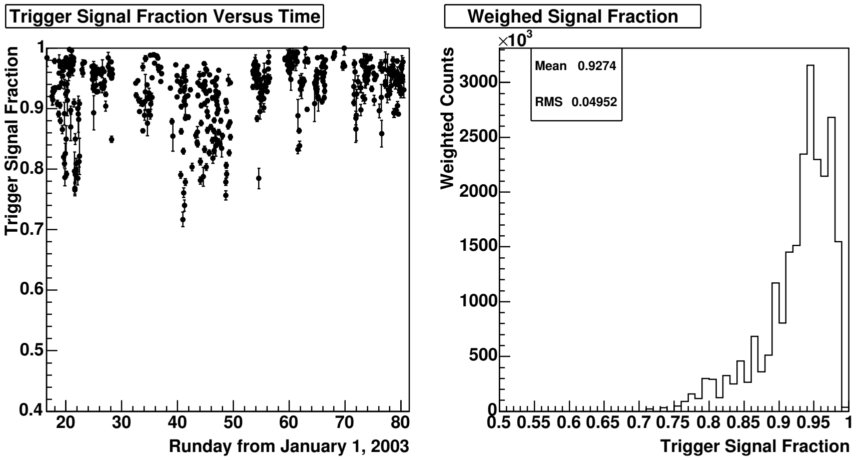

(a) (b)

Figure F.2: (a) Trigger signal fractions versus time. (b) 1 dimensional projection Of accepted runs weighted by the number of triggers.

and the value is 92 ± 5% which is used to correct the final spectra.

F.2 d+Au Vertex Resolution

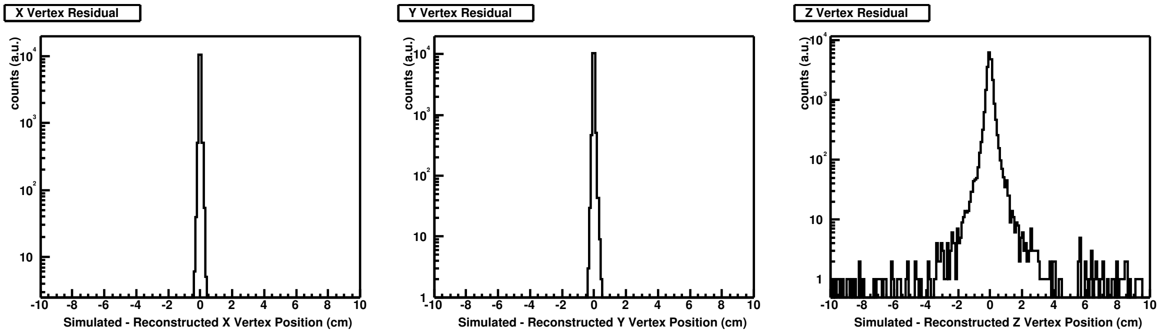

(a) (b) (c)

Figure F.3: d+Au vertex finding resolution in the (a) transverse X direction (c) transverse Y direction (d) longitudinal Z direction.

The vertex resolution for d+Au collisions is quantified by a similer method as in p+p collisions. One takes zerobias events during the d+Au run and injects a full HIJING simulation of a d+Au event. The vertex resolution is shown in Figure F.3

for the transverse and longitudinal directions.

Figure F.4(a) shows the input multiplicity distribution, and Figures F.4(b-d) shown the vertex efficiency, contamination and failure respectively. Although the multiplicity dependence is similar to p+p collisions, a larger cross-section of events occur at higher multiplicity, thus increasing the integrated efficiency. The intergraded vertex efficiency in d+Au is 93±1%, while the contamination is 4±1% and the failure is 3±1%.

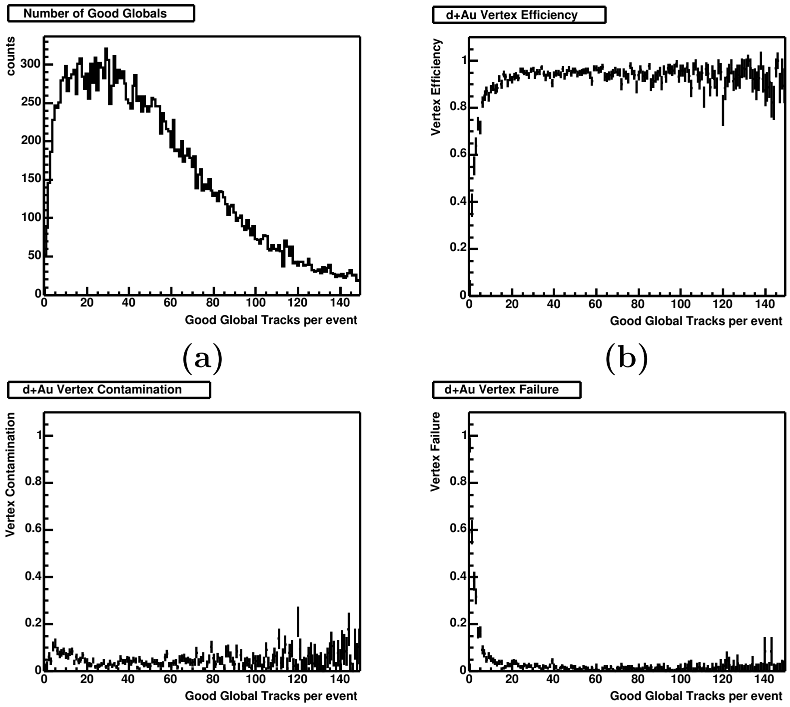

(a) (b)

(a) (b)

Figure F.4: (a) d+Au simulated input multiplicity (b) d+Au vertex finding efficiency (c) d+Au vertex finding contamination (d) d+Au vertex finding failure.

F.3 d+Au Minimum Bias Spectra

The fully corrected d+Au minimum bias charged hadron spectra from the meanZ method is shown in Figure F.5 along with the published spectra from the standard

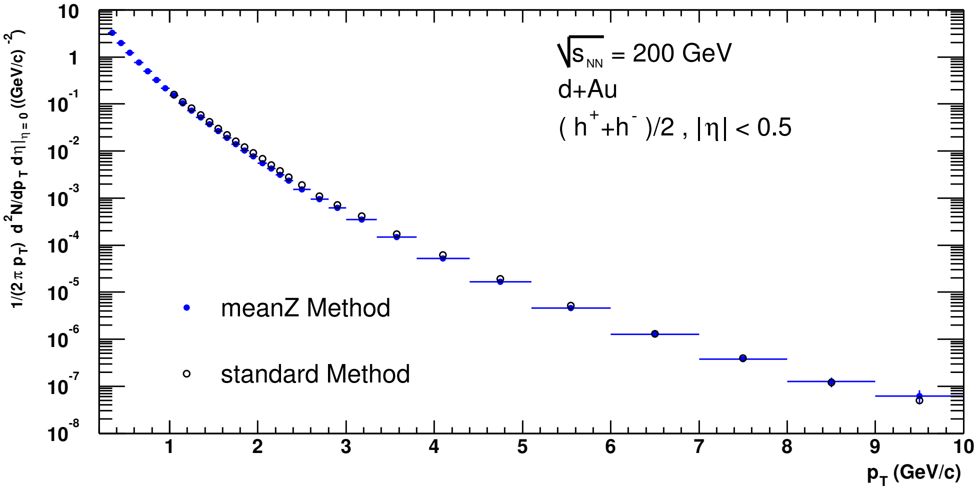

Figure F.5: d+Au inclusive charged hadron $p_\perp$ spectra at $\sqrt{s_{\rm NN}} = 200$ GeV from both the standard and meanZ method of vertex finding.

vertexing method [71]. The spectra agree within the 15% relative normalization uncertainty.

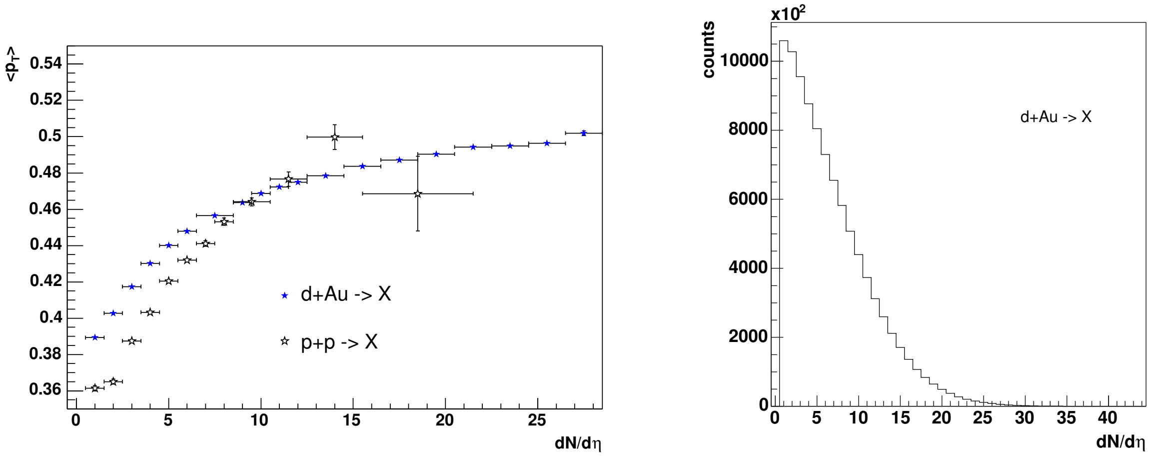

(a) (b)

Figure F.6: (a) d+Au $\langle p_\perp \rangle$ versus multiplicity (b) d+Au uncorrected multiplicity distribution.

The above spectra can be fit with a power law function as discussed in Section 4.2.1 to extract the $\langle p_\perp \rangle$. The value found is $\langle p_\perp \rangle = 0.449 \pm .001$ GeV/c. Furthermore, the spectra can be broken down into multiplicity bins to determine the dependence on $\langle p_\perp \rangle$ versus multiplicity. This is shown in Figure F.6(a) along with the data from p+p collisions from Section 4.2.3. There is a scaling of $\langle p_\perp \rangle$ with multiplicity in d+Au collisions as well as in p+p collisions. As the raw multiplicity is larger in d+Au collisions, as shown in Figure F.6(b), the measurement can go to larger multiplicity. There also appears to be a saturation of the scaling at $\frac{dN}{d\eta}$ greater than 25.

F.4 d+Au Central Data

In addition to the minimum bias data set, a high centrality data set was also used. Centrality tagging is based on the uncorrected charged particle multiplicity within $-3.8 > \eta > -2.8$, measured by the Forward Time Projection Chamber (FTPC) that lies in the fragmentation region of the Au beam. See Section 2.2.2 for a description of the FTPC. The FTPC-Au multiplicity was examined in quadrants relative to the orientation of the leading charged hadron at mid-rapidity to remove autocorrelation effects.

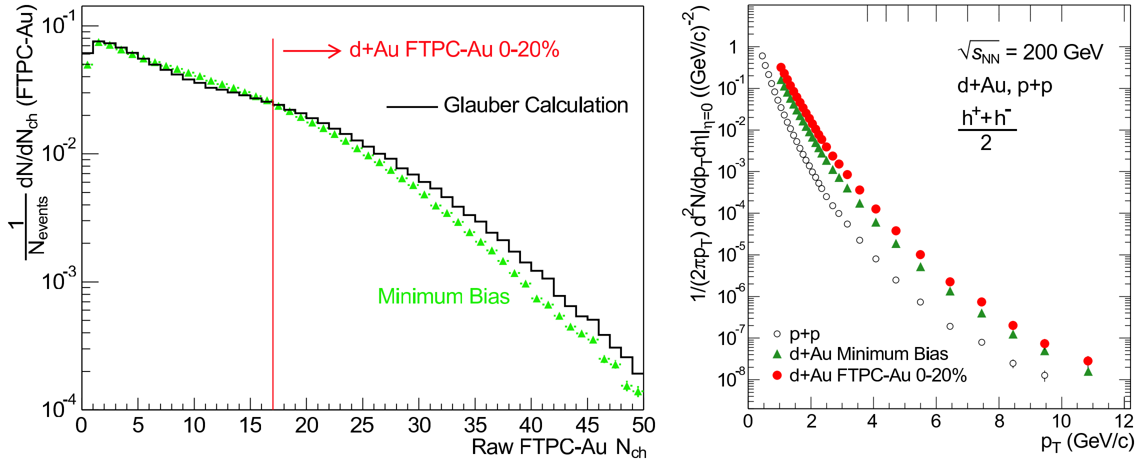

(a) **(b)**

Figure F.7: (a) d+Au centrality selection. Points are the multiplicity distribution from data, histogram is the Monte Carlo model. Events right of the red line are defined as the 20% most central data set. (b) Inclusive $p_\perp$ distributions for minimum bias and central d+Au collisions, and non-singly diffractive p+p collisions.

The centrality tags are modelled using a Monte Carlo Glauber calculation as described in Appendix E. In this model the mean number of binary collisions $\langle \mathrm{N_{bin}} \rangle$ is 7.5±0.4 for minimum bias events and σ_{hadr}^{dAu}=2.21±0.09 b. The FTPC-Au multiplicity distribution is modelled by convoluting the Glauber model distribution of participants from the Au nucleus with the charged multiplicity distribution measured in $2.5 < \eta < 3.5$ for p+p̄ collisions at $\sqrt{s}$=200 GeV [45]. The FTPC-Au acceptance, efficiency and backgrounds were taken into account using HIJING [31] events in a GEANT model [32] of the detector. Figure F.7 shows the measurements for minimum bias events with the corresponding Glauber model prediction. High FTPC-Au multiplicity therefore biases towards central collisions. Figure F.7(a) shows the cut defining the 20% highest multiplicity collisions in the data. $\langle \mathrm{N_{bin}} \rangle$=15.0±1.1 for the 20% highest multiplicity collisions in the Glauber model. The spectra from both minimum bias and central collisions is plotted along with the data from p+p collisions in Figure F.7(b). Comparisons to p+p collisions are made in Section 5.3.

Appendix G

Data Tables

The data of this thesis can be found at http://www.star.bnl.gov as well as in References [47, 71] where they previously have been published.

The p+p inclusive charged hadron spectra is shown in Table G.1. The measured p+p NSD cross-section is 31.1 mb ± 3.7 mb. Both the inelastic and NSD differential yields quoted below for the p+p data should be multiplied by this factor to produce differential cross-sections. The quoted uncertainty is the sum of the statistical and systematic uncertainty.

The d+Au inclusive charged hadron spectra is shown in Table G.2

p+p $p_\perp$(low,high) [GeV/c]	$\frac{1}{2\pi p_\perp}\, d^2N/dp_\perp d\eta\|_{\eta=0}(GeV/c)^{-2}$ NSD	Inelastic
0.45 (0.40,0.50)	0.58±0.04	0.62±0.04
0.55 (0.50,0.60)	0.35±0.02	0.36±0.02
0.65 (0.60,0.70)	0.21±0.01	0.22±0.01
0.75 (0.70,0.80)	0.13±0.01	0.13±0.01
0.85 (0.80,0.90)	0.079±0.004	0.082±0.005
0.95 (0.90,1.00)	0.051±0.003	0.052±0.003
1.05 (1.00,1.10)	0.033±0.002	0.034±0.002
1.15 (1.10,1.20)	0.022±0.001	0.022±0.001
1.25 (1.20,1.30)	0.015±0.001	0.015±0.001
1.35 (1.30,1.40)	0.010±0.001	0.010±0.001
1.45 (1.40,1.50)	0.0072±0.0004	0.0072±0.0004
1.55 (1.50,1.60)	0.0051±0.0003	0.0051±0.0003
1.65 (1.60,1.70)	0.0035±0.0003	0.0035±0.0003

p+p $p_\perp$(low,high) [GeV/c]	$\frac{1}{2\pi p_\perp} d^2N/dp_\perp d\eta\|_{\eta=0}(GeV/c)^{-2}$ NSD	Inelastic
1.75 (1.70,1.80)	0.0025±0.0002	0.0025±0.0002
1.85 (1.80,1.90)	0.0018±0.0001	0.0018±0.0001
1.95 (1.90,2.0)	0.0013±0.0001	0.0013±0.0001
2.05 (2.00,1.10)	0.00094±0.00009	0.00094±0.00009
2.15 (2.10,2.20)	0.00070±0.00007	0.00070±0.00007
2.25 (2.20,2.30)	0.00051±0.00006	0.00051±0.00006
2.35 (2.30,2.40)	0.00038±0.00004	0.00038±0.00004
2.49 (2.40,2.60)	0.00024±0.00003	0.00024±0.00003
2.70 (2.60,2.80)	0.00015±0.00002	0.00015±0.00002
2.90 (2.80,3.00)	0.000096±0.000010	0.000096±0.000010
3.16 (3.00,3.35)	0.000054±0.000004	0.000054±0.000004
3.55 (3.35,3.80)	0.000022±0.000002	0.000022±0.000002
4.06 (3.80,4.40)	0.0000078±0.0000006	0.0000078±0.0000006
4.70 (4.40,5.10)	0.0000024±0.0000002	0.0000024±0.0000002
5.48 (5.10,6.00)	0.00000072±0.00000007	0.00000072±0.00000007
6.42 (6.00,7.00)	0.00000019±0.00000002	0.00000019±0.00000002
7.43 (7.00,8.00)	0.000000077±0.000000012	0.000000077±0.000000012
8.43 (8.00,9.00)	0.000000024±0.000000006	0.000000024±0.000000006
9.44 (9.00,10.00)	0.000000012±0.000000004	0.000000012±0.000000004

Table G.1: p+p changed hadron yields.

d+Au	$\frac{1}{2\pi p_\perp} d^2N/dp_\perp d\eta\|_{\eta=0}(GeV/c)^{-2}$	
$p_\perp$(low,high) [GeV/c]	0-20% Central	Minimum Bias
1.05 (1.00,1.10)	0.32±0.03	0.16±0.01
1.15 (1.10,1.20)	0.23±0.02	0.11±0.01
1.25 (1.20,1.30)	0.16±0.01	0.081±0.004
1.35 (1.30,1.40)	0.12±0.01	0.058±0.003
1.45 (1.40,1.50)	0.085±0.007	0.042±0.002
1.55 (1.50,1.60)	0.062±0.004	0.030±0.001
1.65 (1.60,1.70)	0.046±0.003	0.022±0.001
1.75 (1.70,1.80)	0.034±0.002	0.016±0.001
1.85 (1.80,1.90)	0.025±0.001	0.012±0.001
1.95 (1.90,2.0)	0.019±0.001	0.0091±0.0004
2.05 (2.00,1.10)	0.014±0.001	0.0068±0.0003
2.15 (2.10,2.20)	0.010±0.000	0.0050±0.0003
2.25 (2.20,2.30)	0.0078±0.0004	0.0038±0.0002
2.35 (2.30,2.40)	0.0059±0.0003	0.0028±0.0002
2.49 (2.40,2.60)	0.0039±0.0003	0.0019±0.0001
2.70 (2.60,2.80)	0.0024±0.0002	0.0011±0.0001
2.90 (2.80,3.00)	0.0015±0.0001	0.00072±0.00005
3.16 (3.00,3.35)	0.00085±0.00004	0.00041±0.00002
3.56 (3.35,3.80)	0.00036±0.00002	0.00017±0.00001
4.07 (3.80,4.40)	0.00013±0.00001	0.000062±0.000004
4.71 (4.40,5.10)	0.000038±0.000004	0.000019±0.000002
5.50 (5.10,6.00)	0.000010±0.000001	0.0000052±0.0000006
6.44 (6.00,7.00)	0.0000023±0.0000003	0.0000013±0.0000002
7.45 (7.00,8.00)	0.00000074±0.00000012	0.00000040±0.00000006
8.45 (8.00,9.00)	0.00000020±0.00000004	0.00000012±0.00000002
9.46 (9.00,10.00)	0.000000074±0.000000021	0.000000050±0.000000009

Table G.2: d+Au changed hadron yields.

Appendix H

Glossary

ADC *Analog to Digital Converter*

Converts an continuous voltage into a discrete electrical signal

AGS *Alternating Gradient Synchrotron*

A pre-accelerator for RHIC

Au+Au *Gold on Gold*

Gold on Gold Collisions

BBC *Beam-Beam Counters*

Annular scintillator at high pseudorapidity used to trigger p+p collisions

BNL *Brookhaven National Laboratory*

A science laboratory located in Long Island, NY that houses the RHIC experiments

CTB *Central Trigger Barrel*

A collection of scintillating slats that surround the TPC

DAQ *Data AQuistion*

The system that collects and stores information from the detectors

DCA *Distance of Closest Approach*

The smallest distance separating two geometrical objects

FEE *Front End Electronics*

Electronics that are mounted on detector elements

FTPC *Forward Time Projection Chamber*

A drift chamber,similar to the TPC, that tracks charged particles at forward angles

GEANT *GEometry ANd Tracking*

A computing library to model detector geometries and energy loss in detector materials

HERWIG *Hadron Emission Reactions With Interfering Gluons*

An event generator for Hadron Emission Reactions With Interfering Gluons (including supersymmetric processes)

HIJING *Heavy Ion Jet INteraction Generator*

A model to simulate nucleus nucleus collisions

LHC *Large Hadron Collider*

The future highest energy accelerator being constructed at CERN

MWPC *Multi-Wire Proportional Chamber*

A series of wire grids that amplifies and determines the 2 dimensional location of an drift electron

NSD *Non-Singly Diffractive*

A p+p or p+$\bar{\text{p}}$ event where both nucleons fragment

RDO *Read Data Out*

The interface between detector systems and data acquisition

RHIC *Relativistic Heavy Ions Collider*

A 3.8 km accelerator located at BNL capable of colliding most nucleons from protons to gold.

STAR *Solenoidal Tracker At RHIC*

One of the four main experiments at RHIC

SVT *Silicon Vertex Tracker*

A solid-state drift detector located close to the beamline

TPC *Time Projection Chamber*

A large cylindrical drift chamber which provides charged particle tracking

ZDC *Zero Degree Calorimeter*

A detector located along the beamline (zero degrees in θ) that measures neutrons

d+Au *Deuteron on Gold*

Deuteron on Proton Collisions

eV *Electron Volt*

The amount of energy an electron acquires when accelerated through a 1 Volt potential

$\mathbf{p}_\perp$ *Transverse Momentum*

The component of momentum perpendicular to the beamline

$\mathbf{p+\bar{p}}$ *Proton on Anti-Proton*

Proton on Anti-Proton Collisions

p+p *Proton on Proton*

Proton on Proton Collisions

PMT *Photo Multiplier Tubes*

A detector that amplifies a photon into a electrical pulse

ppLMV *Proton+Proton Low Multiplicity Vertex*

The standard vertex finder used for low multiplicity p+p events in STAR

Bibliography

[1] LBL Nuclear Sciece Division and CPEP. The Nuclear Wall Chart. http://www.lbl.gov/abc/wallchart/index.html.

[2] E. D. Bloom et al. High-energy inelastic e p scattering at 6-degrees and 10-degrees. *Phys. Rev. Lett.*, 23:930–934, 1969.

[3] Frithjof Karsch. Lattice Results on QCD Thermodynamics. *Nucl. Phys.*, A698:199–208, 2002. hep-ph/0103314.

[4] Siegfried Bethke. Alpha(s) 2002. *Nucl. Phys. Proc. Suppl.*, 121:74–81, 2003. hep-ex/0211012.

[5] Siegfried Bethke. Determination of the QCD coupling α_s. *J. Phys.*, G26:R27, 2000. hep-ex/0004021.

[6] J. Pumplin et al. New generation of parton distributions with uncertainties from global qcd analysis. *JHEP*, 07:012, 2002. hep-ph/0201195.

[7] S. Kretzer. Fragmentation functions from flavour-inclusive and flavour- tagged e+ e- annihilations. *Phys. Rev.*, D62:054001, 2000. hep-ph/0003177.

[8] G. J. Alner et al. Anti-Proton - Proton Cross-Sections at 200 GeV and 900 GeV Center-of-Mass Energy. *Z. Phys.*, C32:153, 1986.

[9] H. Hahn et al. The RHIC Design Overview. *Nucl. Instrum. Meth.*, A499:245–263, 2003.

[10] Tandem Van de Graff Group. Tandem Van de Graff. http://www.bnl.gov/bnlweb/facilities/TVdG.html.

[11] NEC. Peletron Charging System. http://www.pelletron.com/charging.htm.

[12] Distributed by Peabody Scientific, Peabody, MA, 01960, USA.

[13] Alternating Gradient Synchrotron. URL: http://www.bnl.gov/bnlweb/facilities/AGS.html, 2003.

[14] C.J. Gardner. *Internal RHIC Note*, 2003.

[15] RHIC Project. RHIC Design Manual. *Technical Design Report, Brookhaven National Laboratory*, URL: http://www.agsrhichome.bnl.gov/NT-share/rhicdm/, 1994.

[16] L. Ahrens et al. The RHIC Injector Accelerator Configurations, and Performance for the RHIC 2003 Au-d Physics Run. Presented at IEEE Particle Accelerator Conference (PAC2003).

[17] W. Fischer et al. Intra-beam Scattering Measurements in RHIC. Presented at European Particle Accelerator Conference, Paris, 2002.

[18] Clemens Adler et al. The RHIC Zero Degree Calorimeters. *Nucl. Instrum. Meth.*, A470:488–499, 2001. nucl-ex/0008005.

[19] Manuel Calderon de la Barca Sanchez. *Charged Hadron Spectra in Au + Au Collisions at* $\sqrt{s_{\mathrm{NN}}} = 130$ *GeV*. PhD thesis, Yale University, 2001. nucl-ex/0111004.

[20] M. Anderson. The STAR Time Projection Chamber: A Unique Tool for Studying High Multiplicity Events and rhic. *Nucl. Instrum. Meth.*, A499:659, 2003.

[21] M. Anderson et al. A Readout System for the STAR Time Projection Chamber. *Nucl. Instrum. Meth.*, A499:679, 2003.

[22] STAR Conceptual Design Report. *Technical Report No. Pub-5347,LBL (unpublished).*

[23] K. Hagiwara et al. Review of Particle Physics. *Phys. Rev.*, D66:010001, 2002.

[24] F. Bergsma et al. The STAR Detector Magnet System. *Nucl. Instrum. Meth.*, A499:633, 2003.

[25] Matthew Horsley. *A measurement of the Charged Particle Ratios* $\frac{\pi^-}{\pi^+}$*,* $\frac{K^-}{K^+}$ *and* $\frac{\bar{P}}{P}$ *at High Transverse Momentum in an Ultra-Relativistic Heavy Ion Collision.* PhD thesis, Yale University, 2002.

[26] K.H. Ackermann et al. The Forward Time Projection Chamber (FTPC) in STAR. *Nucl. Instrum. Meth.*, A499:679, 2003.

[27] R. Bellwied et al. The STAR Silicon Vertex Tracker: A Large Area Silicon Drift Detector. *Nucl. Instrum. Meth.*, A499:640, 2003.

[28] Bum Choi. *High* $p_\perp$ *Inclusive Charged Hadron Distributions in Au+Au Collisions at* $\sqrt{s_{\rm NN}} = 130$ *GeV at RHIC.* PhD thesis, University Of Texas, 2003.

[29] Jan Balewski. *Private Comunications*, 2003.

[30] D. Cebra and S. Margetis. Main Vertex Reconstruction in STAR. *STAR note SN089,(unpublished).*

[31] Xin-Nian Wang and Miklos Gyulassy. A Systematic Study of Particle Production in p + p (anti-p) Collisions via the HIJING Model. *Phys. Rev.*, D45:844–856, 1992.

[32] CERN Program Library Office. GEANT: Detector Description and Simulation Tool. 1993. Cern Program Library Long Writeup W5013.

[33] J. Adams and L. Gaudichet. *Private Comunications*, 2003.

[34] M. Heinz. *Private Comunications*, 2003.

[35] K.O. Schweda. *Private Comunications*, 2003.

[36] Yu Chen. *High Transverse Momentum Charged Hadron Production in Au+Au Collisions at the Relativistic Heavy Ion Collider.* PhD thesis, University Of California, Los Angeles, 2003.

[37] C. Albajar et al. A Study of the General Characteristics of Proton - Anti-Proton Collisions at $\sqrt{s} = 0.2$ TeV to 0.9 TeV. *Nucl. Phys.*, B335:261, 1990.

[38] A. Drees et al. Results From Vernier Scans at RHIC Durring the PP Run 2001-2002. Presented at IEEE Particle Accelerator Conference (PAC2003), 12-16 May 2003.

[39] Thomas Roser. RHIC Run 3 (FY2003) Running Projections. URL: http://www.rhichome.bnl.gov/AP/RHIC2003/, 2002.

[40] Torbjorn Sjostrand, Leif Lonnblad, and Stephen Mrenna. Pythia 6.2: Physics and manual. 2001. hep-ph/0108264.

[41] G. Corcella et al. Herwig 6.5 release note. 2002. hep-ph/0210213.

[42] Mikhail Kopytine and Joanna Kiryluk. *Private Comunications*, 2003.

[43] N. Amos et al. Measurement of Small Angle Anti-Proton - Proton and Proton Proton Elastic Scattering at the CERN Intersecting Storage Rings. *Nucl. Phys.*, B262:689, 1985.

[44] M. Bozzo et al. Measurement of the Proton - Anti-Proton Total and Elastic Cross-Sections at the CERN SPS Collider. *Phys. Lett.*, B147:392, 1984.

[45] R. E. Ansorge et al. Charged Particle Multiplicity Distributions at 200 GeV and 900 Gev center-of-mass Energy. *Z. Phys.*, C43:357, 1989.

[46] A. Breakstone et al. Multiplicity dependence of the average transverse momentum and of the particle source size in p p interactions at $\sqrt{s_{_{\rm NN}}} =$ 62-GeV, 44-GeV and 31-GeV. *Z. Phys.*, C33:333, 1987.

[47] J. Adams et al. Transverse Momentum and Collision Energy Dependence of High-$p_\perp$ Hadron Suppression in Au + Au Collisions at Ultrarelativistic Energies. *Phys. Rev. Lett.*, 91:172302, 2003. nucl-ex/0305015.

[48] C. Adler et al. Centrality Dependence of High $p_\perp$ Hadron Suppression in Au + Au Collisions at $\sqrt{s_{\mathrm{NN}}} = 130$ GeV. *Phys. Rev. Lett.*, 89:202301, 2002. nucl-ex/0206011.

[49] Dmitri Kharzeev, Eugene Levin, and Larry McLerran. Parton saturation and N_{part} scaling of semi-hard processes in QCD. *Phys. Lett.*, B561:93–101, 2003. hep-ph/0210332.

[50] Dmitri Kharzeev and Eugene Levin. Manifestations of high density QCD in the first RHIC data. *Phys. Lett.*, B523:79–87, 2001. nucl-th/0108006.

[51] Larry D. McLerran. The Color Glass Condensate and Small x Physics: 4 Lectures. *Lect. Notes Phys.*, 583:291–334, 2002. hep-ph/0104285.

[52] Edmond Iancu, Kazunori Itakura, and Larry McLerran. Geometric scaling above the saturation scale. *Nucl. Phys.*, A708:327–352, 2002. hep-ph/0203137.

[53] K. J. Eskola, V. J. Kolhinen, and C. A. Salgado. The scale dependent nuclear effects in parton distributions for practical applications. *Eur. Phys. J.*, C9:61–68, 1999.

[54] J. J. Aubert et al. Measurements of the nucleon structure functions $F_2(n)$ in deep inelastic muon scattering from deuterium and comparison with those from hydrogen and iron. *Nucl. Phys.*, B293:740, 1987.

[55] Michele Arneodo. Nuclear effects in structure functions. *Phys. Rept.*, 240:301–393, 1994.

[56] J. W. Cronin et al. Production of hadrons with large transverse momentum at 200-GeV, 300-GeV, and 400-gev. *Phys. Rev.*, D11:3105, 1975.

[57] M. M. Aggarwal et al. Transverse mass distributions of neutral pions from Pb-208 induced reactions at 158-A-GeV. *Eur. Phys. J.*, C23:225–236, 2002. nucl-ex/0108006.

[58] Yuri L. Dokshitzer, Valery A. Khoze, Alfred H. Mueller, and S. I. Troian. Basics of perturbative QCD. Gif-sur-Yvette, France: Ed. Frontieres (1991) 274 p.

[59] K. Gallmeister, C. Greiner, and Z. Xu. Quenching of high $p_\perp$ hadron spectra by hadronic interactions in heavy ion collisions at RHIC. *Phys. Rev.*, C67:044905, 2003. hep-ph/0212295.

[60] Xin-Nian Wang. Why the observed jet quenching at RHIC is due to parton energy loss. *Phys. Lett.*, B579:299–308, 2004. nucl-th/0307036.

[61] W. Cassing, K. Gallmeister, and C. Greiner. Suppression of high transverse momentum hadrons at rhic by (pre-) hadronic final state interactions. 2003. hep-ph/0311358.

[62] Miklos Gyulassy, Ivan Vitev, Xin-Nian Wang, and Ben-Wei Zhang. Jet quenching and radiative energy loss in dense nuclear matter. 2003. nucl-th/0302077.

[63] Enke Wang and Xin-Nian Wang. Parton energy loss with detailed balance. *Phys. Rev. Lett.*, 87:142301, 2001. nucl-th/0106043.

[64] Xin-Nian Wang. High $p_\perp$ hadron spectra, azimuthal anisotropy and back-to-back correlations in high-energy heavy-ion collisions. 2003. nucl-th/0305010.

[65] Enke Wang and Xin-Nian Wang. Jet tomography of dense and nuclear matter. *Phys. Rev. Lett.*, 89:162301, 2002. hep-ph/0202105.

[66] Dmitri Kharzeev, Yuri V. Kovchegov, and Kirill Tuchin. Cronin effect and high-$p_\perp$ suppression in p-A collisions. *Phys. Rev.*, D68:094013, 2003. hep-ph/0307037.

[67] I. Arsene et al. On the evolution of the nuclear modification factors with rapidity and centrality in d+Au collisions at $\sqrt{s_{NN}} = 200$ gev. 2004. nucl-ex/0403005.

[68] Xin-Nian Wang. Rapidity asymmetry in high-energy d+A collisions. *Phys. Lett.*, B565:116–122, 2003. nucl-th/0303004.

[69] J. Ashman et al. Measurement of the ratios of deep inelastic muon - nucleus cross-sections on various nuclei compared to deuterium. *Phys. Lett.*, B202:603, 1988.

[70] Michael Miller. *Measurement of Jets and Jet Quenching at RHIC.* PhD thesis, Yale University, 2003.

[71] J. Adams et al. Evidence from d + Au Measurements for Final-State Suppression of High-$p_\perp$ Hadrons in Au + Au Collisions at RHIC. *Phys. Rev. Lett.*, 91:072304, 2003. nucl-ex/0306024.

[72] C. Adler et al. Disappearance of back-to-back high $p_\perp$ hadron correlations in central Au + Au collisions at $\sqrt{s_{NN}} = 200$ GeV. *Phys. Rev. Lett.*, 90:082302, 2003. nucl-ex/0210033.

[73] W. Cassing, K. Gallmeister, and C. Greiner. Quenching of high p(t) hadrons by (pre-)hadronic fsi at rhic. 2004. hep-ph/0403208.

[74] Thomas S. Ullrich. Experimental summary on global observables, hadron spectra and ratios. *Nucl. Phys.*, A715:399–411, 2003. nucl-ex/0211004.

[75] T. Matsui and H. Satz. J/ψ suppression by Quark-Gluon Plasma formation. *Phys. Lett.*, B178:416, 1986.

[76] A. D. Frawley. J/$\psi \to ee$ and J/$\psi \to \mu\mu$ measurements in AuAu and pp collisions at $\sqrt{s_{NN}} = 200$ GeV. *Nucl. Phys.*, A715:687–690, 2003. nucl-ex/0210013.

[77] Jeffery Mitchell and Iwona M. Sakrejda. Tracking for the STAR TPC Documentation and User's Guide. *STAR note SN0190*, 1995.

[78] R. Bossingham et al. STAR Offline Simulations and Analysis Software Design. *STAR note 0281*, 1997.

[79] Claude Pruneau. ITTF (Integrated Tracking Task Force) Users Guide. http://www.star.bnl.gov/STAR/ittf/ITTF.pdf.

[80] Brian Lasiuk and Thomas Ullrich. *Star C++ Class Library: User Guide and Reference Manual*, 1999.

[81] F. James and M. Roos. 'MINUIT' A System For Function Minimization and Analysis of the Parameter Errors and Correlations. *Comput. Phys. Commun.*, 10:343–367, 1975.

[82] G. D. Lafferty and T. R. Wyatt. Where to stick your data points: The treatment of measurements within wide bins. *Nucl. Instrum. Meth.*, A355:541–547, 1995.

[83] R.J. Glauber. *Lectures on theoretical physics*, volume 1. Inter-Science, 1959.

[84] R.D. Woods and D.S. Saxon. Diffuse surface optical model for nucleon-nuclei scattering. *Phys. Rev*, 95:577, 1954.

[85] Dmitri Kharzeev, Eugene Levin, and Marzia Nardi. QCD Saturation and Deuteron Nucleus Collisions. 2002. hep-ph/0212316.

[86] Hulthén and Sagawara. *Handbuch der Physik*. Springer-Verlag, Berlin, 1957.

Index